Kent Academic Repository

Full text document (pdf)

Citation for published version

Nicholas, Jack (2016) Photometry of the UWISH2 extended H2 source catalogue. Master of Science by Research (MScRes) thesis, University of Kent.

DOI

Link to record in KAR

https://kar.kent.ac.uk/54879/

Document Version

UNSPECIFIED

Photometry of the UWISH2 extended H$_2$ source catalogue

– Jack Nicholas –

Centre for Astrophysics and Planetary Science

School of Physical Sciences

University of Kent

University of Kent

Thesis submitted to the University of Kent in partial fulfilment of the requirements for the degree of Master of Science.

2016

Declaration

This thesis has not been submitted as an exercise for a degree at any other university.

Except where stated, the work described therein was carried out by me alone.

I give permission for the Library to lend or copy this thesis upon request.

SIGNED:

Acknowledgements

I firstly would like to thank my supervisor Dr. Dirk Froebrich for allowing me to participate in his project. His guidance and expertise have been greatly appreciated and I am thankful for every comment and remark he has made to further my education.

I would like to thank Dr. Mark Price for setting me up with a work station and solving the occasional technical issue. This thanks would have to be shared with PhD student Tim Kinnear, who has also assisted me overcome the occasional Python hurdle.

The data in this thesis is obtained from images taken by the United Kingdom Infrared Telescope which is operated by the the Joint Astronomy Centre on behalf of the Science and Technology Facilities Council of the U.K. I therefore wish to acknowledge and thank them.

The first of several group mentions goes to the University of Kent Men's Rugby club that I have been a member of for four years. I am thankful for all the experiences I have had, including the opportunity to have served as a team captain this year. Secondly, I wish to thank my work colleagues at the Venue nightclub where I have spent two years serving Canterbury's finest young minds with you and witnessing various hilarious acts. Finally, I thank fellow committee members of the University of Kent Physics Society for your support, in alphabetical order: Neil Beszant, John Bottomley, Jenn Bradshaw, Sophie Debenham, Jacob Harman, Kirsty Lukas, Evie Polden and Vishal Patel. ΦΣΚ.

Individual thanks first goes to Samuel Davis and Helen Lafferty. I have enjoyed the countless hours working with you in the postgraduate room that I was technically not allowed in. Twenty-four, Helen. To Sally Cutter, I must thank you for the amazing support you have given me during the write-up period.

I would like to acknowledge both Tam Alam-Ballard, who introduced me to astrophysics, and David Ditzel, who encouraged me to pursue both my BSc and this MSc. Five years on and I wish to thank them for setting me on this path.

My final acknowledgement goes to my mum. Your love and support has been resolute and I thank you so much for all you have done so I can be sitting here now, writing these two sentences.

Publications

Presented here is a list of publications, completed or currently ongoing, from the result of work presented in this thesis:

D. Froebrich, S. V. Makin, C. J. Davis, T. M. Gledhill, Y. Kim, B.-C. Koo, J. Rowles, J. Eislöffel, J. Nicholas, J. J. Lee, J. Williamson, and A. S. M. Buckner. The UWISH2 extended H2 source catalogue.*Monthly Notices of the RAS*, 454:2568-2605, December 2015. doi: 10.1093/mnras/stv1729

D. Froebrich, S. V. Makin. in prep.

S. V. Makin, D. Froebrich. in prep.

T. M. Gledhill et al. in prep.

Abstract

The UKIRT Widefield Infrared Survey for H_2 (UWISH2) is a large, unbiased survey of extended H_2 emission sources, using the 1–$0\,S(1)$ emission line at $2.122\,\mu m$. It covers 209 square degrees of the Galactic Plane (GP) between $l \approx 357°$ to $l \approx 66°$ and $b \approx \pm 1.5°$. UWISH2 further covers high column density regions in Cygnus and Auriga, covering approximately 42 and 35.5 square degrees respectively and leading to a total survey coverage of ≈ 286.5 square degrees. As part of the UWISH2 team, I have performed the photometry for 33200 individual H_2 features, which have been found to compose ~ 700 H_2 jets and outflows, 284 planetary nebulae (PNe), 30 supernova remnants (SNRs) and ~ 1300 photo-dissociation regions (PDRs). About 60% of PNe are newly discovered candidates. Using H_2 emission as a tracer for star formation, I find that the majority of H_2 flux is located in the lower Galactic longitudes for jet and PDR features, indicating increased star formation activity. I have also observed partial concentrations of high H_2 flux at higher Galactic longitudes in the GP from jet features but not PDR features, indicating a lack of high-mass star formation at this region. I offer two methods of photometry: the 'total flux' photometry and the 'median surface brightness times area' photometry. Upon comparing the ratios of the fluxes from both photometries for each feature, I find good agreement (full catalogue: $\sim 97\%$ in a 100% deviation and $\sim 82\%$ in a 20% deviation) for all feature classes except jets, and recommend the median surface brightness times area photometry for all feature types except jets, which should use total flux photometry. Finally, I have calculated the signal-to-noise ratios for individual features, finding the median value for the entire survey to be approximately 15 when using the feature area.

Contents

List of Figures

List of Tables

Chapter 1

Introduction

In this chapter I will present an overview of molecular clouds (MC) and star formation, including some of their physical characteristics, and discuss methods of their support and collapse into clumps and prestellar cores. This will expand into the differences between low and high ($> 8\,\mathrm{M_\odot}$) mass star formation. I will then briefly talk about some properties of the prominent extended molecular hydrogen (H_2) emission sources encountered in the UWISH2 survey, including jets and outflows from young stellar objects (YSOs), planetary nebulae (PNe), supernovae remnants (SNRs) and photo-dissociation regions/ionised hydrogen regions (PDRs/H$_{\text{II}}$ regions). I will then introduce the UWISH2 image survey and discuss its uniqueness. I will then explain how the survey data was gathered and processed.

1.1   The H$_2$ Molecule

This thesis analyses molecular hydrogen emission. Because molecular hydrogen is symmetrical, it does not possess a permanent dipole moment. This means that dipole transitions between rotational, J, and vibrational, ν, (ro-vib) levels are very rare and would require large timescales to occur. Electric quadrupole transitions happen at a far quicker rate and hence are much more likely to occur. The excitation energies for molecular hydrogen are high. The lowest emission energy is from the 0–0 S(0) transition, with a wavelength of $28.22\,\mu m$ which translates to a

minimum excitation temperature of roughly $500\,\mathrm{K}$. The typical temperatures of a MC vary from $10-30\,\mathrm{K}$ so the cold gases would not have enough energy to excite these lines meaning molecular hydrogen would be unobservable. In order to observe ro-vib lines we require the gases to become excited. Methods that can excite the molecule into emission include thermal excitation (from shocks) and fluorescence (from photons). An example of thermal excitation includes bowhead shocks produced from bipolar jets emanating from YSOs, which heat up the surrounding protostellar material to thousands of Kelvin and allows the first couple of vibrational levels to be populated. The $2.122\,\mu m$, $1\text{--}0\,\mathrm{S}(1)$ transition traces regions of shock-excited H_2 at temperatures of the order of $10^3\,\mathrm{K}$ and so becomes observable in the hot star forming environment. If gas temperatures continued to grow, the molecular hydrogen would dissociate. A detailed discussion of shock-excited molecular hydrogen (in jets) is given by Wolfire and Konigl (1991). Figure 1.1 shows a diagram representing the lower ro-vib levels of a molecule, including the $1\text{--}0\,\mathrm{S}(1)$ transition with $\Delta J = 3 \rightarrow 1$ and $\Delta \nu = 1 \rightarrow 0$. The corresponding temperature of H_2 at the $J = 3$ and $\nu = 1$ energy level is approximately $6000\,K$, but we still see strong emission from gas at $1000\,K$. This is because a fraction of molecules possess the required energy to be excited, even with a lower temperature, as illustrated by a Maxwell-Boltzmann distribution. Figure 1.2 shows the potential energy curves versus internuclear distance of the ground state and first excited state of molecular hydrogen. We can see that when in the ground state, a vibrational level of 14 dissociates the molecule.

1.2 Molecular Clouds

Molecular clouds (MCs) are large and relatively dense regions in space which are comprised of material known as the interstellar medium (ISM), a collection of dust grains and gases in various forms including an abundance of H_2. They appear to us as dark clouds amongst the bright background of the Milky Way as the dust grains absorb the distant starlight behind them.
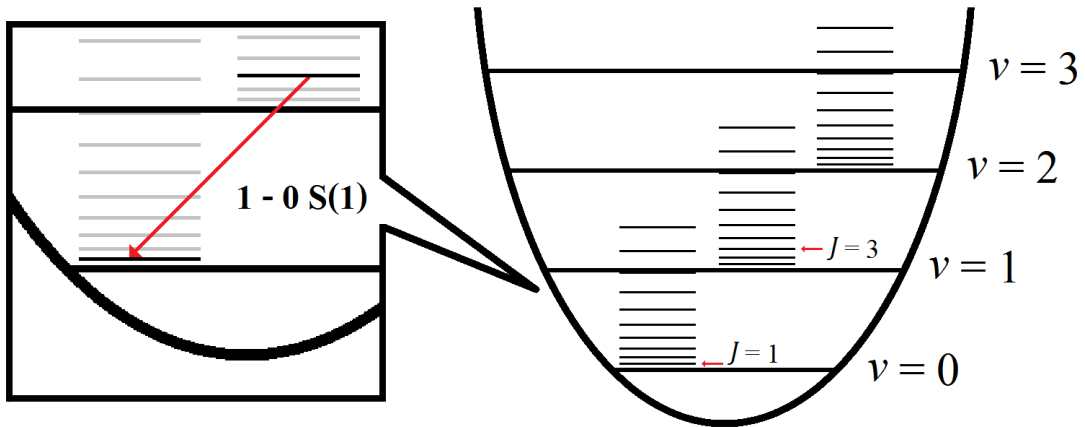
Figure 1.1: Diagram showing the rotational and vibrational levels of a molecule (right) and highlights the 1–0 S(1) transition (left).
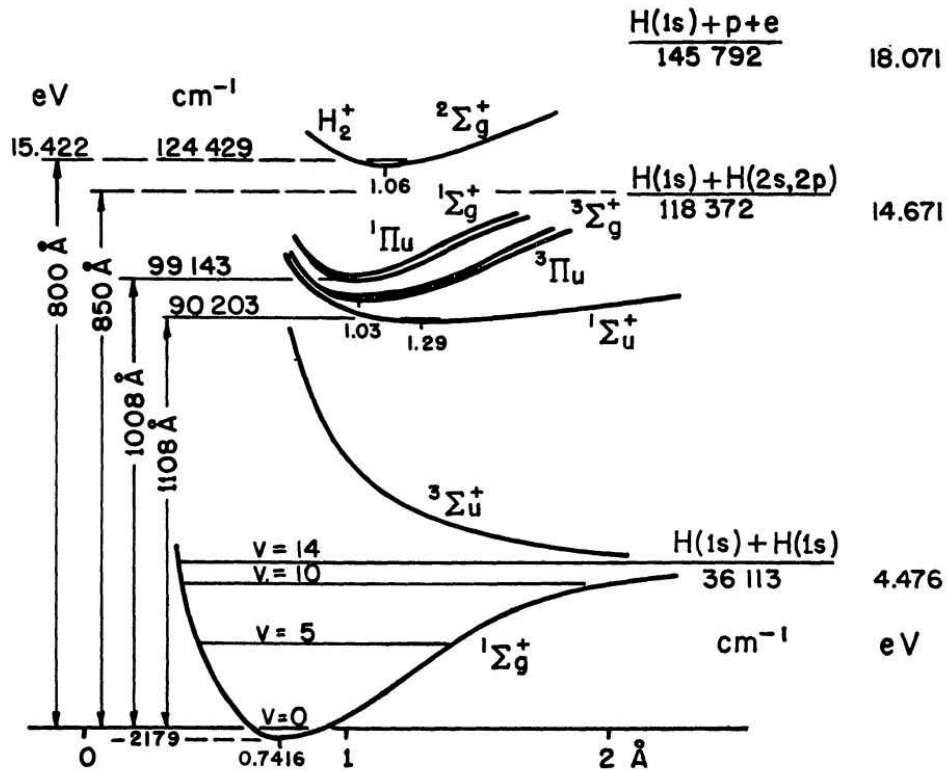
Figure 1.2: The various energy levels of molecular hydrogen shown in a diagram taken from Field et al. (1966). Excitation, dissociation and ionisation energies are shown relative to the $\nu = 0$ ground state level.

Surrounding the MC is an envelope of atomic hydrogen (Hɪ). Interstellar turbulence creates shocks causing density fluctuations in the cloud. In regions of high density, molecular hydrogen readily forms on the surface of dust grains from two Hɪ. For this process, an atom of neutral hydrogen binds weakly to a dust grain via van der Waals bonding before moving to a lattice defect on the grain. A second hydrogen atom will then move around the surface of the dust grain, until it encounters the first. The two atoms bond together to form H_2. The newly formed molecule releases a binding energy of $4.5\,\mathrm{eV}$ upon formation which is used to release itself from the dust grain and also contributes to the internal and kinetic energies of the molecule. This process occurs as such:

$$H + H + \text{dust grain} \rightarrow H_2 + \text{dust grain} \tag{1.1}$$
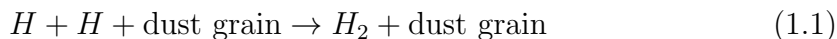
The density of a MC is far less dense than gases present in Earth's atmosphere, for example, which means that collisions between Hɪ and dust grains could take days. The rate of molecular hydrogen formation increases with material density (Hollenbach et al., 1971).

Properties of Molecular Clouds

Molecular clouds exhibit complex and often filamentary structures. They need to have a high opacity in order to shield molecules from incident UV radiation, which can dissociate them. The column density, σ, required to shield molecules from the UV radiation where extinction, A_V, is equal to 1 can be calculated using:

4

$$N(H) = 6.83 \times 10^{21} cm^{-2} \cdot \frac{A_V}{R_V}$$

$$N(H) = 6.83 \times 10^{21} cm^{-2} \cdot \frac{1}{3}$$

$$N(H) = 2.2767 \times 10^{21} cm^{-2}$$

$$\sigma = N(H) \times m_H$$

$$m_H = 1.6733 \times 10^{-24} g$$

$$\sigma = 3.81 \times 10^{-3} g\, cm^{-2}$$

$$(1.2)$$

where R_V describes the dust properties and is typically ~ 3 (Mathis, 1990). There-fore, MCs require column densities of about $4 \times 10^{-3} \, \mathrm{g\, cm^{-2}}$ to exist, but typical column densities are of the magnitude $3 \times 10^{-2} \, \mathrm{g\, cm^{-2}}$. Typical sizes of MCs range from $2 - 20$ pc but there are recorded sizes of up to a couple 10^2 pc and MCs can contain between 10^2–10^6 $\mathrm{M_\odot}$. These values and other appropriate numbers can be found in Table 1.1. There are different classifications of MCs relating to their size and masses. The largest are referred to as giant molecular clouds (GMCs) and describe clouds that contain roughly 10^4–10^6 $\mathrm{M_\odot}$ but this is speculative and open to an individuals interpretation of 'giant'. Star formation processes in GMCs drive the cloud material to become fragmented. These fragments possess higher densities and are known as clumps, and will eventually collapse to form prestellar cores and eventually protostars. Their physical characteristics are displayed alongside those of the cloud in Table 1.1.

Table 1.1: Table containing some physical properties (ranges) of molecular clouds and cores adapted from Klessen (2011). For each stage, left-right chronologically ordered, large decreases in size and mass coincide with large increases in mean density as core is formed.

Property	Molecular cloud	Clumps	Protostellar core
Size (pc)	2–20	0.1–2	$\lesssim 0.1$
Mass ($M_\odot$)	10^2–10^6	10–10^3	0.1–10
Temperature (K)	10–30	10–20	7–12
Column Density ($g\,cm^{-2}$)	0.03	0.03–1.0	0.3–3
Mean density ($H_2\,cm^{-3}$)	10^2–10^3	10^3–10^5	$> 10^5$

Turbulence and Magnetic Fields

Turbulence

Within GMCs, velocity dispersion, size and luminosity are related via the three Larson relations (Larson, 1981). One of these relations indicates a correlation between velocity dispersion, σ_v and region size. A relationship appeared showing that velocity dispersion was proportional to the 0.38 power of the cloud size. The relationship has changed since it was first described. Solomon et al. (1987) found that the velocity linewidth of GMCs was proportional to the 0.5 power of the cloud size. The full relationships, where R is cloud size in parsecs, can be approximately expressed as:

$$\sigma_v \approx 1.10\,R^{0.38} \text{ (Larson, 1981)}$$

$$\sigma_v \approx 0.72\,R^{0.5} \text{ (Solomon et al., 1987)}$$

One characteristic that is prominent in all MCs is that the observed velocity linewidth is much greater than one would expect from thermal motions of the 10–20 K temperatures. This has been attributed to the presence of a series of random internal motions known as supersonic turbulence. Pressure from turbulence is a factor in the prevention of rapid collapse of the cloud. Thus the turbulent energy must be of the same or higher magnitude than the gravitational energy in order

to achieve a virial balance between turbulent pressure and self-gravity. The ratio of turbulence to gravitational energy is found to be almost always greater than one with the exception of very dense regions (Rosolowsky et al., 2008). Without this support, the cloud would undergo a global collapse. Therefore, this support contributes to the observed low star formation efficiency (Klessen et al., 2000; Krumholz and McKee, 2005).

Magnetic Fields

Turbulence is not the only means of support against a global collapse of the cloud. Magnetic fields are reviewed as a support mechanism by Shu et al. (1987), where random internal motions are attributed to magneto-hydrodynamic (MHD) waves. It is accepted that the energy from a combination of turbulence and magnetic fields provides the large scale support against the clouds own gravity. Observations are done by Zeeman splitting (Crutcher, 1999) and show that typical magnetic field strengths for MCs range from a few to a few hundred μG. Depending on the size of the magnetic field strength, they can offer either permanent or temporary support to a cloud. A strongly magnetized 'subcritical' cloud will be perpetually prevented from collapse whereas a weakly magnetized 'supercritical' cloud will inevitably undergo collapse, albeit delayed. Prestellar cores are initially subcritical but as they accumulate mass they exceed a critical mass and turn supercritical (Crutcher et al., 2009).

Fragmentation into Clumps and Core Formation

Prestellar cores form out of fragmented clumpy regions of the MC. There are different possible scenarios that cause these clumpy regions to form. One scenario states that turbulent motions within the cloud can create large density fluctuations across the cloud. These cause the cloud to fragment into clumps of high density material required for small prestellar cores to form. Alternatively, small

density fluctuations may be exaggerated and amplified by self-gravity to create the clumps. It is also possible that a combination of both occurs. From Jeans (1902) and Larson (2003), the Jeans length, λ_J, describes a critical value of wavelength, where plane-wave perturbations go from being pressure-dominated below the critical value to gravitationally-dominated when exceeding the value. The Jeans length of an isothermal medium with uniform density can be expressed in terms of the density, ρ and the isothermal sound speed, $c = (kT/m)^{\frac{1}{2}}$. In this case, m is the average particle mass. When the Jeans length is exceeded, the cloud becomes unstable and self-gravity prevails. The Jeans length is:

$$\lambda_J = \frac{\pi^{\frac{1}{2}} c}{(G\rho)^{\frac{1}{2}}} \tag{1.3}$$

Assuming the spatial dimensions of the cloud are similar to one another, the corresponding Jeans mass, M_J, can be calculated from the Jeans length using $M_J = \rho\lambda^3$. This is the critical mass value for a volume of gas whereby exceeding it leads to gravitationally unstable density fluctuations (Low and Lynden-Bell, 1976). With the constant $\pi^{\frac{3}{2}}$ approximately equal to 5.57, the Jeans mass becomes:

$$M_J = \frac{5.57 c^3}{G^{\frac{3}{2}} \rho^{\frac{1}{2}}} \tag{1.4}$$

Calculations using different geometries and state of equilibrium have yielded results close to the Jeans mass showing that it gives a good approximation for the minimum mass required for fragmentation.

There is some ambiguity in the process that turns clumpy regions into prestellar cores as there is no decisive model on how the material collapses to form the core. One accepted model utilizes the idea of gravitational fragmentation, where self-gravity overcomes thermal pressure for a clump of unstable gas leading to a runaway collapse (Larson, 1985). Another model depicts a core quasistatically increasing in density via ambipolar diffusion, where matter condenses along the magnetic field lines of the initially less dense core (Shu et al., 1987). Simulations have shown that collapse rate accelerates as ambipolar diffusion decreases the magnetic flux,

Table 1.2: CMF is the core mass function. Table listing the some of the main properties of the four core formation models. Adapted from André et al. (2009).

Models	Gravitational fragmentation (i)	Turbulent fragmentation (ii)
Strong B-field (iii)	Short (few Myr) timescale, Mildly supersonic infall, Initial CMF very narrow	Very short ($<$ Myr) timescale, Highly supersonic infall, Initial CMF is broad
Weak B-field (iv)	Long ($\sim$10 Myr) timescale, Subsonic infall, Initial CMF very narrow	Short (few Myr) timescale, Subsonic relative infall and supersonic systematic speeds, Initial CMF is broad

before progressing as in a case with no magnetic fields. A new model has been described by André et al. (2009) which emphasizes the supersonic turbulence's role of large scale support and small scale generation of density fluctuations. From a conceptual point of view, core formation models are divided into four categories. The distinguishing characteristics of these categories are whether the initial core formation happens a result of i) linear (gravitational fragmentation) or ii) non-linear (turbulent fragmentation) perturbations, and whether magnetic fields are iii) dynamically dominant or iv) not. The differences are summarized in Table 1.2.

Angular Momentum and the Angular Momentum Problem

Due to the presence of turbulence, the cores forming in the MC are expected to be rotating so that the angular momentum is conserved. Angular momentum in the star forming core is orders of magnitude higher than the angular momentum of the core of the star it will become. Due to the fact that there is such a huge angular momentum deficit in the later stages of a stars lifetime, and the necessity for angular momentum to be conserved, this has been dubbed the 'angular momentum problem'. One possible solution to this shedding of excess angular momentum is that rotating clouds can often form binary or multiple systems whose orbital motions must be taken into account. Observations show that the majority of stars form

this way (Zinnecker and Mathieu, 2001) and that some single stars are products of an unstable triple system, whereby the lightest member is ejected (Reipurth, 2000). Angular momentum is also responsible for the formation of an accretion disk around the protostar. In order for mass to be able to accrete from this disk onto the protostar, it needs to lose excess angular momentum. This indicates that there must be a method of redistributing angular momentum. Two main methods disk material can lose angular momentum by include i) some viscous transport process in the accretion disk and ii) jets/outflows. With the viscous process, angular momentum is transported outward in the disk. This happens due to the collision of particles in the disk and the exchange of angular momentum. Particles that are left with less angular momentum after the collision can then move inwards towards the protostar whilst the particle with more angular momentum moves outwards, taking the excess angular momentum with it. A time-dependent model known as 'magnetic braking' can also reduce the angular momentum of the disk by a few orders of magnitude in less than $1\,\mathrm{Myr}$ (Mouschovias and Paleologou, 1979). Magnetic braking occurs when strong stellar winds strip ionised material from a protostar. This material is captured by the protostars magnetic field lines and co-rotates with the star as it move outwards, taking the excess angular momentum with it.

Accretion

There is a large range in mass between the smallest and largest of stars and it has been proposed that the random turbulent motions may be the origin for stellar mass distributions and can influence the stars final mass (Padoan et al., 2007). When the core forms, it will possess a very small fraction of the stars final mass. Several simulations for the formation of a $1\,\mathrm{M_\odot}$ star have been discussed by Appenzeller and Tscharnuter (1975) and Masunaga and Inutsuka (2000). Most of the mass must be acquired through accretion, which is the process of gaining mass gradually from the infalling material of the circumstellar envelope into the accretion disk and towards the star forming core. Initially the accretion shock is adiabatic due to optically thick material, but after the accretion of the first hydrostatic core, radiation begins

10

to escape. This adiabatic core experiences further gravitational collapse triggered by the dissociation of molecular hydrogen. A protostar is born when the second core is accreted as a result of this. Numerical simulations of a gravitationally unstable, spherically symmetric core of finite size shows accretion decreases with time (Vorobyov and Basu, 2005). The mass accretion rate onto the star has been observed to change in gravitationally unstable disks (Vorobyov, 2009). Vorobyov and Basu (2006) found that the accretion rate can spend prolonged amounts of time at low values, typically $\lesssim 10^{-7} \, \mathrm{M_\odot} yr^{-1}$ and occasionally experience short and intense episodic accretion bursts when the rate can typically be $\gtrsim 10^{-4} \, \mathrm{M_\odot} yr^{-1}$. This is caused by the accretion of gravitationally fragmented disk material driven onto the protostar. Most of the star's mass is accreted during these bursts.

The protostar stops expanding at a radius of approximately $4 \, \mathrm{R_\odot}$ ($\sim 2 \times 10^{-2} \, \mathrm{AU}$) (Masunaga and Inutsuka, 2000). At about $0.2 \, \mathrm{M_\odot}$, the protostar can start burning deuterium. It continues to accrete mass and will eventually become a main sequence (M-S) star. Intermediate stages a star will go through include becoming a T-Tauri star, which is a young variable, and possibly an FU Orionis star, which is a young, extreme variable.

1.3 High Mass Star Formation

To explore the differences of high and low mass star formation, there must first be a critical mass that separates a star being low mass or high mass. To define this, we compare the accretion timescale to the contraction timescale of the protostar (also known as the Kelvin-Helmholtz timescale or KH from now on). These timescales can be written as:

$$t_{accr} \;\;=\;\; \frac{M_*}{\dot{M}_{accr}} \tag{1.5}$$

$$t_{KH} \;\;=\;\; \frac{GM_*^2}{R_*L_*} \tag{1.6}$$

where M_*, R_*, L_* denote the mass, radius and luminosity of the protostar respectively and $\dot{M}_{accr}$ denotes the mass accretion rate of the envelope, thought to be independent of M_*.

For low mass stars, the KH timescale is greater than the accretion timescale, meaning that contraction will occur after the supply of material is exhausted. The low mass star contracts slowly along the birthline to the zero-age main sequence (ZAMS) when it starts burning hydrogen. However, if there is enough material in the envelope, accretion will continue until the protostar mass reaches roughly $8\,M_\odot$, at which point these two timescales become equal (Palla and Stahler, 1993). Beyond this critical point, the accretion timescale overtakes the contraction timescale so that a rapid collapse of the star occurs. Hydrogen burning begins and the star becomes a ZAMS star whilst still immersed in material. At this stage, low mass star formation theories predict that further collapse is halted and that the surrounding environment is disrupted due to radiation pressure (Cesaroni, 2005). This would paradoxically imply that there are no stars greater than $8\,M_*$ in existence, and therefore requires the adaptation of low mass star formation theories.

One high mass star formation theory involves the collision or coalescence of intermediate mass protostars within a cluster. The formation of high mass stars as a result of collision is a subject that has been analysed heavily by Bonnell et al. (1998). The theory of coalescence has also been analysed by Maeder and Behrend (2002). Another model proposed in the monolithic collapse model (Zinnecker and Yorke, 2007), which is a scaled-up version of the low mass star formation by disc accretion model. In this scenario, a massive outflow forms very early after accretion has started, which serves as a mechanism to transport the high-energy radiative flux away from the core. One other model was proposed by Beech and Mitalas (1994) which states that high mass stars form through accretion with a non-fixed $\dot{M}_{accr}$. The accretion rate would be required to grow with time or stellar mass in order for the star to reach its final size before exhausting its hydrogen. This is because the main sequence lifetime of high mass stars is short, with lifetime

decreasing with increasing mass via:

$$t_{MS} \sim 7 \times 10^9 yrs \cdot \left(\frac{M_*}{M_\odot}\right) \cdot \left(\frac{L_\odot}{L_*}\right) \tag{1.7}$$

1.4 Jets and Outflows

There is a phenomenon observed in the early stages of protostellar evolution where newly formed stars drive mass back into the environments that they were born in via jets or molecular outflows. The outflows are energetic and possess some degree of collimation. They are often used as tracers to identify active star forming regions, especially in cases when the YSO source is obscured by disk material. I will discuss three main physical models that offer an explanation on the driving mechanism of jets, but no model is completely correct. They all rely on magneto-hydrodynamics (MHD) and stellar winds but differ in interaction zones and the point of the outflow origin. They are the:

- **Stellar surface wind**

    This is where an isotropic wind from the stellar surface sweeps up the infalling ambient material and expands into the polar areas, which is then accelerated into an outflow via MHD. Different amounts of collimation have been observed, from well-collimated jets on small scales (Konigl and Pudritz, 2000) to poorly collimated outflows where the outflow takes the form of a wide-angled wind (WAW) (Cunningham et al., 2005). Models can then be divided into two groups, those which are highly collimated and jet driven and those that are poorly collimated and WAW driven. Outflow collimation and shaping have been further explored by Delamarter et al. (2000) and Gardiner et al. (2003) which analyse the effects of inflow ram pressure on outflow collimation and the role of toroidal magnetic fields in shaping the outflow respectively.

- **Disk wind**

  This model assumes that the infalling gas drags the magnetic field lines of the circumstellar disk so that they are at an angle to the disk. When this angle exceeds 60° with respect to the disk plane, the effective gravitational potential along the magnetic field lines overcomes the gravitational potential of the stellar surface. The infalling gas is now in a state of instability which leads to outflows. Magnetically driven outflows are analysed in greater detail by Seifried et al. (2012) and Pudritz et al. (2012).

- **X-wind**

  This is an adaption of the previous two models in the sense that it is a combination of the two. The magnetic field of the circumstellar disk interacts with the magnetic field of the protostar in what is known as an 'X-region'. This occurs in the inner edge of the disk where the ambient material may co-rotate with the star. Infalling matter towards the protostar is then either channeled by field lines connecting the star to the disk or blown back out. For an amount of mass that makes it through to the disk, this model requires that a significant fraction must be ejected back out (Shu and Shang, 1997). This also serves as a mechanism to carry away excess angular momentum in the system. The X-wind model schematic is shown in Figure 1.3.

Outflows have been observed from brown dwarfs (Whelan et al., 2005). Brown dwarfs are substellar objects, meaning they do not possess the required mass to sustain hydrogen fusion. They have a mass range between 13-80 M_J, where M_J is the mass of Jupiter. Above 13 M_J, deuterium burning can take place (Stamatellos, 2014). Outflows have also been observed in O-type stars (Beuther and Shepherd, 2005), which are the most massive type of stars in existence. These findings suggest that the occurrence of outflows is ubiquitous across all star formation. The velocities of outflows are typically supersonic, being up to hundreds of kilometres per second which may influence the degree of collimation (Machida et al., 2007).

14
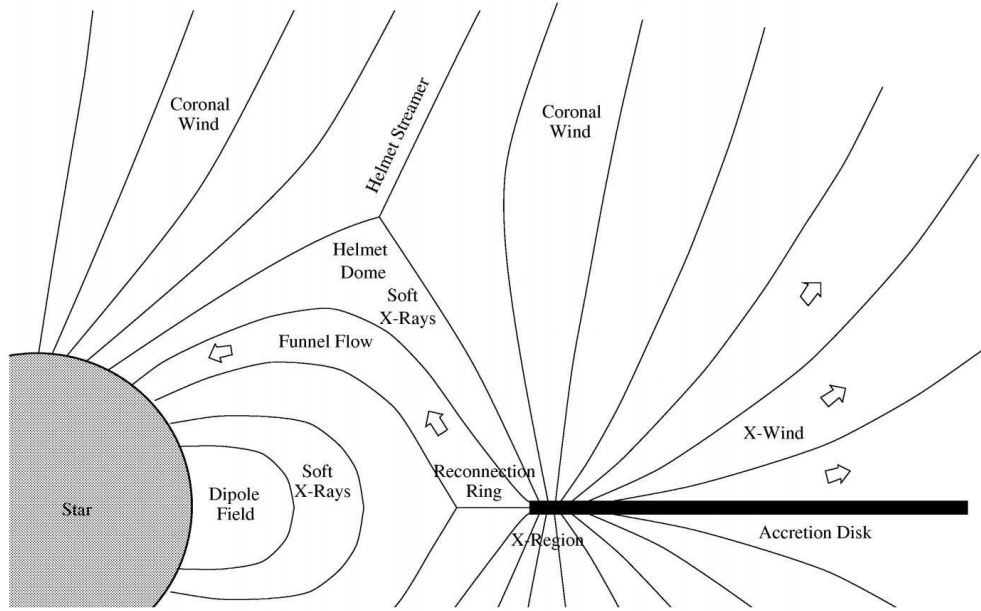
Figure 1.3:   The X-wind model schematic from Shu and Shang (1997).

1.5   Planetary Nebulae

In the later stages of the life of a low to intermediate mass star ($<8\,\mathrm{M_\odot}$), it enters a region on the Hertzsprung-Russell (H-R) diagram known as the asymptotic giant branch (AGB). This occurs after the M-S phase, the red giant phase and the horizontal branch phase as illustrated in Figure 1.4. The horizontal branch phase marks the beginning of the burning of helium and the AGB phase marks the complete burning of helium in the core. The star at this point consists of a dense electron-degenerate core composed of carbon and oxygen. This core is surrounded by a burning shell of helium which is in turn surrounded by a burning shell of hydrogen. Surrounding the burning hydrogen shell is a low density convective outer envelope with a radius extending several hundred $\mathrm{R_\odot}$.

Thermal pulses arise from the temperature increases of the core and helium shell. The temperature increases are due to core contraction and helium fusion in the shell (and dumping of helium 'ash' from the hydrogen burning shell). The star begins to pulsate with an initially low amplitude and short period but eventually

the pulsations grow to have large amplitudes and long periods. This is a catalyst which drives strong outflows that eject the convective envelope and the outer hydrogen shell from the star. The remnants of this process are the much smaller star, known as a white dwarf (WD), and an expanding shell of dust and hydrogen, moving outward into space. The material ejected is subject to photoionisation from the hot white dwarf which illuminates it, creating a planetary nebula (PN, PNe plural). PNe form a brief fraction of stellar lifetime, less than 10^5 yrs (Frew and Parker, 2010).

From Frew and Parker (2010), emission is classed as a PN if it obeys certain observational or physical characteristics. The shape of the emission is one of these characteristics. PNe can have either a round, elliptical or bipolar morphology. Suggested influences in shaping the PN include the central stars rotation (Georgiev et al., 2011) and 'very' late thermal pulses (Frankowski and Soker, 2009). Observational effects can also change the inferences of PN morphology as discussed by Shaw (2012). These include the angular resolution, exposure depth and dynamic range associated with observations. Envelopes of H_2 have been detected around PNe (Jaminet et al., 1991). AGB star outflows contribute large amounts of dust into the ISM which allows for the formation of H_2 in the dense PN environment from the three-body interaction of a dust grain and two HI as described at the start of this chapter. Thus the $1–0\,S(1)$ emission line of H_2 can be observed and used to trace PNe.

1.6 Supernova Remnants

Supernova Process

The common fate for high mass stars (and possibly low mass binaries) is to end their lives in a cataclysmic explosion called a supernova. These events are among the most energetic in Universe and can release as much energy in an instant as some stars can release over billions of years.

High mass stars can become sufficiently hot enough to begin fusion elements heav-
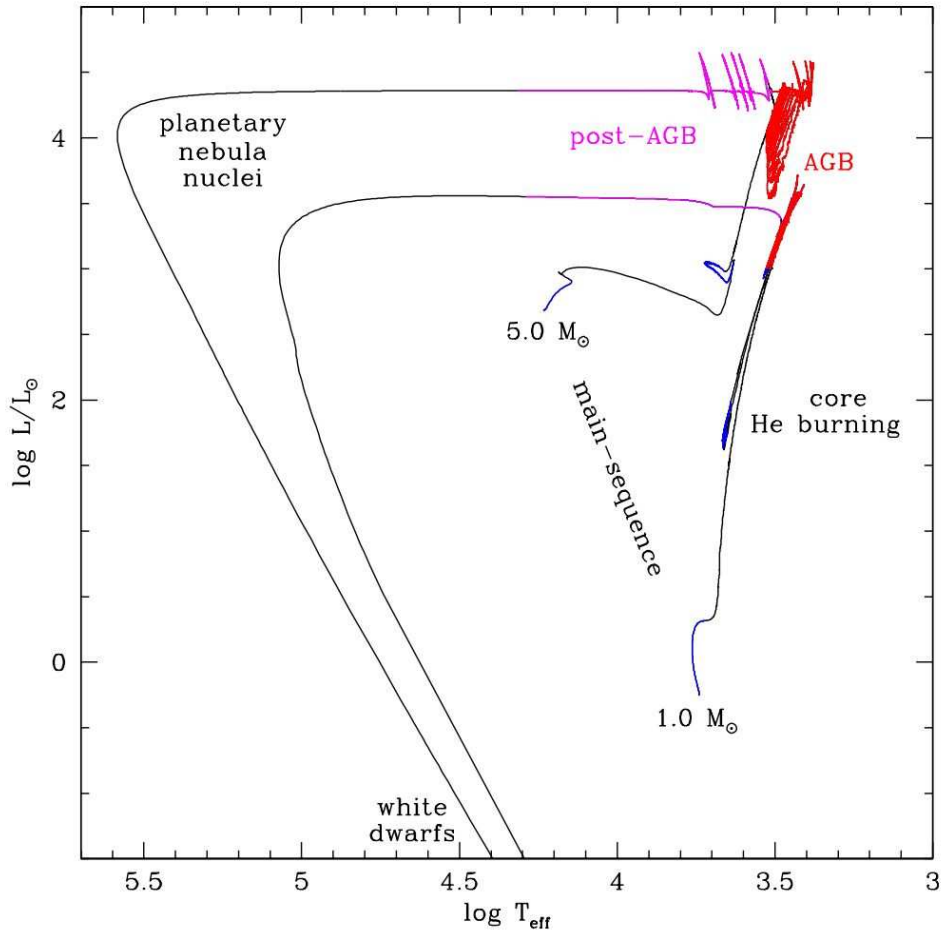
Figure 1.4: The post-M-S H-R diagram from Wood (2010). The stellar structure during the post-AGB phase has changed such that its radius is smaller due to the loss of the envelope and the temperature of the star is increasing at a constant luminosity. This is demonstrated by the horizontal line moving leftwards towards the PN phase.

ier than carbon and oxygen. High mass star cores can fuse elements up to iron before fusion becomes no longer possible. The mass of the core will eventually cause gravitational forces to exceed the electron degeneracy pressure that supports against collapse. This results in the collapse of the core and the outward explosion of all other stellar material in what is known as a Type II supernova explosion. The different types of supernovae will be explained later in this section.

High mass white dwarfs from intermediate mass stars are likely progenitors of Type Ia supernovae. A stable white dwarf can support itself from gravitational collapse due to electron degeneracy pressure. At a certain critical stellar mass, the electron degeneracy pressure gives way to the white dwarf's self-gravity and allows for further collapse. The first attempt to place a value to this critical mass limit was by Chandrasekhar (1931) who predicted the critical mass, known unanimously as the Chandrasekhar limit, to be $\sim 0.91 \, \mathrm{M_\odot}$. He later revised this to about $1.44 \, \mathrm{M_\odot}$ for non-rotating, non-magnetised WDs (Chandrasekhar, 1935), which is much closer to the currently accepted value.

Larger members of an intermediate mass binary pair may acquire the Chandrasekhar limit through accretion of the smaller member which leads to a supernova explosion. This accretion process works such that as the more massive of the binary pair becomes a red giant, it spills gas onto its smaller companion. The remaining core of the giant and the lighter star spiral inwards and co-exist in a common envelope of gas. This envelope gets ejected as the distance separating the binaries decreases. The giant core eventually collapses into a white dwarf. When the companion star starts swelling into a giant, it spills gas onto the white dwarf. This increases the white dwarf's mass to a point which can exceed the Chandrasekhar limit. There are different types of supernovae, with Type Ia and Type II having already been mentioned. The types are defined by the spectra of their supernova remnants (SNR) which is in turn determined by its method of achieving supernova.

- **Type I Supernova**

  The spectra associated Type I supernovae contains no hydrogen lines. There are different subdivisions of Type I supernovae which are:

– **Type Ia**

A supernovae that occurs from the collapse of a WD star in a binary system due to the gravitational pressure overcoming electron degeneracy. It has a single ionised silicon (Si$_{\rm II}$) absorption line at about 615 nm. Type Ia are the brightest type of supernova, which makes them easy to find across the Galaxy. Coupled with this, they make good standard candles as they always collapse at the same mass limit and hence have a known luminosity. The spectra of Ia supernovae are later dominated by ionised iron (Fe$_{\rm II}$ and Fe$_{\rm III}$).

– **Type Ib**

A Type Ib shows either a weak or no Si$_{\rm II}$ line, but does show a non-ionised helium (He$_{\rm I}$) line at 587.6 nm. The progenitors for these are core-collapsing Wolf-Rayet stars, with masses greater than $20\,{\rm M}_\odot$, who have lost their outer layers due to strong stellar winds. Their spectra are later dominated by non-ionised oxygen (O$_{\rm I}$) and ionised cadmium (Ca$_{\rm II}$)

– **Type Ic**

Type Ic show either weak or no Si$_{\rm II}$ or He$_{\rm I}$ lines. Their progenitors are slightly more evolved Wolf-Rayet stars.

• **Type II Supernova**

From the core-collapse of a high mass star. These supernova produce narrow emission lines, including neutral atomic hydrogen (H$_{\rm I}$).

Figure 1.5 from Cappellaro and Turatto (2001) illustrates these typical basic spectra of SNRs from Type Ia, Ib and II supernovae.

Evolution of Supernova Remnants

The post-supernova evolution can be split into three phases. The first is:

• **The free expansion phase**

The energy and density of the material ejected in the process currently ex-
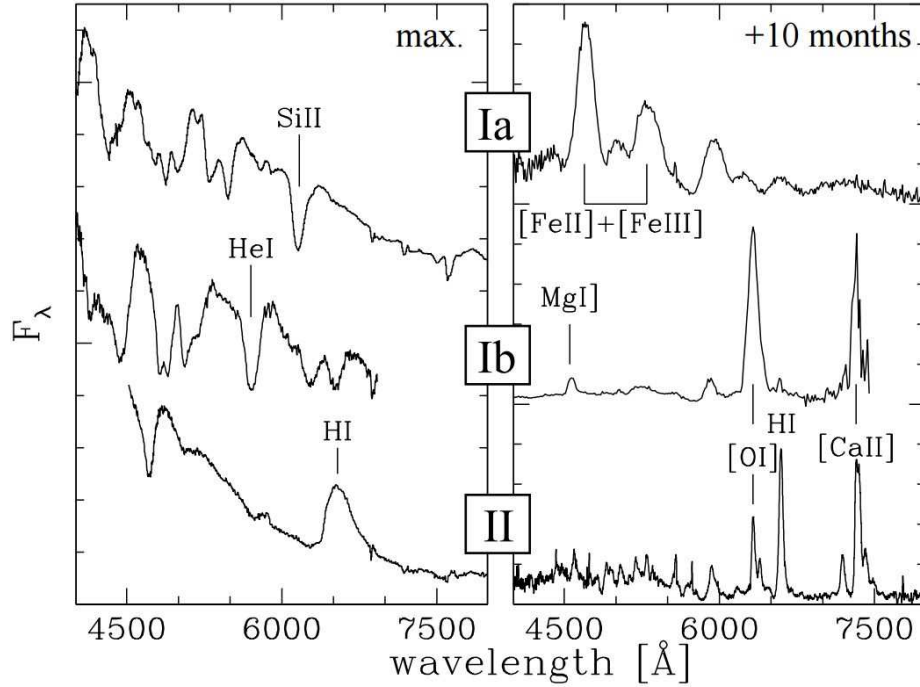
Figure 1.5: The spectra of Type Ia, Ib and II supernovae which near maximum (left) and the spectra ten months later (right). Obtained from Cappellaro and Turatto (2001).

ceeds the values of the surrounding medium by a very large amount. The material expands freely as if the medium were negligible (vacuum-like). As the supernova shock wave (which is very supersonic) propagates, it sweeps up the ISM that lies within its path, forming an expanding shell. The mass of swept-up material is small compared to the ejected mass such that:

$$m_{eject} \gg \frac{4\pi}{3} R_{shell}^3 \cdot \rho \tag{1.8}$$

where m_{eject} is the mass of material ejected in the supernova and R_{shell} is the radius of the shell measuring from the forefront of the shock to the stellar remnant (neutron star or black hole) and contains the swept up ISM. The density is equal to the product of the mean mass per hydrogen, μ, the atomic hydrogen density in the surrounding medium, n_{shell} and the hydrogen atom mass, m_h. This radius is constantly evolving as the wave propagates until the swept-up mass equals the ejected mass, therefore doubling the SNR's initial

mass, or m_{eject}. This occurrence is the classical criteria for determining when a SNR has had a significant impact on its surroundings. At this point R_{shell} becomes:

$$R_{shell} = \left(\frac{3 \cdot m_{eject}}{4\pi \cdot \mu \cdot n_{shell} \cdot m_h}\right)^{\frac{1}{3}} \tag{1.9}$$

The time taken for this to occur is known as the sweep-up time and is $t_{sweep} = R_{shell}/v_{eject}$, where v_{eject} is the ejection velocity of the gas. Assuming most of the supernova energy, E_{eject}, is converted into kinetic energy, the ejection velocity can be:

$$v_{eject} = \left(\frac{2E_{eject}}{m_{eject}}\right)^{\frac{1}{2}} \tag{1.10}$$

At this stage, the expansion of the SNR begins to be affected, hence 'free' expansion ends. A reverse shock travels inwards, heating up the ejected gas to high temperatures. Further expansion is hence driven by thermal pressure.

- **The adiabatic phase**

  Also known as the Sedov-Taylor phase from Taylor (1950) and Sedov (1959), the gas of the SNR is so hot that radiation energy loss is small, hence adiabatic. We make the following assumptions:

  1. The surrounding material density, ρ, is homogeneous.

  2. The ram pressure of the shock, ρv_{eject}^2 is much higher than the pressure of the surrounding gas.

  3. Radiative energy loss at shock front is small compared to the energy of the ejection, E_{eject}.

  As the initial energy of the supernova and the surrounding density describe the evolution of the remnant over time, we can consider dimensional analysis of E_{eject}/ρ. The results of which can be seen next.

$$x = r \cdot t^\alpha \cdot \rho^\beta \cdot E_{eject}^\gamma$$

r has dimensions l, t has t, ρ has m/l^3 and E_{eject} has dimensions ml^2/t^2.

$$x = l^{1-3\beta+2\gamma} \cdot t^{\alpha-2\gamma} \cdot m^{\beta+\gamma}$$

$$1 - 3\beta + 2\gamma = \alpha - 2\gamma = \beta + \gamma = 0 \text{ (as dimensionless)}$$

Solution

$$\alpha = -\frac{2}{5}$$

$$\beta = \frac{1}{5}$$

$$\gamma = -\frac{1}{5}$$

This results in the following time dependent R_{shell}

$$R_{shell}(t) = x_0 \cdot \left(\frac{E_{eject} \cdot t^2}{\rho}\right)^{\frac{1}{5}} \tag{1.11}$$

where x_0 is the normalisation factor and is to be determined. The speed of the shock front, v_s, is determined by the time differential of R_{shell}, which is $2R_{shell}/5t$. The post-shock temperature can be determined from the Rankine-Hugoniot jump conditions. The post-shock pressure and density, denoted by P_s and ρ_s respectively, are:

$$P_s = \frac{2\rho v_s^2}{\gamma + 1} \tag{1.12}$$

$$\frac{\rho_s}{\rho} = \frac{\gamma + 1}{\gamma - 1} \tag{1.13}$$

where γ is the specific heat ratio. Combining v_s with Equations 1.12 and 1.13, along with the ideal gas law:

$$P_s = \frac{k}{\mu \, m_h} \rho_s \, T_s \tag{1.14}$$

will result in the following equation for the post-shock temperature:

$$T_s = \frac{2(\gamma - 1)}{(\gamma + 1)^2} \cdot \frac{\mu \, m_h}{k} \cdot x_0^2 \left[\frac{2}{5} \left(\frac{E_0}{\rho \cdot t^3} \right)^{\frac{1}{5}} \right]^2 \tag{1.15}$$

Thus the post-shock temperature is proportional to $t^{-\frac{6}{5}}$ which means that gas shocked at early stages (smaller radii) has higher temperature.

- **Cooling or 'snow plough' phase**

  The adiabatic phase continues until the temperature behind the shock front decreases to around 10^6 K. Ionised atoms can start to capture free electrons in the gas, radiating their excitation energy. The outer layers of the SNR radiate their energy before forming a thin, cold and dense shell. The thermal pressure in post-shock regions decreases. Only a fraction of the initial energy is available to drive the expansion. The expansion of R_{shell} becomes proportional to $t^{\frac{2}{7}}$, which translates to a time differential expansion speed of $2R_{shell}/7$t. Thus the expansion rate of the SNR has decreased. As more mass is swept up, the SNR breaks into clumps and the velocity eventually becomes subsonic, allowing the ejected matter to disperse into the ISM.

Because of the large-scale and highly energetic nature of these events, shock fronts from supernova are key to manipulating the ISM and creating density fluctuations that can eventually become star forming regions. The 1–0 S(1) emission line of H_2 traces shocked regions that have been swept up by the SNR blast wave.

1.7 Photo-dissociation and HII regions

HII regions

Once a high mass star (such as an OB star) forms in a GMC, it produces large amounts of high energy radiation. This includes extreme ultraviolet radiation (EUV) with wavelengths in the range of $10\,\mathrm{nm}$ to $\gtrsim 100\,\mathrm{nm}$ and energies $> 13.6\,\mathrm{eV}$, the energy required to ionise hydrogen. The OB star ionises the gas surrounding its natal GMC, creating a HII region. Excess energy is spent heating the HII region to temperatures of about $10^4\,\mathrm{K}$ (Anderson et al., 2009). The pressure differences between the cloud and the HII region causes the ionisation front to expand into the cloud. There is a variety of sizes of HII regions, summarised in Table 1.3.

HII region size

Assuming a thin shell of gas with a surface boundary that separates the ionised material inside its volume and non-ionised outside. It extends to a radius R from the ionising star and has a shell thickness dR. The gas density is n, hence the number of particles is $4\pi R^2 n \cdot dR$. The number of ionising photons per second from the star is dN and the radius of the shell grows by the shell thickness, dR. Assuming each photon ionises a hydrogen atom:

$$\frac{dN}{dt} = 4\pi R^2 n \frac{dR}{dt} \tag{1.16}$$

The HII region will eventually be in equilibrium with the ionisation and recombination rate of ions and electrons. However, whilst it still expands, ions and electrons recombine at a rate α. At temperatures of $10^4\,\mathrm{K}$, $\alpha \approx 2 \times 10^{-19}\,m^3 s^{-1}$. Modifying the above equation to allow for the recombination rate:

$$\frac{dN}{dt} - \frac{4\pi R^3}{3} \cdot n_i \cdot n_e \cdot \alpha = 4\pi R^2 n \frac{dR}{dt} \tag{1.17}$$

where n_i and n_e are ion and electron densities. When the rates are eventually in

Table 1.3: Table showing the size, density and ionised mass properties of HII regions. Information obtained and adapted from Franco et al. (2003).

Class of region	Size [pc]	Density [cm^{-3}]	Ionised mass [M$_\odot$]
Hypercompact	~ 0.003	$\gtrsim 10^6$	$\gtrsim 10^{-2}$
Ultracompact	$\lesssim 0.1$	$\gtrsim 10^4$	$\sim 10^{-2}$
Compact	$\lesssim 0.5$	$\gtrsim 5 \times 10^3$	~ 1
Classical	~ 10	~ 100	$\sim 10^5$
Giant	~ 100	~ 30	$10^3 - 10^6$
Supergiant	> 100	~ 10	$10^6 - 10^8$

equilibrium, the expansion will cease, leading to $dR/dt = 0$. The ionising flux from the star, dN/dt is called S_* and the radius of the shell at equilibrium is known as the Strömgren radius, R_S (Strömgren, 1939)), and is:

$$R_S = \left(\frac{3 \cdot S_*}{4\pi \cdot n_i \cdot n_e \cdot \alpha} \right)^{\frac{1}{3}} \tag{1.18}$$

The final size is typically larger because the ionisation will double the number of particles within the volume of the shell, creating an extra internal pressure, $P = 2 \cdot n_i \cdot kT_i$. This additional pressure makes the final HII region radius:

$$R = \left(\frac{2T_i}{T_n} \right)^{\frac{2}{3}} \cdot R_S \tag{1.19}$$

Photo-dissociation Regions

As well as EUV radiation, high mass stars also produce far ultraviolet radiation (FUV), with wavelengths spanning roughly $100 - 200$ nm and energies that are $<$ 13.6 eV but high enough to dissociate and ionise most molecules with low ionisation potentials. FUV radiation forms photo-dissociation regions (PDRs), which exist beyond the ionisation front – between the HII region and neutral MC. They regulate the heating and influence the chemistry of predominantly neutral regions of the ISM.

The boundary of the PDR closest to the central star experiences ionisation whereas the boundary furthest from the star (and closest to the neutral cloud) is mostly molecular. PDRs are a very rich source of both atomic hydrogen and the H_2 molecule (Hollenbach and Tielens, 1997).

Hollenbach and Tielens (1999) discusses the presence of PDRs in the ISM. Whilst well known for occurring on the boundary of molecular clouds and HII regions, they can also occur in other cold, dense and neutral matter such as around PNe. The presence of PDRs around PNe and their physical properties has been investigated by Tielens and Hollenbach (1993).

1.8 Thesis Layout

In this thesis I present an overview of UWISH2 observations and subsequent data reduction, followed by an explanation of the photometry process and an analysis of said photometry performed on extended H_2 emission sources. The structure of this thesis is as follows:

- **Chapter 2:** I provide descriptions of the observation procedures and data processing necessary for the production of H_2 – K difference images that are required for the detection of H_2 emission sources. I describe how H_2 sources are detected and classified as one of four types of emission source – either jets/outflows, PNe, SNRs or PDRs.

- **Chapter 3:** I explain how photometry is performed on the H_2 – K difference images.

- **Chapter 4:** I present an analysis of the spatial distributions, areas and fluxes of the individual, non-grouped H_2 source. This includes the summary of how much of the H_2 emission area and flux is located at different locations and further separate this into the different types of sources.

- **Chapter 5:** Following a grouping procedure which I explain, I present the analysis of the spatial distributions, areas and fluxes of the grouped H_2 sources.

- **Chapter 6:** I present a comparison of flux estimates from two different types of photometry and analyse their agreement with one another.

- **Chapter 7:** I analyse the signal to noise ratios associated with each individual, non-grouped H_2 emission source.

- **Chapter 8:** I provide a summary of currently ongoing and future projects associated with this research.

- **Chapter 9:** I provide a conclusion of this research.

- **Bibliography**

- **Appendices**

Chapter 2

The UWISH2 Survey

2.1 UWISH2

The United Kingdom Infrared Telescope (UKIRT) Widefield Infrared Survey for H_2 (UWISH2) is an unbiased, narrowband imaging survey covering a total area of 286.45 square degrees. Of that area, roughly 209 square degrees is devoted to the inner Galactic Plane (GP), spanning from $l \approx 357°$ to $l \approx 65°$ and $b \approx \pm1.5°$. The remaining area is split between approximately 42 square degrees and 35.5 square degrees for high dust column density regions in Cygnus and Auriga respectively. The survey uses the 1–$0\,S(1)$ emission line of H_2, corresponding to a wavelength of $2.122\,\mu m$, as a tracer for jets/outflows, PNe, SNRs and PDRs. Figure 2.1 shows the area of the GP where UWISH2 tiles have been imaged. Figure 2.2 shows the areas of Cygnus and Auriga imaged in UWISH2. The background of these figures show $100\,\mu m$ dust emission from the Infrared Astronomical Satellite (IRAS). Figure 2.3 shows the relative coverage at Galactic longitudes and latitudes of the GP. Figure D.1 in Appendix D shows the relative coverages for Cygnus and Auriga. UWISH2 data exists in the form tiles. From this point on, regarding UWISH2 tiles and images, a tile is composed of 16 images in a 4×4 square grid. All tiles and images can be viewed online[1].

---

[1]astro.kent.ac.uk/uwish2
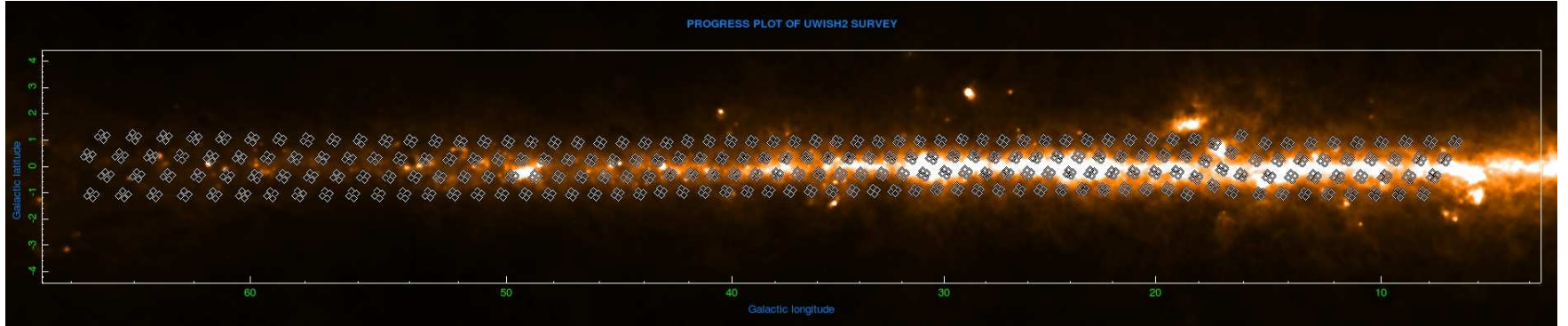
Figure 2.1: A map indicating imaged areas of the GP by UWISH2. The square symbols correspond to one tile. They are overlaid on top of a $100\,\mu m$ IRAS dust emission image. No gaps exist between the tiles.

Table 2.1: Table summarising the number of outflows detected in previous surveys. Cygnus-X has been included as it is an upcoming product of UWISH2.

Region	Coverage [deg^2]	Number of outflows	Relevant publication
Orion A	1.2	76	Stanke et al. (2002)
DR 21/W75N	0.8	50	Davis et al. (2007)
Taurus-Auriga-Perseus	140	26(in 4 deg^2)	Davis et al. (2008)
Orion A	8	116	Davis et al. (2009)
Serpens and Aquila	33	131	Ioannidis and Froebrich (2012a)
Cygnus-X	42	500+ expected	Makin et al. (in prep)

2.2 Previous H₂ Surveys

Previous work involving H$_2$ surveys includes the search for protostellar jets in the Orion A GMC by Stanke et al. (2002). The survey covered 1.2 square degrees and resulted in the identification of 76 candidate outflows. Another example by Davis et al. (2007) covered 0.8 square degrees and investigated the star forming region DR 21/W75N, resulting in knots and bow shocks attributed to 50 individual outflows. Another paper by Davis et al. (2008) investigated a survey of the Taurus-Auriga-Perseus complex, finding 26 individual outflows within the NGC 1333, L1455, L1448 and Barnard 1 (B1) star forming regions in Perseus. Orion A was re-investigated by Davis et al. (2009) where an 8 square degree region was found to contain 116 outflows. An analysis of UWISH2 data covering 33 square degrees of Serpens and Aquila by Ioannidis and Froebrich (2012a) found 131 jets and outflows from YSOs, significantly increasing from the previously known number. Table 2.1 summarises these previous works.

With exception to Ioannidis and Froebrich (2012a) that was part of UWISH2, two common traits of all these surveys is that they i) increase the number of previously known outflows, furthering our understanding of the star forming environment and ii) are all biased as well known star forming regions were specifically targeted for investigation. There is also the problem of basic properties of the
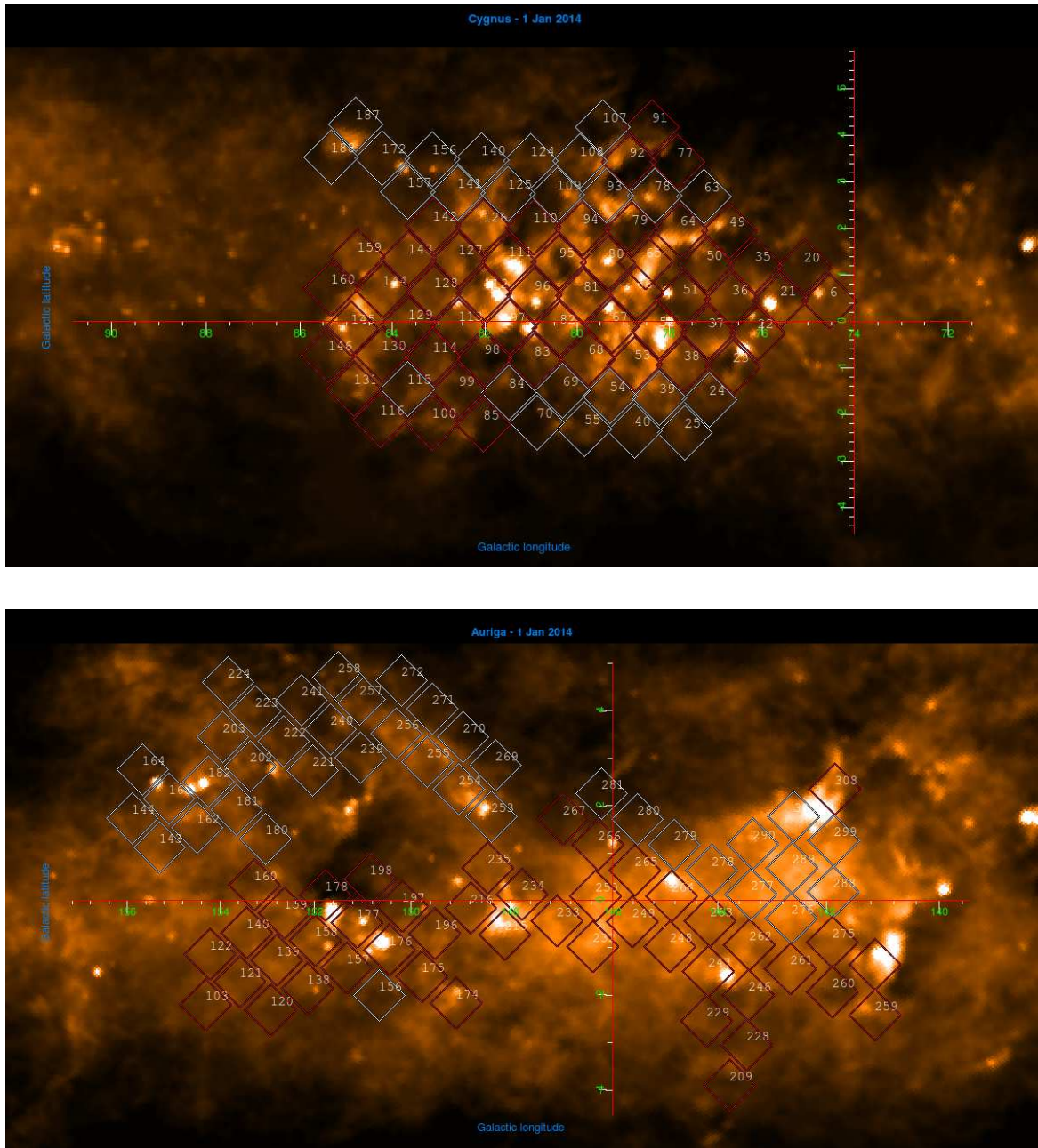
Figure 2.2: **Top:** Cygnus. **Bottom:** Auriga. Maps showing the areas of Cygnus and Auriga covered by UWISH2. Squares indicate tile positions. Due to observation time running out, only certain sections of these two regions were covered. The red squares indicate tiles that have been imaged whilst white squares indicate tiles that were not, albeit planned. Squares are overlaid on top of $100\,\mu m$ IRAS dust emission images.
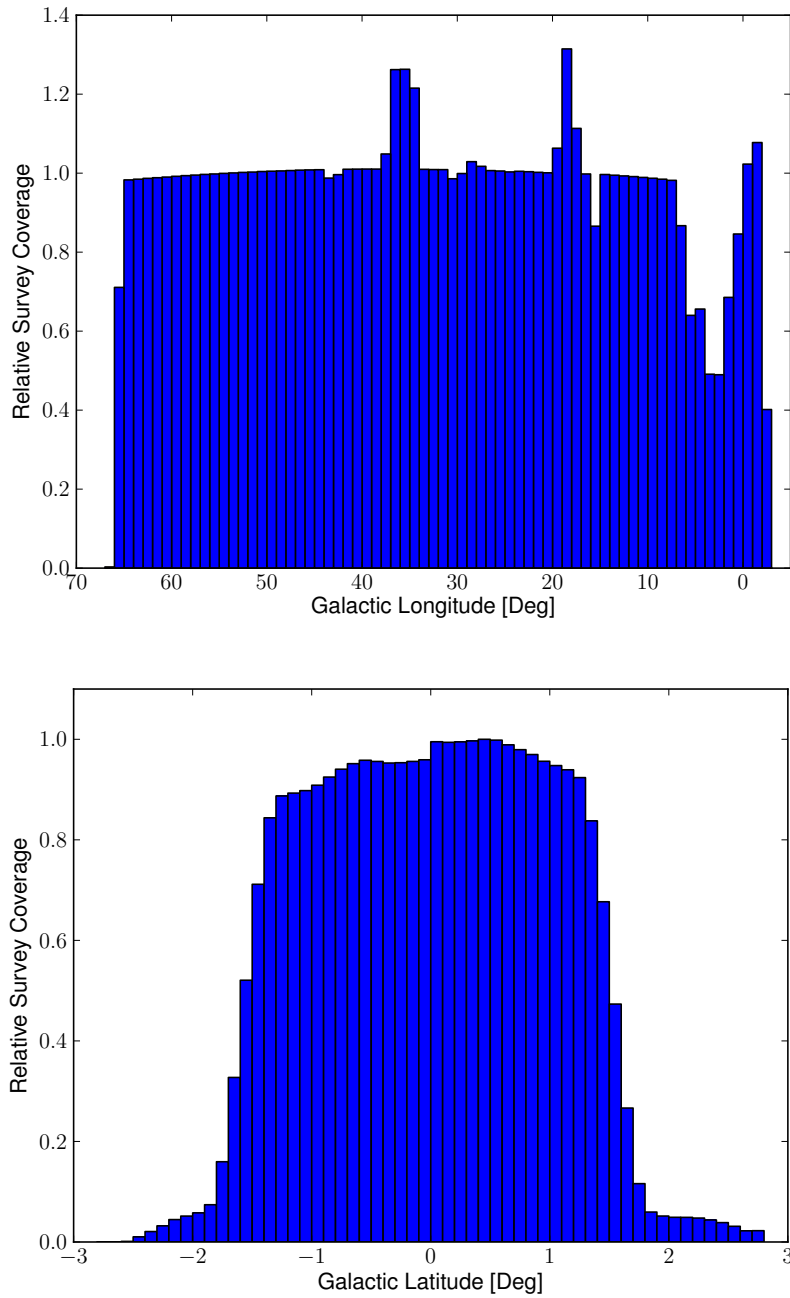
Figure 2.3: Top: Galactic longitude. **Bottom:** Galactic Latitude. Histograms showing the relative coverages at certain Galactic longitudes and latitudes of the GP. We can see that the majority of the GP was covered near-homogeneously.

outflows in different regions not always agreeing, making it difficult to form conclusions. UWISH2 is therefore unique in the sense that it is a survey that does not target a specific MC or a series of MCs, but instead covers a much larger area without selection bias. This allows for the creation of a catalogue of various H_2 emission objects (including outflows) across a large area. This is also the first time that such a large scale survey of H_2 emission has been carried out.

2.3 UKIRT and WFCAM

The UKIRT is a 3.8 m telescope situated on the summit of the Hawaiian dormant volcano, Mauna Kea. As its name suggests, it is dedicated to infrared astronomy. The UKIRT observatory houses the Wide Field Camera (WFCAM) imaging instrument which all data was acquired from. WFCAM uses four Rockwell Hawaii-II (HgCdTe 2048×2048) detectors where the gap between adjacent detectors is 94% of the detector width. The schematic of the detectors can be seen in Figure 2.4. A technical discussion of WFCAM has been prepared by Casali et al. (2007).

The pixel scale is 0.4" but a 2×2 micro-stepping pattern is repeated at three jitter positions during observations. At each jitter position, a 6.4" offset was applied, with micro-step offsets of ± 1.4". This allowed for 12 exposures to be acquired for each telescope pointing and has also led to the pixel scale decreasing from 0.4" to 0.2" in the final images. Exposures were through a narrowband H_2 filter ($\lambda = 2.122 \, \mu m, \delta\lambda = 0.021 \, \mu m$). The exposure time was 60 seconds which resulted in a 720 second integration time for each pixel after the micro-stepping (Froebrich et al., 2011). Additionally, the field of view after 2×2 micro-stepping (a single image tile) covers 0.79 square degrees of sky, compared to the single shot field of view that covers 0.21 square degrees. Tile areas in UWISH2 are roughly 0.75 square degrees. With the exception of the filter and exposure time, the UWISH2 survey used a similar observing strategy seen in the Galactic Plane Survey (GPS)
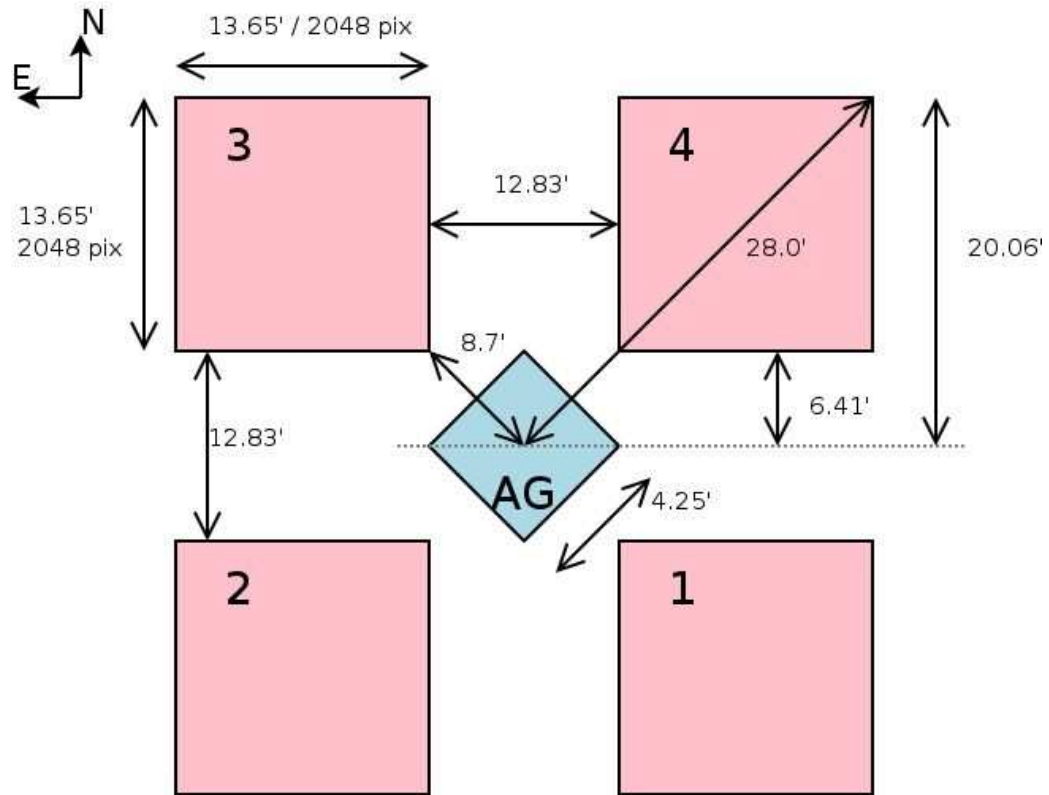
Figure 2.4:   Schematic of the focal plane layout of WFCAM. Detector (pink square) dimensions are $13.65' \times 13.65'$ and the spacing between adjacent detectors is 12.83', or 94% of the detector width.

by Lucas et al. (2008), which is one of five surveys known collectively as the UKIRT Infrared Deep Sky Survey (UKIDSS, Lawrence et al. (2007)).

2.4 Calibrations and Continuum Subtraction

The WFCAM data was then reduced by the Cambridge Astronomical Survey Unit (CASU) in a process described by Dye et al. (2006). After data reduction, images can still contain artefacts which mimic H_2 objects, so it is important to be aware as they will lead to false detections later. The astrometric calibrations were achieved using the co-ordinates of objects in the Two Micron All Sky Survey (2MASS, Skrutskie et al. (2006)) point source catalogue. Unsaturated WFCAM sources were matched with 2MASS objects (with errors $< 0.1\,\mathrm{mag}$) for the photometric calibration. Astrometric and photometric calibrations have been described by Dye et al. (2006), Hewett et al. (2006) and Hodgkin et al. (2009). The 2MASS photometry is then transformed into the WFCAM ZYJHK system using the following empirically derived colour equations from Dye et al. (2006):

$$Z_{WFCAM} \;=\; J_{2MASS} + 0.95\,(J_{2MASS} - H_{2MASS}) \tag{2.1}$$

$$Y_{WFCAM} \;=\; J_{2MASS} + 0.50\,(J_{2MASS} - H_{2MASS}) \tag{2.2}$$

$$J_{WFCAM} \;=\; J_{2MASS} - 0.075\,(J_{2MASS} - H_{2MASS}) \tag{2.3}$$

$$H_{WFCAM} \;=\; H_{2MASS} + 0.04\,(J_{2MASS} - H_{2MASS}) - 0.04 \tag{2.4}$$

$$K_{WFCAM} \;=\; K_{2MASS} - 0.015\,(J_{2MASS} - K_{2MASS}) \tag{2.5}$$

The reduced images from CASU were not continuum subtracted, but continuum subtracted images are necessary because they will emphasise the emission associated with H_2 sources (jets/outflows, PNe, SNRs and PDRs). K-band data from the GPS was used to remove the continuum emission from the H_2 narrowband images on an image by image basis. H_2 images from UWISH2 and K-band images from

the GPS are aligned based on the World Co-ordinate System (WCS).

The first attempt at continuum subtraction required both images to be Gaussian smoothed to compensate for different seeing conditions and enhancement of the signal to noise ratio. This process is described by (Ioannidis and Froebrich, 2012a). Note that by doing this, it is possible to dilute the signal for some of the weak, small extended H_2 features, possibly below the detection threshold. In an attempt to completely remove the continuum sources, the K-band images needed to be scaled with a scaling factor (sc). The final $H_2 - K$ difference images were created via:

$$H_2 - K \text{ Difference Image } = H_2 - K \cdot sc \qquad (2.6)$$

However, continuum subtraction was later redone using a new method described by Lee et al. (2014). The image subtraction procedure astrometrically aligns the H_2 image to the corresponding K-band image and determines the scaling factor for the continuum image. Point-spread-function (PSF) fitting is then used to remove most of the point-like continuum sources from both images. The K-band image with removed point sources is then subtracted from the H_2 image with point sources removed. This is done to remove extended continuum sources that went undetected. The quality of the final $H_2 - K$ difference images was improved using this method.

For every image, full resolution near-infrared JHK, JHH_2 and JKH_2 colour composites have been created alongside the $H_2 - K$ difference images. These images can be acquired online from the UWISH2 website[2].

2.5 Source Detection

The majority of real H_2 features in the images are of low brightness and spatially resolved but are projected onto a spatially variable background. Therefore it is necessary to filter images to remove all remaining point sources that survived con-

[2]astro.kent.ac.uk/uwish2

tinuum subtraction and subtract the local background from the H_2 – K difference images to correct for any large variable background. To accomplish the point source removal, all objects smaller than 2" $\times$ 2" (100 pixels) that have a pixel value exceeding the 5σ noise are replaced with the local background. The local background is determined as the median pixel value within a 20" range (Froebrich et al., 2015). H_2 sources were automatically detected in the background subtracted, point source filtered images if the source area was four square arcseconds (100 pixels) or greater and had pixel values above half the root-mean-square (RMS) noise. Detected H_2 sources are enclosed in a polygon via contour plotting in ds9[3]. These closed contour sources are referred to as 'regions' for the remainder of this paragraph. The minimum size limit is a further guarantee that surviving point sources do not get detected. Furthermore, every region that had a 2MASS point source within three arcseconds from the region centre is rejected so as to remove saturated stars. Many bright stars also showed diffraction rings which get automatically detected. Therefore, every region within 35" of a diffraction ring star was rejected. Finally, all regions that are identified and are within 10" from the edge of the image are discarded. The overlap between images is generally larger than 10" so there should be no loss of objects. Figure 2.5 shows different types of artefacts encountered in the H_2 – K difference images, including diffraction rings from a bright star (top right).

2.6 Source Classification

H_2 regions that have survived rejection criteria will be referred to as features or H_2 features from this point on. The feature is manually classified as belonging to either a jet/outflow, PN, SNR or a PDR. Jet/outflow features are primarily identified based on the shape of their emission, as well as other factors such as their colour in the JKH_2 colour images and whether they are in proximity to known star forming regions. For PNe, the structure of the emission is typically ring-like or

---

[3]ds9.si.edu/site/Home.html
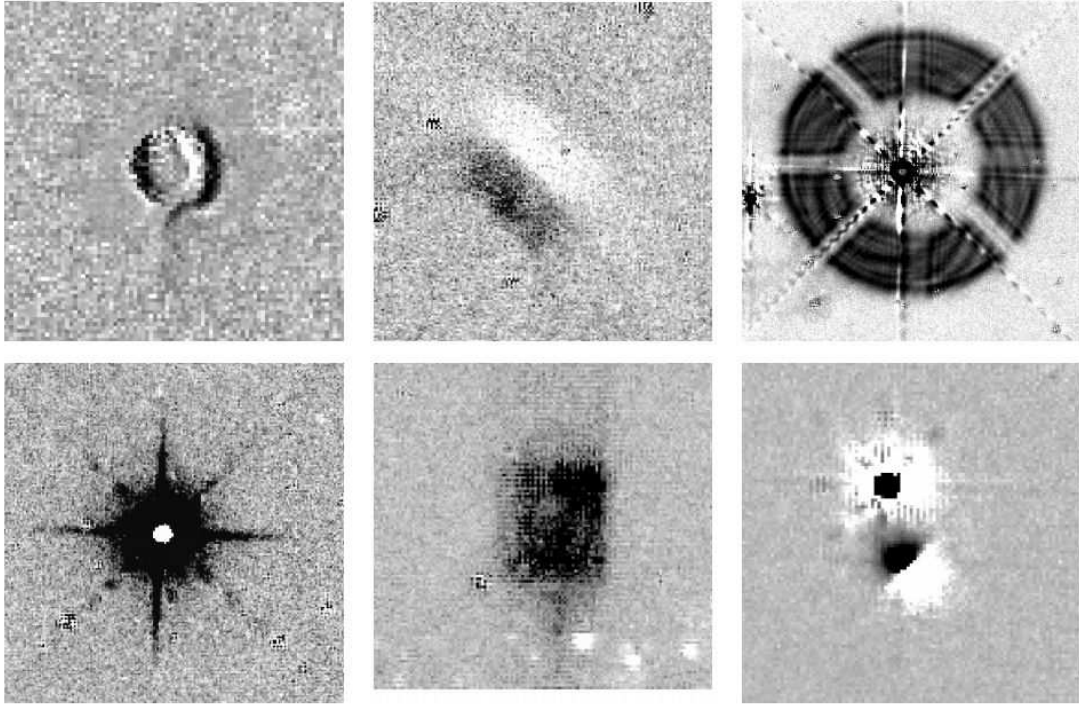
Figure 2.5: Example of false positives in the H$_2$ – K difference images from Froebrich et al. (2015). Colour is inverted so bright regions appear dark. From the top left to the bottom right, the panels show the following: i) electronic cross-talk from bright stars; ii) reflections from very bright stars; iii) diffraction rings around bright stars; iv) a variable (brighter during H$_2$ imaging) and saturated star; v) reflection from a bright star just outside the edge of an image; vi) high proper motion star (next to variable star – fainter during H$_2$ imaging.

bipolar and can possibly be even more complex. It is important to check that the feature is not related to any identifiable star forming region. Shape is not always a guaranteed classification method as a bipolar PN may be indistinguishable from a bipolar jet from a YSO. We checked for known PNe at the location of the candidate H_2 feature and designated the feature as such if it was within a few arcseconds of a known PN. For this we utilized PNe entries from SIMBAD[4] and catalogues from IPHAS (Sabin et al., 2014), MASH (Parker et al., 2006) and MASH2 (Miszalski et al., 2008). Newly discovered PNe candidates were identified based on whether their emission looks similar to previously known members. If a feature has a close proximity to a known SNR from Green (2009) and shows no obvious PN or jet/outflow-like characteristics then it is classified as a SNR. Additionally, if a feature shares little resemblance to H_2 emission observed in other SNRs then it remains unclassified. Any remaining H_2 features that haven't been classified as either belonging to a jet, PN or SNR remain unclassified. It is likely that a large majority of these features are part of a PDR surrounding a Hɪɪ region. Because of this, all of the unclassified features are henceforth treated as a part of a PDR from now on. In the final UWISH2 catalogue, a specific feature type can be identified as belonging to either a jet, PN, SNR or PDR based on a single-letter classifier 'j', 'p', 's' and 'u' respectively. An example of each feature is provided in Figure 2.6. After the identification of all individual features was complete, another program was used to group together local features of the same classification. This will be further explained in Chapter 5.

---

[4]simbad.u-strasbg.fr/simbad
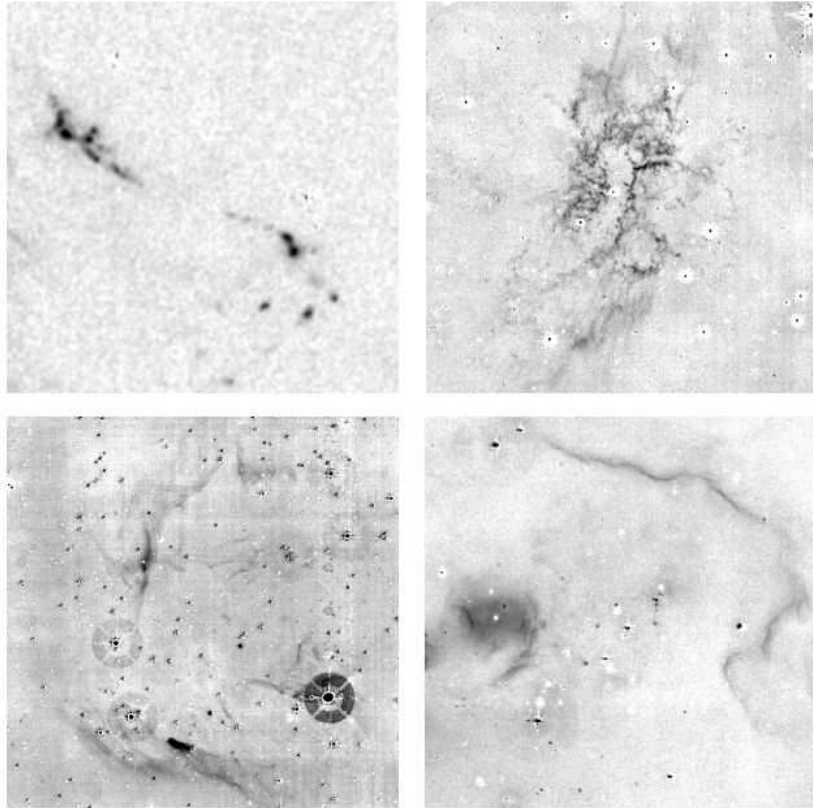
Figure 2.6: Example from Froebrich et al. (2015) of real objects in the $H_2 - K$ difference images that represent each of our feature types. Darker regions in the image represent brighter features. The panels, from top left to bottom right, show i) 'j' features from IRAS 20294+4255; ii) 'p' features from PN SH 21-71; iii) 's' features from SNR G11.2 – 0.3 and iv) 'u' features from emission near the cluster VDB 130.

Chapter 3

Photometry

3.1 UWISH2 H_2 Features

One objective of UWISH2 is performing the photometry of sources of molecular hydrogen emission within the GP, Cygnus and Auriga. I have developed a program, seen in Appendix A, which will accomplish this for the H_2 features. All images in the survey use a Flexible Image Transport System (FITS) format with image dimensions of approximately $4k \times 4k$ pixels. As detailed in previous work by Froebrich et al. (2015), each background subtracted image has previously been passed through another program which identifies extended molecular hydrogen sources. The program encapsulates each feature in a polygon with vertices characterizing co-ordinate points. Co-ordinate points are of the form of the non-integer x and y pixel numbers in the image, but astronomical co-ordinate systems can be used via the FITS WCS. The polygon can have as many co-ordinate points as desirable to best fit the shape of the source. The feature subsequently has its vertex co-ordinates exported to a text file with all other features from the same image. An example H_2 feature is shown in Figure 3.1.
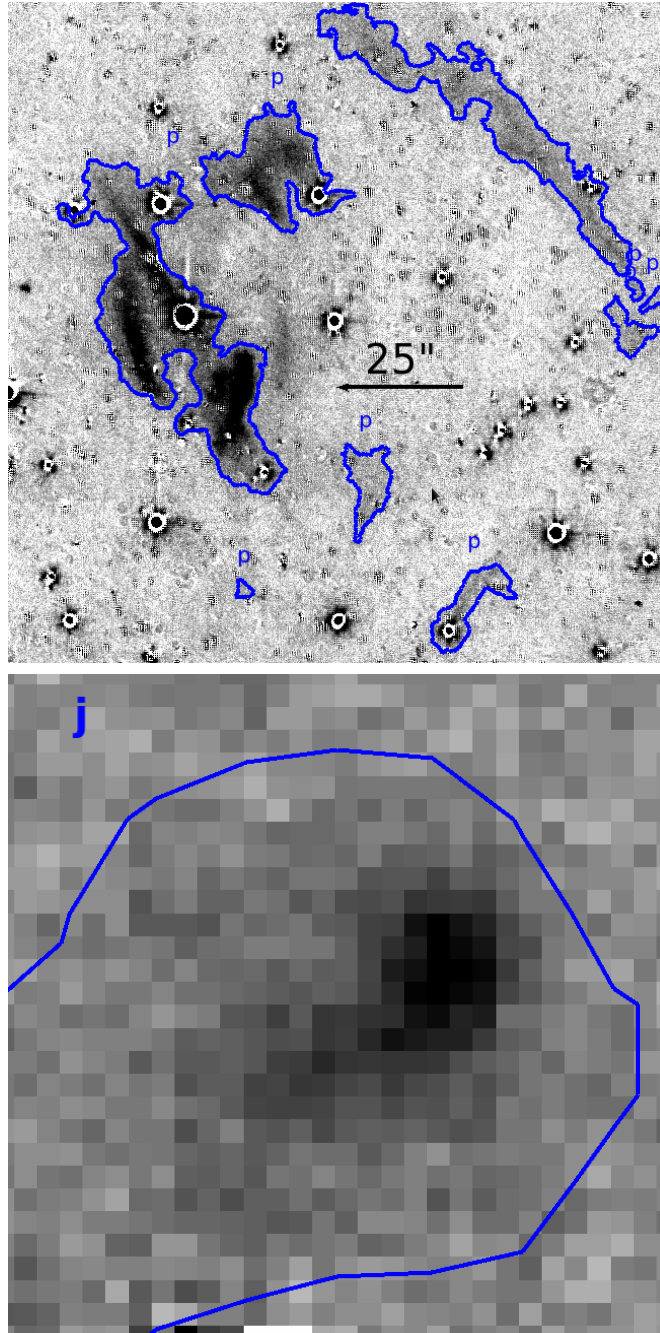
Figure 3.1: Example of real H$_2$ emission features, from the image *w20130919_00162_w*, contained within polygons (top). The features have been manually classified as belonging to a PN, denoted by the adjacent 'p'. It should be noted that these features have been grouped as a single PN. Below is a magnified section of the outflow designated in the catalogue as *UWISH2_035.15688-0.82647*. It is apparent that the pixel intensities contained within the feature contrast those in the background. The line connecting two vertices can bisect several pixels and part of the photometry code determines whether a bisected pixel's intensity is included in the photometry. Here, darker pixels indicate higher intensities.

3.2 My Program

Area and Location of Features

From the file containing the co-ordinates that describe the shape of the H_2 feature, my program reads the geometric information of one feature at at time and follows the perimeter in an anti-clockwise direction and, using said co-ordinates, calculates the area, A, of each feature as well as the centroid co-ordinates (C_x, C_y) via:

$$A = \frac{1}{2} \sum_{i=0}^{N-1} (x_i \, y_{i+1} - x_{i+1} \, y_i) \tag{3.1}$$

$$C_x = \frac{1}{6A} \sum_{i=0}^{N-1} (x_i + x_{i+1})(x_i \, y_{i+1} - x_{i+1} \, y_i) \tag{3.2}$$

$$C_y = \frac{1}{6A} \sum_{i=0}^{N-1} (y_i + y_{i+1})(x_i \, y_{i+1} - x_{i+1} \, y_i) \tag{3.3}$$

where x_i, y_i and x_{i+1}, y_{i+1} are any pair of neighbouring vertices. These equations require that the initial co-ordinate pair serve as the final co-ordinate pair $(x_0, y_0 = x_N, y_N)$ to complete the perimeter. Should the co-ordinates be read in the clockwise direction, the area will be a negative of its otherwise correct value.

Determining Whether Pixels are Inside a Feature

Every feature has characteristic maximum and minimum x and y co-ordinate values which are utilized as corner co-ordinates to create a box that can contain the entire feature. For each pixel inside the box, my program will determine whether it is inside or outside the feature boundary. For a pixel to be included in the feature I set the condition that if the top right corner of a pixel is within the feature boundary then it is inside. To determine this, my program will start at the top-right of a pixel and advance in a linear direction whilst counting the number of intersections with the feature boundary. This will continue until it reaches the boundary of the

43

box. Should the final number of intersections be zero or an even number, then we can conclude the pixel is outside the feature. This is because a straight line leaving the pixel will either never intersect before reaching the box or it will intersect once to enter the feature and once more to exit, possibly multiple times. Pixels with an odd number of intersections are deemed to be inside as they will have to intersect once to leave the feature or three times to leave, enter and leave and so forth. I can justify the top right of a pixel as being the benchmark for inclusion as features typically consist of hundreds of pixels. This is because any feature smaller than 4 square arcseconds (exactly 100 pixels) will remain undetected during automatic detection (Froebrich et al., 2015). Therefore a single pixel along a feature boundary carries a small weighting relative to a whole feature and won't affect the flux. It can also be argued that pixels on the right of the feature with a high probability of being excluded will be balanced by the pixels on the left with a high probability of being included. The co-ordinates of pixels that are deemed to be inside of the feature are stored in a text file.

Defining the Background

To determine the pixels that constitute the background, a circle which can just contain the entire area of emission for the feature is created. This is achieved by finding the greatest linear distance between a co-ordinate pair and the centre of the feature and designating that as the radius of the circle. It is found by testing every vertex co-ordinate pair through:

$$R_i = \sqrt{(x_i - C_x)^2 + (y_i - C_y)^2} \tag{3.4}$$

This will uncover the largest value of R_i which becomes synonymous with the radius, R, of the circle (and the feature). $R = R_i^{max}$. The background consists of all pixels contained within a ring with inner radius equal to R and outer radius $2R$. In a similar method as before, a box is created around the background ring. Each pixel inside the box is analysed and only deemed part of the background if its

44
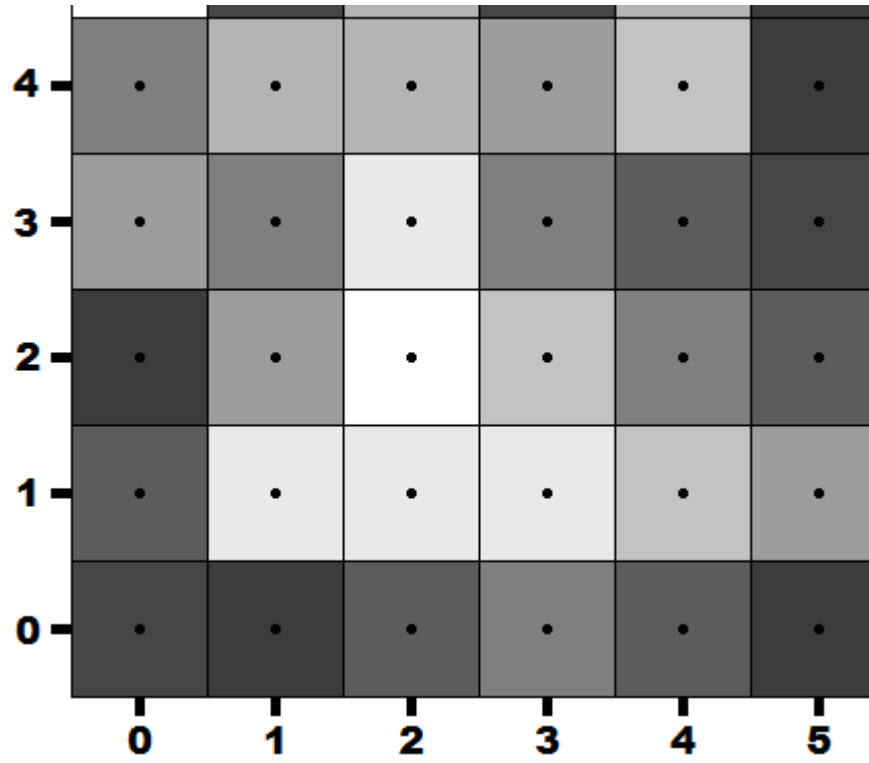
Figure 3.2: An example x, y grid of pixels. The integer co-ordinates of each pixel lies in its centre. As the photometry program includes pixels which have their upper right corner inside the feature, I specifically search whether $(x + 0.5, y + 0.5)$ for each pixel is in the feature or not.

distance from the circle centre (centre of the feature) is within the greater than R but less than $2R$. For features near the image boundary, some background pixels might have an intensity of 'NaN'. These pixels are ignored by the program. The co-ordinates of pixels that are deemed to be part of the background are stored in a text file.

The Mean, Median and Peak Pixel Intensities

There now exists two lists of pixel co-ordinates in text files, one with pixels that are inside the feature and the other with pixels inside the background ring. The program proceeds to open the relevant FITS image and, using the two generated lists of co-ordinates, grabs the respective pixel intensities and assigns the value to its co-ordinates. The value of pixel intensities in a feature can be described as counts and I calculate the mean, median and peak counts for each feature, as well as the sum of all counts within each feature. My program performs 3σ clipping to the background pixels in an attempt to remove extended H_2 sources or saturated stars which can lead to erroneous or negative background corrected fluxes. The background median surface brightness is then calculated and subtracted from the median surface brightness value of the feature to produce a corrected version. The processes described were performed for every feature in an image before every image in the survey. The photometry code can be found in Appendix A. Once this was completed for all H_2 features in all images, the flux was calibrated as described in the next section.

3.3 Flux Measurement and Calibration

The mean, median and peak counts for a feature (before or after correction) quantify the H_2 flux as the H_2 – K difference images conserve it. From this point, multiplying the counts for features in a single image by a calibration constant unique to that image will turn them into a meaningful flux with units W/m^2. In

order to convert the counts into a relevant units for flux we first converted them into magnitudes via:

$$m = m_{zp} - 0.05 \, (X - 1) - 2.5 \cdot log_{10} \left(\frac{counts}{t_{exp}} \right) - m_{ap} \qquad (3.5)$$

where M_{zp} is the magnitude zero point for the observations, X is the airmass during the observations, t_{exp} is the exposure time and m_{ap} is the aperture correction. The value of the airmass can only be within one or two meaning it will often have the same or smaller order of magnitude as the uncertainty of the magnitude zero point (Froebrich et al., 2015). The exposure time for our images is 720 seconds (Froebrich et al., 2011) and the aperture correction is zero as we only consider extended H_2 sources. The magnitude zero point can be found in the FITS header of a features respective image. Using the magnitude conversion, the flux can be obtained using:

$$f = F_0^{H_2} \cdot 10^{-\frac{m}{2.5}} \qquad (3.6)$$

where $F_0^{H_2}$ is the flux zero-point. We used the 2MASS K-band flux zero point from (Cohen et al., 2003) given as $4.283 \times 10^{-10} \, Wm^{-2}\mu m^{-1}$ and the K-band filter width of $0.262\mu m$ to arrive at a flux zero-point of $1.12 \times 10^{-10}Wm^{-2}$. With the substitution of the magnitude and flux zero-point we can conclusively describe the flux, f, of a feature as:

$$f = counts \cdot \frac{9.0 \times 10^{-12} \, Wm^{-2}}{t_{exp}} \cdot 10^{-\frac{m_{zp} - 0.05 \, (X-1)}{2.5}} \qquad (3.7)$$

Conversion of flux into surface brightness ($Wm^{-2} \, arcsec^{-2}$) should take into account that the area of one pixel is 0.04 square arcseconds (Froebrich et al., 2015).

3.4 Program Output

A table containing a small fraction of the output can be found in Table B.1 in Appendix B. The following feature properties have been found using my program and are available to view in the full catalogue online[1]:

i) Area of the emission in square arcseconds. The number of pixels inside the feature were counted and multiplied by the 0.04 square arcseconds area per pixel.

ii) Feature radius in arcseconds. This is the radius of a circle that can encapsulate the entire feature and is found using the centroid co-ordinates as previously described.

iii) Median background corrected surface brightness in $10^{-19} \, Wm^{-2} \, arcsec^{-2}$. It forms a reliable method of photometry when multiplied by the feature area as it will filter features with erroneous fluxes due to residual stars that influence the total flux. This is discussed in Chapter 6.

iv) Peak surface brightness in $10^{-19} \, Wm^{-2} \, arcsec^{-2}$: is the highest one-pixel surface brightness in the feature.

v) Total flux in $10^{-19} \, Wm^{-2}$: is the sum of all pixel intensities in the feature and a form of photometry that is effective if there are no residual stars in the feature.

vi) 1-pixel RMS noise surface brightness in $10^{-19} \, Wm^{-2} \, arcsec^{-2}$: is the one σ RMS of the pixel values in background ring after sigma clipping to remove bright or dark aberrations.

---

[1]astro.kent.ac.uk/uwish/catalogue

Chapter 4

Analysis of Individual H$_2$ Features

This chapter will discuss the characteristics of individual features in the UWISH2 survey. It will look to compare the spatial distributions of the extended H$_2$ emission features per square degree in the GP, Cygnus and Auriga as well the the flux and area distributions in the same regions. I discuss how relative survey coverage affects our results.

4.1   General Distributions

The total number of images that make up the survey is 5872. Of these, only 1929 images contain identifiable extended H$_2$ emission line features that are above the detection threshold which shows that a large fraction of the GP covered by the survey is vacant of H$_2$ emission. This would suggest many individual features either exist as a cluster and are localized to within a few arcminutes or that many features comprise one actual object. We have identified 33200 individual extended H$_2$ emission features within our images. I have compared how features belonging to the different classes (jets, PNe, SNRs and PDRs) are distributed throughout different sections of the GP as well as Cygnus and Auriga. Additionally I list the total area occupied by the features and their total flux. A summary of our results can be seen in Table 4.1 and Table 4.2.

Population Distribution

From information in Table 4.1, 62.1% of features exist within the GP, a region concerning $0° < l < 68°$ and $356° < l < 360°$. The latter Galactic longitude range shall henceforth be simplified to $-4° < l < 0°$ resulting in the GP spanning $-4° < l < 68°$ for the rest of this thesis. Because the GP covers a relatively large area, I have split it into four sections with each possessing a Galactic longitude range of $18°$. Section one henceforth refers to the region with the Galactic longitude range covering $-4° < l < 14°$, which includes the Galactic Centre. Section two henceforth refers to $14° < l < 32°$ whilst section three covers $32° < l < 50°$. Section four, finally, refers to the range $50° < l < 68°$. Breaking the 62.1% of features in their relevant sections, the three sections that make up $-4° < l < 50°$ possess an approximately equal share of H_2 features. Section one contains 27.6% of all features in the GP. Section two contains 33.7% whilst the section three contains 29.1%. This leaves section four with a much less significant contribution to the GP with 9.6% of features.

About 35.5% of features exist in Cygnus, which ranged from $74° < l < 86°$, whilst the remaining 2.4% of features can be found in Auriga, between $140° < l < 155°$.

The coverage of the survey is not entirely homogeneous meaning some sections of the GP have a greater width in Galactic latitude than others. The consequences of this is that comparing the number of features in a region won't yield an accurate conclusion. This is due to, for example, Galactic longitudes with a high feature population possibly having also received a greater amount of Galactic latitude coverage than Galactic longitudes with less features. In an attempt to correct this ambivalence, Table 4.2 lists the average number of features occupying one square degree per specific position (GP, Cygnus, Auriga). From this, 73% of our survey coverage is spent observing the GP. Breaking down the 73% across the four defined sections of the GP, section one received 21% of the relative coverage. Sections two, three and four received relative coverages of 27.5%, 28.1% and 23.3% respectively. This shows that sections two and three received the most coverage in the GP.
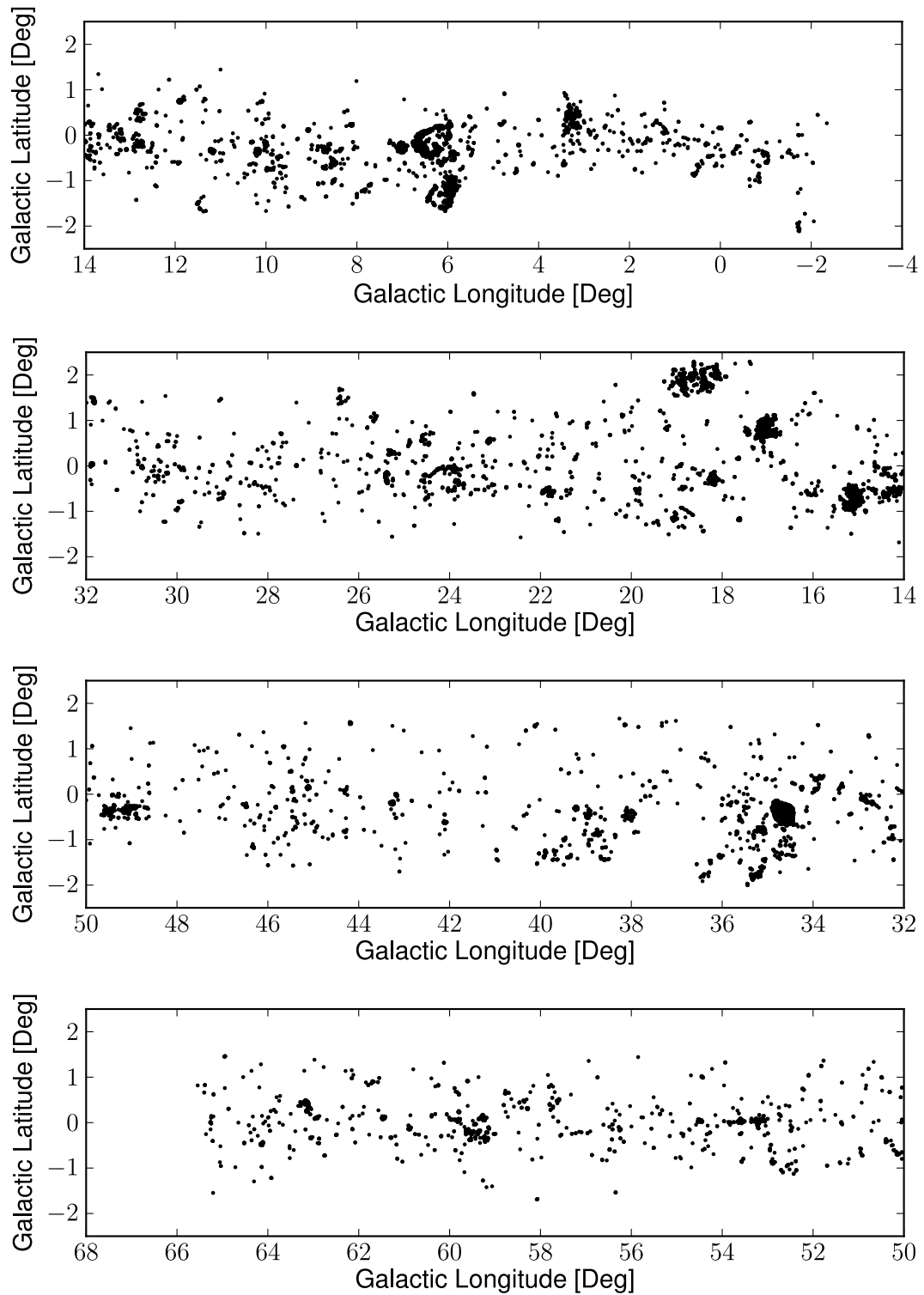
Figure 4.1: The spatial distributions of all H_2 features within the four defined sections of the GP. It accurately depicts the non-homogeneous distribution.
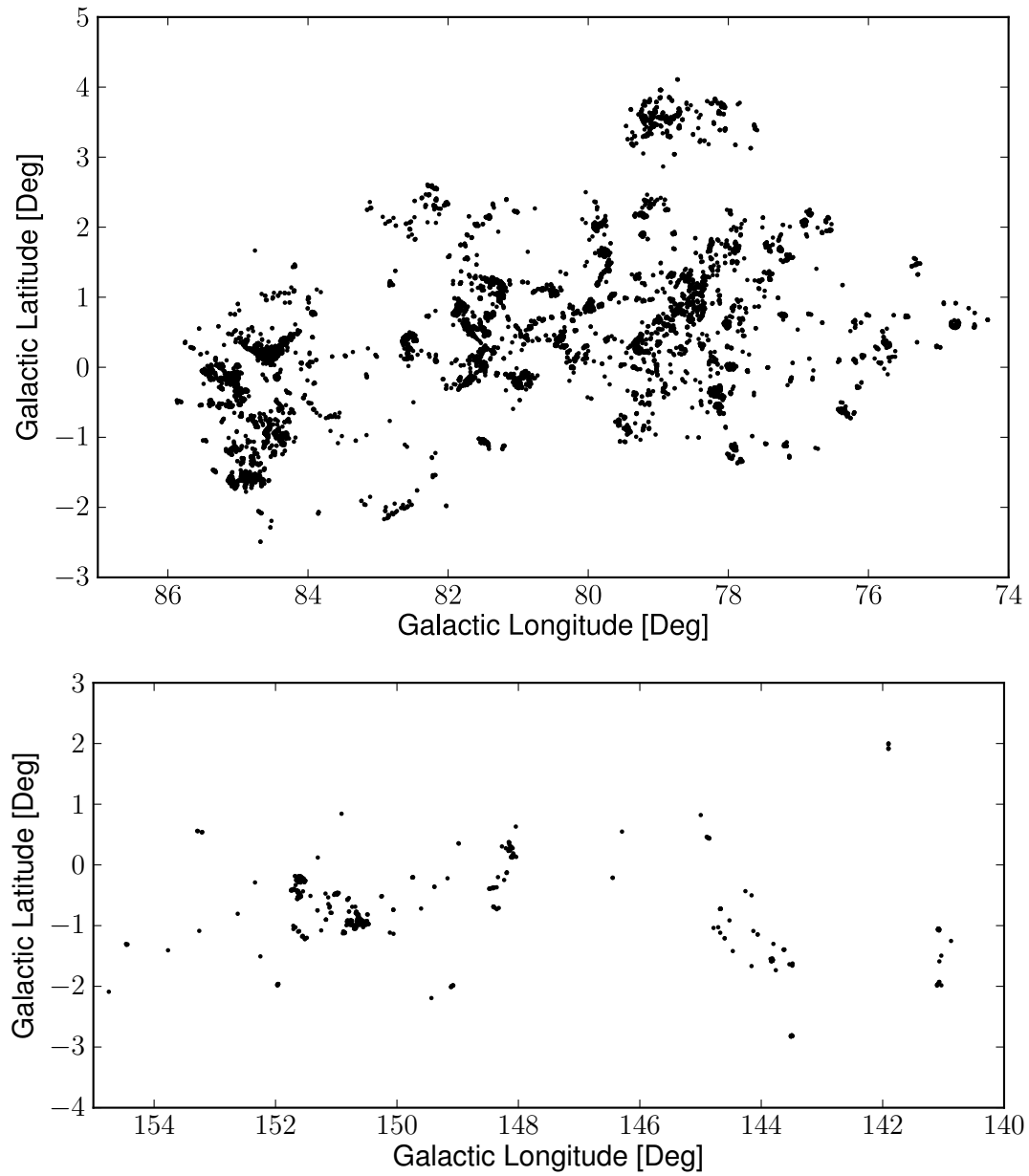
Figure 4.2: The spatial distributions of all features within Cygnus (top) and Auriga (bottom). The larger range of Galactic latitudes shows survey bias as we targeted regions of high column density.

52

Comparisons of the number of features per square degree given in the table now contradict comparisons of feature numbers in Table 4.1. It appeared before that sections two and three had the highest number of features but after scaling for the survey coverage, section one was in fact the most crowded with 129.6 H_2 features per square degree. An initially small decline to 121.1 H_2 features in the section two grew into a large decline of 101.9 H_2 features in section three and 40.5 H_2 features in section four.

H_2 features classified as jets or PDRs can be used as tracers to identify star formation regions. The presence of jets can be synonymous with active accreting YSOs and T-Tauri Stars. PDRs serve as tracers for more evolved and higher mass stars and are often found near clusters. Coupling this with the fact that section one contained the highest number of jet features per square degree (11.64), the star formation activity is highest at lower Galactic longitudes and toward the Galactic Centre. Section four features are comprised of 21.4% jets/outflows which is a relatively high percentage. This is due to the lack of SNR and PDR features which is evidence for a deficit of high mass stars in this section.

There is a deficit of PNe features in section one compared to sections two and three. This may be due to a combination of extinction and distance, which would be complimentary to each other in this case. The lower Galactic longitudes (i.e section one) are directed toward the Galactic Centre, looking into the nearby Sagittarius arm of The Milky Way. As a minor spiral arm of The Galaxy, it is essentially a giant star forming factory full of bright young stars and dense gas. Thus it is entirely plausible that the extra extinction in this direction prevents the detection of some PNe in section one.

Out of approximately 300 known SNRs in the Milky Way (Green, 2014), the UWISH2 survey covers 119 members either partially or fully. From these 119, we have manually identified H_2 emission features likely belonging to 30 of them.

Therefore our SNR detection rate is roughly 25%. Of the 119 covered, seven belong to Cygnus and one inhabits Auriga, and these are listed in Table 4.3. The reason that there are no H_2 emission features classed as SNRs in Cygnus and Auriga is likely statistical. With the SNR detection rate there was a 13% chance that none of the Cygnus SNRs would be detected. For Auriga, there was a 75% chance that its sole SNR would remain undetected. It could also be that Auriga being of relatively low mass compared to Cygnus and the GP is unlikely to produce numerous high mass stars that are capable of going supernova.

Table 4.1: Table showing the sum of feature areas and the sum of feature total fluxes for the different types of emission source in different regions of the survey. The first five columns of data, denoted by N, list the various populations of H_2 features. The first column is the total number of features of all types in different regions in the survey before being broken down into the various types. The three main sections we say objects can be located in are the GP, Cygnus and Auriga. Due to its large size, the GP is further split into four sub-sections of equal sized sections. Section one covers $-4° < l < 14°$. Section two covers $14° < l < 32°$. Section three covers $32° < l < 50°$ whilst section four covers $50° < l < 68°$. The sixth through to tenth columns list the sum of feature areas, denoted by A^{tot}, for different types and region. The final five columns list the sum of the feature total flux, denoted by F^{tot}, of the features split into the same criteria as before.

Region In Plane	N_{All}	N_{Jet}	N_{PN}	N_{SNR}	N_{PDR}	A^{tot}_{All}	A^{tot}_{Jet}	A^{tot}_{PN}	A^{tot}_{SNR}	A^{tot}_{PDR}	F^{tot}_{All}	F^{tot}_{Jet}	F^{tot}_{PN}	F^{tot}_{SNR}	F^{tot}_{PDR}
						[arcmin^2]					[$10^{-14}\,\mathrm{W\,m^{-2}}$]				
Whole Survey	33200	3558	796	5630	23216	407.2	31.9	17.0	117.3	241.0	113.97	10.55	7.67	46.10	49.65
GP	20627	1895	726	5630	12376	292.3	15.6	15.6	117.3	143.8	88.41	4.70	7.37	46.10	30.25
— Section One	5698	512	117	1720	3349	107.1	5.2	3.9	38.7	59.3	32.84	1.69	1.87	14.39	14.89
— Section Two	6958	492	224	512	5730	68.9	3.7	5.0	6.6	53.6	17.71	1.16	3.98	2.64	9.94
— Section Three	5996	468	250	3337	1941	96.6	3.8	4.5	71.5	16.7	34.15	1.15	1.13	29.01	2.87
— Section Four	1975	423	135	61	1356	19.8	2.9	2.2	0.5	14.2	3.71	0.69	0.40	0.06	2.56
Cygnus	11790	1476	39	—	10275	108.3	15.4	1.0	—	91.9	24.25	5.73	0.24	—	18.27
Auriga	783	187	31	—	565	6.5	0.9	0.4	—	5.3	1.30	0.12	0.06	—	1.13

Table 4.2: Table showing the number of H_2 features, N and total flux, F, per square degree using the survey coverage for the GP, Cygnus and Auriga. Due to its large size, the GP is further split into four sub-sections of equal sized sections. Section one covers $-4° < l < 14°$. Section two covers $14° < l < 32°$. Section three covers $32° < l < 50°$ whilst section four covers $50° < l < 68°$.

Region In Plane	Survey Coverage	N_{All}	N_{Jet}	N_{PN}	N_{SNR}	N_{PDR}	F_{All}	F_{Jet}	F_{PN}	F_{SNR}	F_{PDR}
	[deg^2]			[features per deg^{-2}]					[$10^{-14}\,\mathrm{W\,m^{-2}\,deg^{-2}}$]		
Whole Survey	286.45	115.90	12.42	2.78	19.65	81.05	0.40	0.04	0.03	0.16	0.17
GP	209.01	98.69	9.07	3.47	26.94	59.20	0.42	0.02	0.04	0.22	0.14
— Section One	43.97	129.59	11.64	2.66	39.11	76.17	0.75	0.04	0.04	0.33	0.34
— Section Two	57.40	121.22	8.57	3.90	8.92	99.83	0.31	0.02	0.07	0.04	0.17
— Section Three	58.83	101.92	7.96	4.25	56.72	33.0	0.58	0.02	0.02	0.49	0.05
— Section Four	48.71	40.55	8.68	2.77	1.25	27.84	0.08	0.01	0.008	0.001	0.05
Cygnus	41.99	280.78	35.15	0.93	—	244.70	0.58	0.14	0.006	—	0.44
Auriga	35.46	22.08	5.27	0.87	—	15.93	0.04	0.003	0.001	—	0.03

Area Distribution

The sum area of all the extended H_2 features in our survey is 407.2 square arcminutes or approximately 0.11 square degrees meaning detectable H_2 only occupies one two-thousand-five-hundredths of the total coverage of the survey. Of the 407.2 square arcminutes, features in the GP contribute 71.8% of the area and for Cygnus, 26.6%. This leaves the final 1.6% from Auriga.

To get an idea of relative sizes, the total jet and PNe feature areas in the GP are of similar quantity. Jet features, however, feature much more in number than PNe features meaning that the average area of extended H_2 emission from a jet feature will less than that of an average PN feature.

Cygnus has nearly more than four times the jet features per square degree and almost equals the total jet area of the entire GP. I have already mentioned that the presence of jets is tracer of star formation indicating that Cygnus has a huge amount of active star formation. The most populous contributors to our catalogue of features also represent the highest fraction of areas in our cumulative values. The PDR features make up 70% of the catalogue so it is not surprising they comprise 59.2% of the total area. Almost half of the PDR area is contained within the first two sections of the GP. There is also a significant contribution in Cygnus. PDRs, which are tracers for higher mass stars and star forming regions as previously mentioned, are known to be in abundance in the GP and Cygnus. Figure 4.3 shows the area distribution of the features for jets (top row) and PDRs (bottom row). The left-hand column shows distribution of said classes across the GP whilst the right-hand column shows the distribution for Cygnus. For the GP, it shows that there is more emission at Galactic longitudes lower than 20° than seen at higher Galactic longitudes. We observe a steady decrease in area as Galactic longitude increases. Large groups can contribute to huge spikes of area, such as at $35° < l < 36°$ for jets. The spike in area is partly due to Mercer 14, a young molecular cloud with a YSO producing the massive outflow G35.2-0.74N. Another example is DR 21, a huge star forming region in Cygnus at $81.5° < l < 81.75°$. For Cygnus there is no obvious relationship with Galactic longitude and the total area of H_2 emission.

Table 4.3: Table of known SNRs within the survey coverage of Cygnus and Auriga that show no H_2 emission. Information is taken from (Green, 2014), which includes an SNR's position in Galactic co-ordinates (listed to one-tenth of a degree). Listed is also the angular size of the remnants in arcminutes. If a remnant has a given name in other literature, the name has been supplied. The '?' notation adjacent to any data entry implies inaccuracy and hence lack of confidence for a definitive value or category.

Region	Galactic longitude [deg]	Galactic latitude [deg]	Size [arcmin]	Other name
Cygnus	74.9	1.2	8×6	CTB 87
Cygnus	76.9	1.0	9	–
Cygnus	78.2	2.1	60	DR 4, γ Cygni SNR
Cygnus	83.0	-0.3	9×7	–
Cygnus	84.2	-0.8	20×16	–
Cygnus	85.4	0.7	24?	–
Cygnus	85.9	-0.6	24	–
Auriga	152.4	-2.1	100×95	–
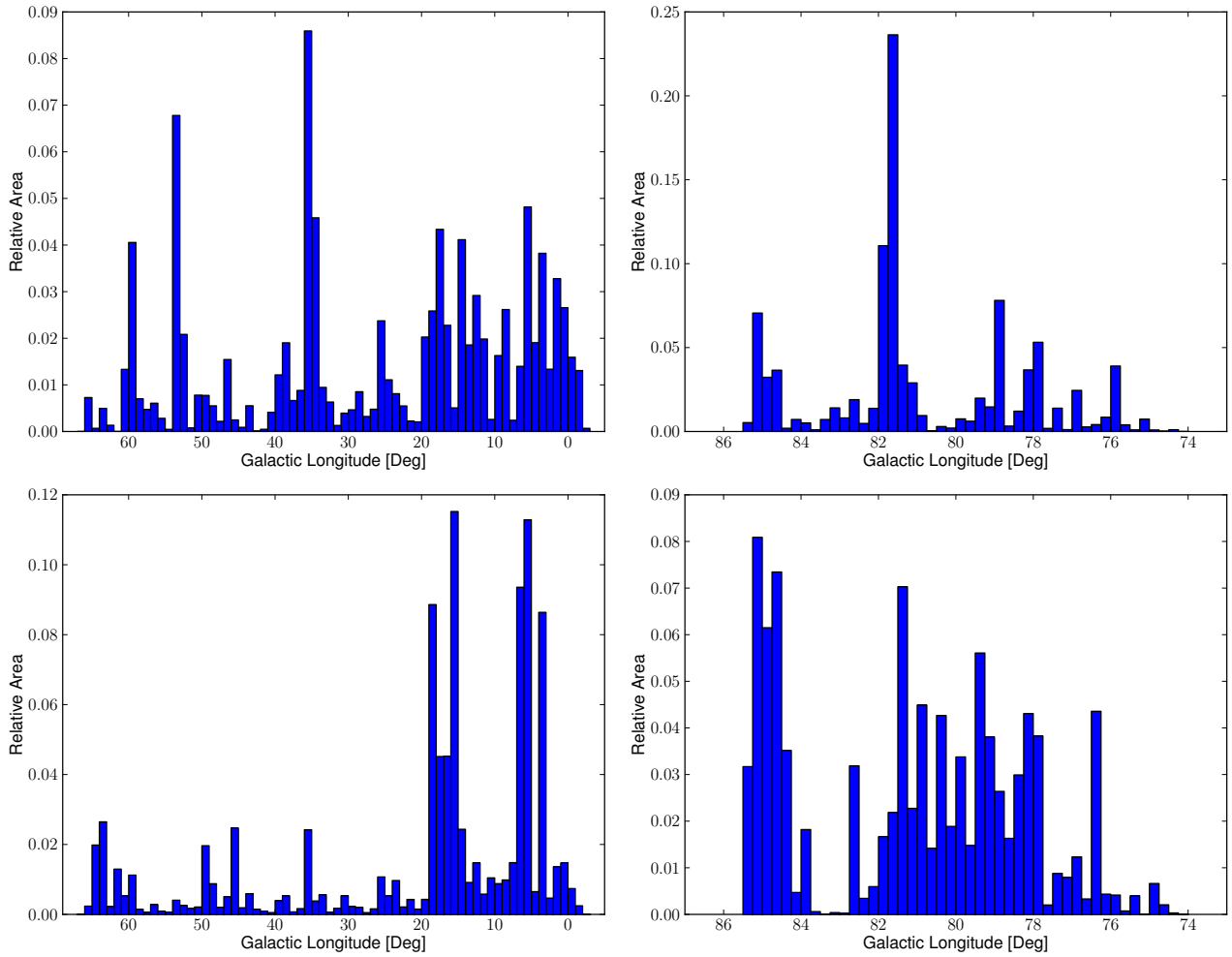
Figure 4.3: The distribution for the feature emission area across the Galactic longitude in the GP (left) and Cygnus (right) for jets (top) and PDRs (bottom). Bin width for the GP is one degree and 0.25 degrees for Cygnus.

Because the majority of H_2 features exist in groups and actual regions of emission take up minuscule areas relative to the area of the entire survey, it is realistic that a one degree longitude range may contain very little emission. Because jet/outflow features contribute a large fraction of area in the higher Galactic longitudes of the GP and PDRs do not, it suggests that the abundance of higher mass stars may be contained at the lower Galactic longitudes.

Total Flux Distribution

The sum total flux of all H_2 features in all areas of coverage for the survey is $1.14 \times 10^{-12}\,W\,m^{-2}$ meaning the average flux across all features is $3.43 \times 10^{-17}\,W\,m^{-2}$. PDR and SNRs features make up 43.6% and 40.4% of the total flux in the survey respectively. They also make up 86.9% of all the survey features and 88% of the total emission area so the huge contribution isn't unexpected. The jet feature flux per square degree of Cygnus is 6.08 times that of the entire GP and almost 40 times greater than that of Auriga. For jet and PDR features, areas of high total flux are a good indicator of active star formation. We can conclude that whilst areas of high column density were targeted in Auriga, data suggests it is a very sparse region relative to other regions in the survey.

The PDR feature flux density in Cygnus is almost three times that of the GP. There is however 1.35 times more PDR feature flux contained in the first two GP sections than the entirety of Cygnus. This suggests that whilst higher mass star formation activity is high in both regions, the lower Galactic longitudes of the GP are home to a larger number of high mass stars, which complements the findings from the Section The distance to features will also have an effect on the total flux however, as the area and total flux will decrease with distance. It may be possible that the majority of bright PDRs (and other features) in the GP may be very close compared to PDRs in Cygnus. These numbers are represented as a flux distribution in Figure 4.4. The top row relates to total flux of jets in the GP and Cygnus respectively. For jet features, whilst there is no discernible pattern, a large fraction of total flux is contained within the first 20° from the Galactic Centre. A few regions at higher Galactic longitudes can also contain large amounts of flux. One such region between $53° < l < 54°$ contains the infrared dark cloud (IRDC) G53.2 which is analysed in Kim et al. (2015). In Cygnus there is no visible relationship, the total flux appears independent of spatial location. As with the GP, there are some large spikes from regions such as DR 21. The panels along the bottom row of Figure 4.4 replace jet features with PDR features and a similar relationship is seen at the Galactic Centre. High amounts of jet flux can be found at the higher Galactic longitudes of
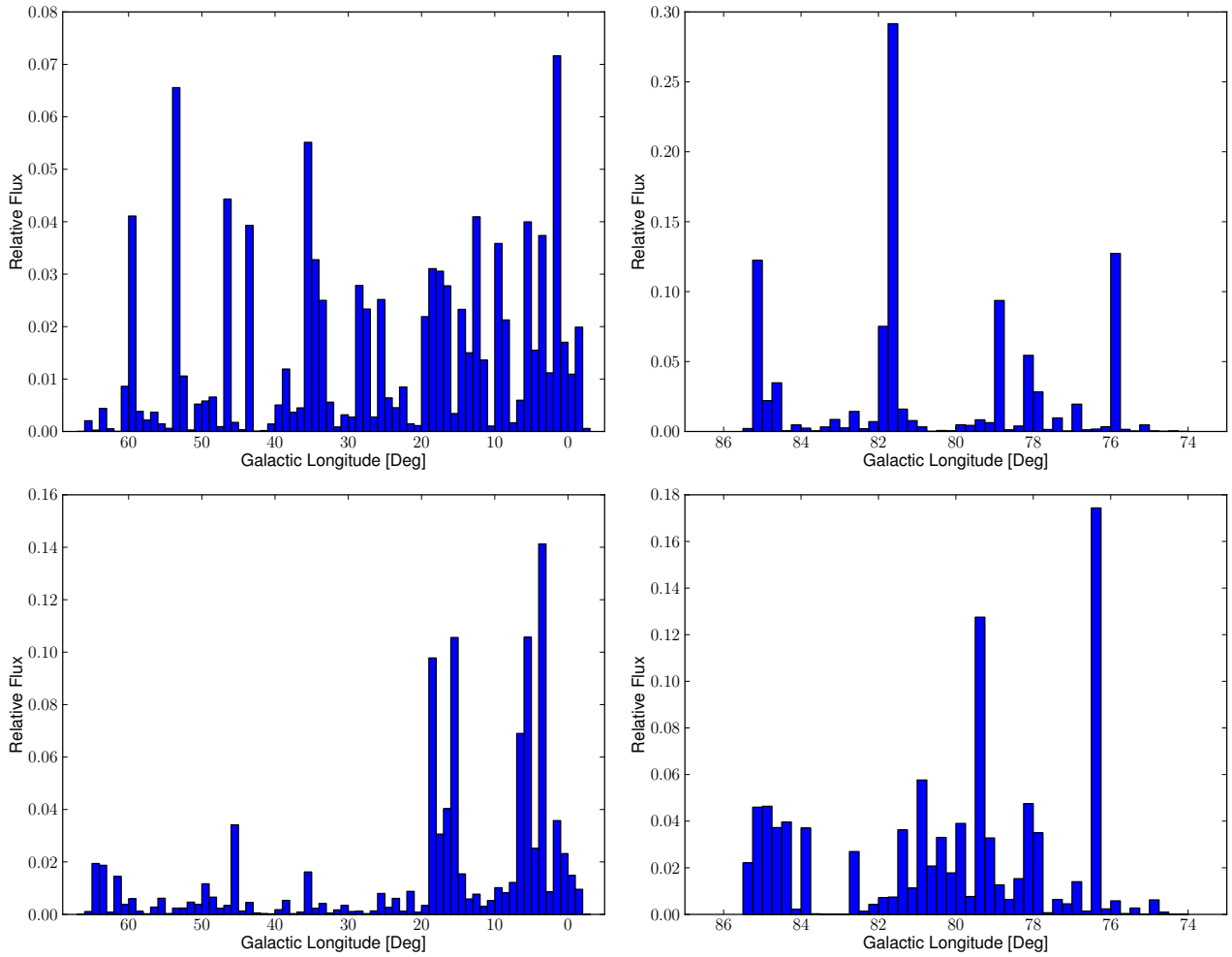
Figure 4.4: The distribution for the total flux across the Galactic longitude in the GP (left) and Cygnus (right) for jets (top) and PDRs (bottom). Bin width for the GP is one degree and 0.25 degrees for Cygnus.

the GP whilst high PDR flux can not be. For Cygnus, there is a relatively small amount of change in flux as Galactic longitude changes. There are two spikes of high flux caused by features within $76.25° < l < 76.5°$ and $79.25° < l < 79.5°$. The former is mostly due to a large HII region at G076.4-00.6 whilst the latter is made of several intermediately bright objects, with the highest flux coming from a HII region at G079.3+00.3.

61

The projected numbers of jet/outflow features in Figure 4.5 at given Galactic longitudes and latitudes is derived from the known coverage of the survey. We were able to calculate the expected number of jet features seen at any given Galactic longitude or latitude and compare to the actual number detected. The coverage distribution is mostly uniform-like such that if the projected data were to match closely with real data, then we would expect a homogeneous distribution of jet features over a ~ 200 squared degree region covering $-3° < l < 67°$ and $-1.4° < b < 1.4°$. This is not the case as we have identified a greater jet density than projected near the Galactic Centre where several lower Galactic longitudes have a higher number of features than projected. The opposite of this observation is usually true at higher Galactic longitudes. We can visualize the decrease in jets (and hence star formation) as Galactic longitude increases and the actual number of features is less than projected. This is also observed with the distribution for the Galactic latitude in that the greatest number of jet features occurs between $0° \leq b < 0.1°$ before decreasing away from the Galactic Centre in both directions. There is a higher split of jet features observed in the southern hemisphere of the Milky Way. Similar figures for PNe, SNR and PDR features can be found in Appendix F.1.
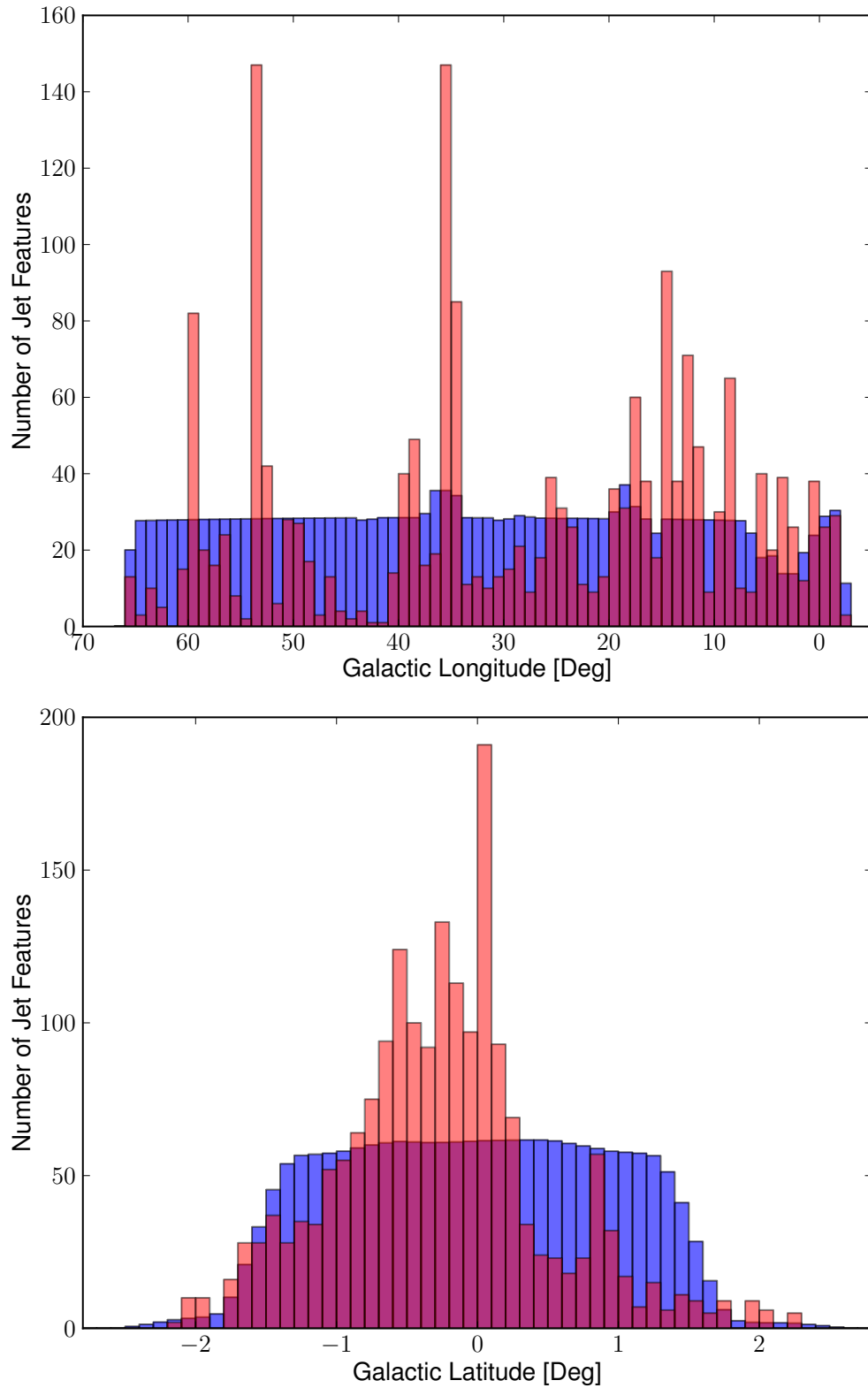
Figure 4.5: The distribution of jet features in the GP found per one degree Galactic longitude (top) and 0.1 degrees Galactic latitude (bottom) versus the projected distribution using the relative survey coverage at each region (blue).

Chapter 5

Analysis of Groups of H$_2$ Features

In this section I will discuss the process of grouping the individual H$_2$ features into jet and PDR groups, and whole or partial PNe and SNRs. I compare the number of groups of jets and PDRs and the number of PNe to the expected numbers from the survey coverage. I also briefly discuss the new PNe candidates we have observed.

5.1 Grouping of features

As previously discussed, the majority of H$_2$ features are in fact not isolated and instead form part of a larger complex. As a result of their large size and low surface brightness, objects such as PNe and SNRs will be composed of several emission features. For the majority of individual features, apart from those classed as SNRs, the features were grouped according to their spatial distribution (Froebrich et al., 2015). Features were considered part of a group if they had a nearest neighbour within a specific angular distance unique to the feature classification. For each group, the position of the object/group centre, the total flux, total area, total median surface brightness were all calculated from the sum of the composing individual features. Additionally, the group size was calculated which is the radius of a circle enclosing all features for a given object or group.

As mentioned above, the threshold for a feature to be considered for group or object membership is dependent on the types of emission. For PNe, features were

64

automatically grouped if they had a separation of less than three arcminutes. A PNe group can generally be considered as a single PNe but manual confirmation was carried out to ensure that no two PNe were closer than the three arcminute threshold. We also checked that the extended PNe in the catalogue had no outlying features beyond the threshold that were incorrectly classified as a separate PN. Concerning the jets and outflows, there have been issues with identifying identifying the actual driving source of some jets. Separating jets and outflows and identifying their source is a task which is beyond the scope of this thesis. Efforts to achieve this are ongoing (Makin and Froebrich, in prep; Froebrich and Makin, in prep) and this subject is further discussed in Chapter 8. Even without the knowledge to confidently identify an individual source and the outflows emanating from it, we can still conclude that a group of jets/outflow features can be considered as a star forming region with several actively accreting YSOs. Thus we are still able to analyse jet groups for useful information on star forming regions. From (Ioannidis and Froebrich, 2012b) the typical line-of-sight distance of jets and outflows in the survey area is about $3.5 \, \mathrm{kpc}$ and groups are generally of the order of $5 \, \mathrm{pc}$ (small) in size (Ioannidis and Froebrich, 2012a). As a result of this we used a separation threshold of $0.1°$ for the minimum distance in grouping (six arcminutes). Figure 5.1 elaborates on how features are grouped and how the $0.1°$ minimum distance comes into play. In this example, the feature labelled 'start' is our origin point. From this, a program identifies the nearest neighbour and determines whether its centroid is within $0.1°$ from the origin feature. If true, the two features are grouped and if false, the 'start' feature becomes a group with itself as the only member. Assuming the nearest neighbour was grouped, the program identifies the second nearest neighbour from the origin. The criteria is then slightly altered and the program asks if the distance to the second nearest neighbour minus the distance to the first nearest neighbour is less than $0.1°$. If true then it is grouped and the program continues to the next nearest neighbour until the difference between a feature and origin and the closest feature before it and the origin is greater than $0.1°$. The features classified as unknown or 'u' (which are likely Hɪɪ regions or PDRs) are
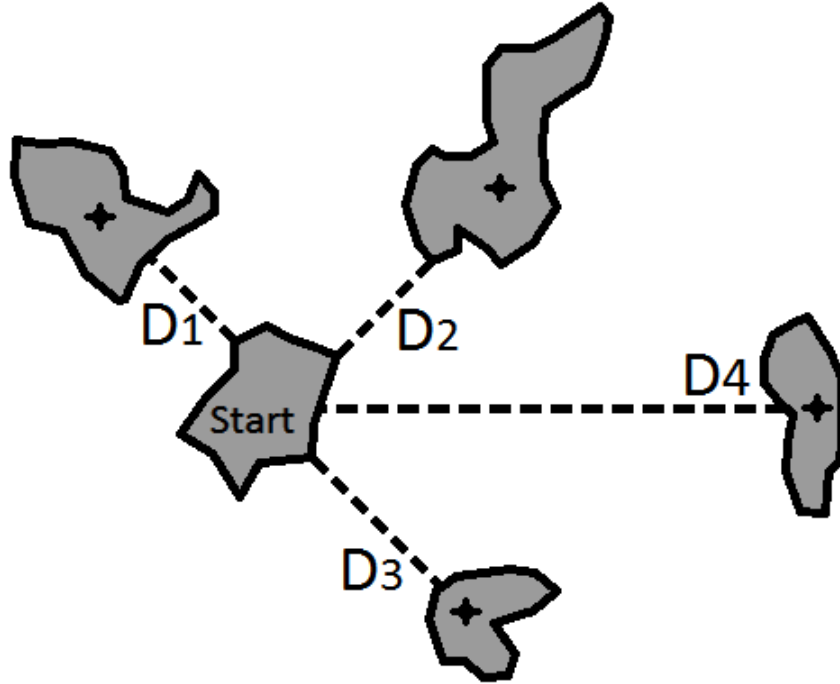
Figure 5.1: An example illustration of the feature grouping process. Distances are arbitrary but assume in this example that the distance 'D1' is less than 0.1°and the distance 'D4-D3' is greater than 0.1°to end the grouping process.

grouped using the same 0.1° minimum separation distance as the jets/outflows as they probably share similar typical distances with jets. These features are likely linked to more evolved star forming regions, which compliments the very young star forming regions responsible for jets. The H_2 emission from these features is caused by radiation from intermediate mass stars.

$$
\begin{aligned}
\text{Nearest Neighbour} \quad &: \quad D_1 < 0.1° \\
\text{Next Nearest Neighbour} \quad &: \quad D_2 - D_1 < 0.1° \\
\text{Next Nearest Neighbour} \quad &: \quad D_3 - D_2 < 0.1° \\
&\Downarrow \\
N^{th} \text{ Nearest Neighbour (not in group)} \quad &: \quad D_N - D_{N-1} > 0.1° \\
\end{aligned}
\tag{5.1}
$$

Program ends, group of N-1 features produced

There are some drawbacks to this method of grouping. The first drawback is that whilst the 0.1° minimum distance has been agreed upon with reason, it remains an arbitrary choice. We would expect a noticeable difference in the group numbers if the minimum distance agreed was different. Using jet and PDR grouping as an example, if the minimum distance was 0.09°, we would expect some of the groupings to have ended prematurely leading to a higher number of smaller groups. Alternatively, a minimum distance of 0.11° would increase the chance of a distant feature being grouped which might increase group sizes and may cause a group with one or a few members to cease to exist. The second drawback arises from the choice of the 'start' feature. Looking at Figure 5.1 and assuming it is not representative of any scale, if the distance 'D_1' is very close to 0° then the distance labelled 'D_2' must be very close to 0.1° for it to be grouped. Thus when we talk about number of jet and PDR groups where this method has been applied there is always uncertainty. Changing the minimum distance for grouping or the starting feature could allow the final numbers to vary by a small amount but my analysis will statistically lead to the same result even with the group numbers eligibility to change.

So far we have used a minimum separation distance to group jets, PNe and PDR features but features classified as SNRs are processed into groups differently. Since many of the SNRs are very extended it was possible to manually select, spatially identify and group all features into their known respective SNRs. Applying the grouping method described for jets and PDRs yielded 78 groups for the 30 confirmed SNRs with H_2 emission in our survey which highlights the advantages of visual identification. The group catalogues are available online[1].

---

[1]astro.kent.ac.uk/uwish/catalogue

5.2 Group Distributions

The entire survey contains 2334 groups across all types of H_2 feature, which averages at approximately 14 features per group. About 71.4% of groups lie within the GP. Concerning only the GP, and using the same criteria for GP sections as defined in Chapter 4, section one contains 24.7% of GP groups, section two holds 31.2%, section three holds 24.5% and then section four with 19.6% of groups. Cygnus holds 24.8% of groups whilst Auriga comprises 3.8%. A more detailed breakdown of the groups is presented in Tables 5.1 and 5.2. In these tables, we present the numbers of the various types of H_2 feature (jets, PNe, SNR and PDRs) as well as the number of these groups per square degree of coverage. The total flux and total area of any specific object/group class in a given area will be the same as those listed in Tables 4.1 and 4.2. To reiterate, PNe and SNR groups now refer to a single object whilst jet groups refer to young star forming regions and PDR groups refer to more evolved star forming regions in proximity to higher mass stars.

Table 5.1: Table showing the numbers of H_2 emission features in different parts of the survey that have been used for analysis. Columns indicate the different classes of emission and rows describe the different parts of the survey (GP, Cygnus and Auriga). Note that the top row concerns the entire survey, indifferent of any specific part. The 'GP' row precedes a split into four equal sections of Galactic longtiude defined as section one ($-4° < l < 14°$), section two ($14° < l < 32°$), section three ($32° < l < 50°$) and section four ($50° < l < 68°$). Note that numbers of PNe and SNRs refer to individual 'complete' objects and numbers of jets and PDRs refer to a group of objects with possibly indiscernible origins but constitute a star forming region.

Region in Survey	N_{Groups}^{Jet}	N^{PN}	N^{SNR}	N_{Groups}^{PDR}
	[number of]			
Whole Survey	711	284	30	1309
GP	450	261	30	925
— Section One	121	45	11	234
— Section Two	145	79	10	286
— Section Three	98	73	7	231
— Section Four	86	64	2	174
Cygnus	210	16	—	353
Auriga	51	7	—	31

Table 5.2: Table listing total coverage of the full or partial parts of the survey in square degrees followed by the projected density of groups per square degree for different classes and parts. Note that the top row concerns the entire survey, indifferent of any specific part. The 'GP' row precedes a split into four equal sections of Galactic longitude defined as section one ($-4° < l < 14°$), section two ($14° < l < 32°$), section three ($32° < l < 50°$) and section four ($50° < l < 68°$). Note that numbers of PNe and SNRs refer to individual 'complete' objects and numbers of jets and PDRs refer to a group of objects with possibly indiscernible origins but constitute a star forming region.

Region in Survey	Survey Area	N^{Jet}_{Groups}	N^{PN}	N^{SNR}	N^{PDR}_{Groups}
	[deg^2]	[groups deg^{-2}]			
Whole Survey	286.45	2.48	0.99	0.10	4.57
GP	209.01	2.15	1.25	0.14	4.42
— Section One	43.97	2.75	1.02	0.25	5.32
— Section Two	57.40	2.53	1.38	0.17	4.98
— Section Three	58.83	1.67	1.24	0.12	3.93
— Section Four	48.71	1.77	1.31	0.04	3.57
Cygnus	41.99	5.00	0.38	—	8.41
Auriga	35.46	1.44	0.20	—	0.87

Jets and Outflows and PDRs

Figure 5.2 shows the spatial distributions of all the jet and PDR groups. Jets and PDRs appear to be distributed in a way that doesn't agree with the homogeneity of the survey. This can be observed in greater detail in Figure 5.3 which compares the actual number of groups and the estimated number of groups at a given Galactic longitude or latitude from utilizing the coverage. The spatial distributions concerning the Galactic latitude of both jets and PDRs show agreement that in a largely homogeneous survey, the bulk of star formation can be seen occurring close to or around $-0.5° < b < 0.5°$. Beyond the latitude range described, the number of groups declines rapidly as distance from the GP increases in what resembles a Gaussian distribution. For the Galactic longitude, we can see that in both jets and PDRs, there is a higher concentration of groups for $l < 20°$ compared to both the actual number of groups when $l > 20°$ or when comparing to the projected number for $l < 20°$ from the coverage. Aside from minimal occasions where group concentration is huge, the coverage starts to overestimate the number of groups as Galactic longitude increases. This is good evidence for a large amount of star forming around the Galactic Centre.

When taking into account the coverage of the survey it is clear that Cygnus has the highest density of jet and PDR groups, with 5.00 jet groups and 8.41 PDR groups per square degree. The GP, by comparison, has 2.15 jet groups and 4.42 PDR groups per square degree (over 209 square degrees), significantly less than Cygnus. The GP, represented as four sections, shows that the density of groups is actually higher at low Galactic Longitudes and gradually decreases. The density of groups in Cygnus may likely have been affected by a survey bias in which we specifically targeted areas with high column density, such as known regions of active star formation. This was due to the lack of time remaining to complete the survey. However, when we look at the density of jet and PDR groups in the star forming region Auriga, a recipient of the same survey bias, the numbers were much smaller. Auriga yielded 1.44 and 0.87 jet and PDR groups per square degree respectively. This is expected given that the star formation rate and surface density

of the cloud is smaller in Auriga. It is clear that the number of groups (and group density) is affiliated to the number of H_2 features. This is shown in the outer GP (mainly section four) and Auriga which have the fewest features and fewest groups of star formation tracers (jets and PDRs). Therefore, even with the survey bias, we do not guarantee a yield of a large number of features because the star formation rate in Auriga is very low. The spatial distribution of jets and PDRs in Cygnus and Auriga is shown in Figure 5.4.
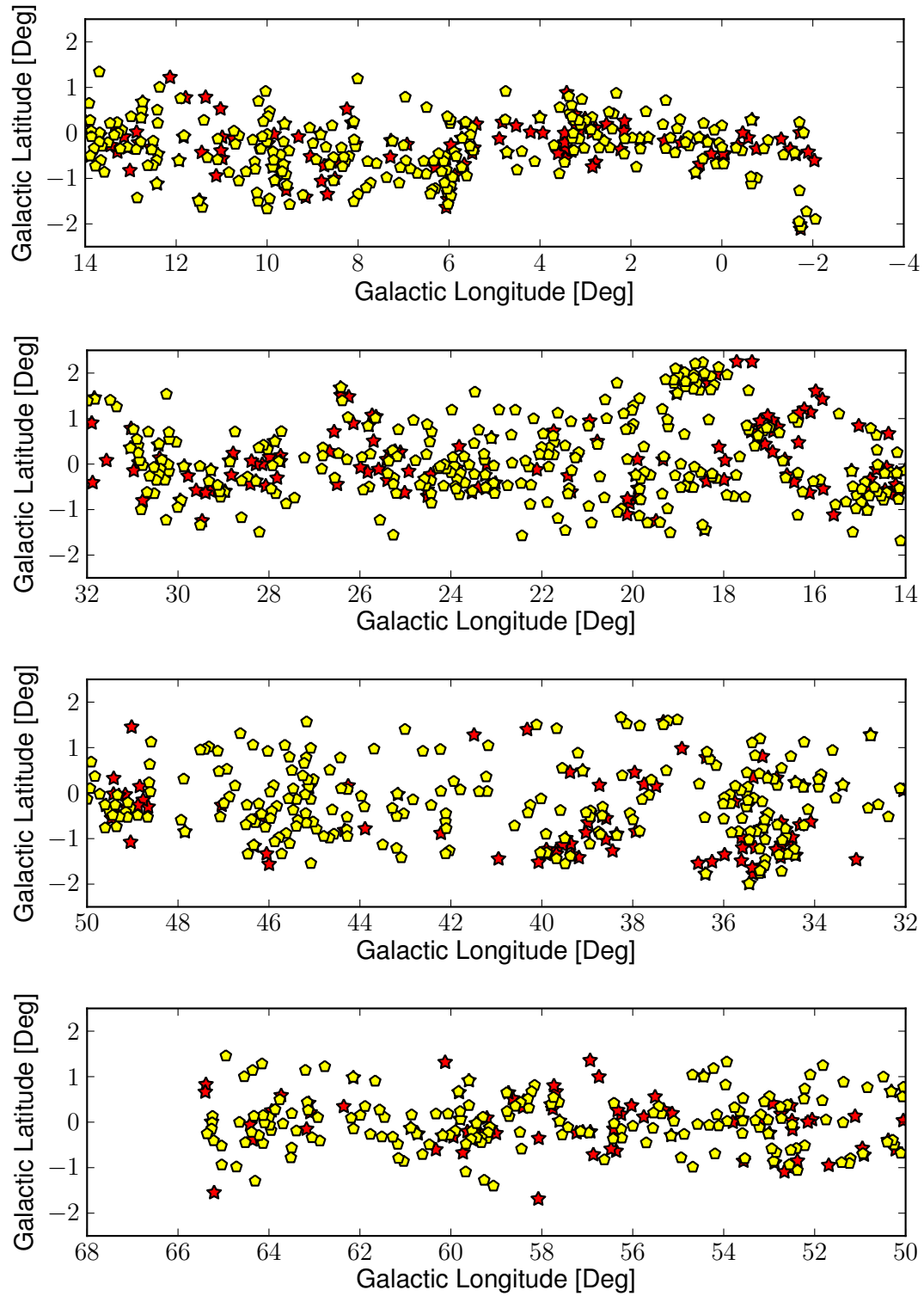
Figure 5.2: The spatial distributions of all the jet (stars) and PDR (pentagons) groups in the four sections of the GP. The top plot represents section one with sections two, three and four following in descending order.
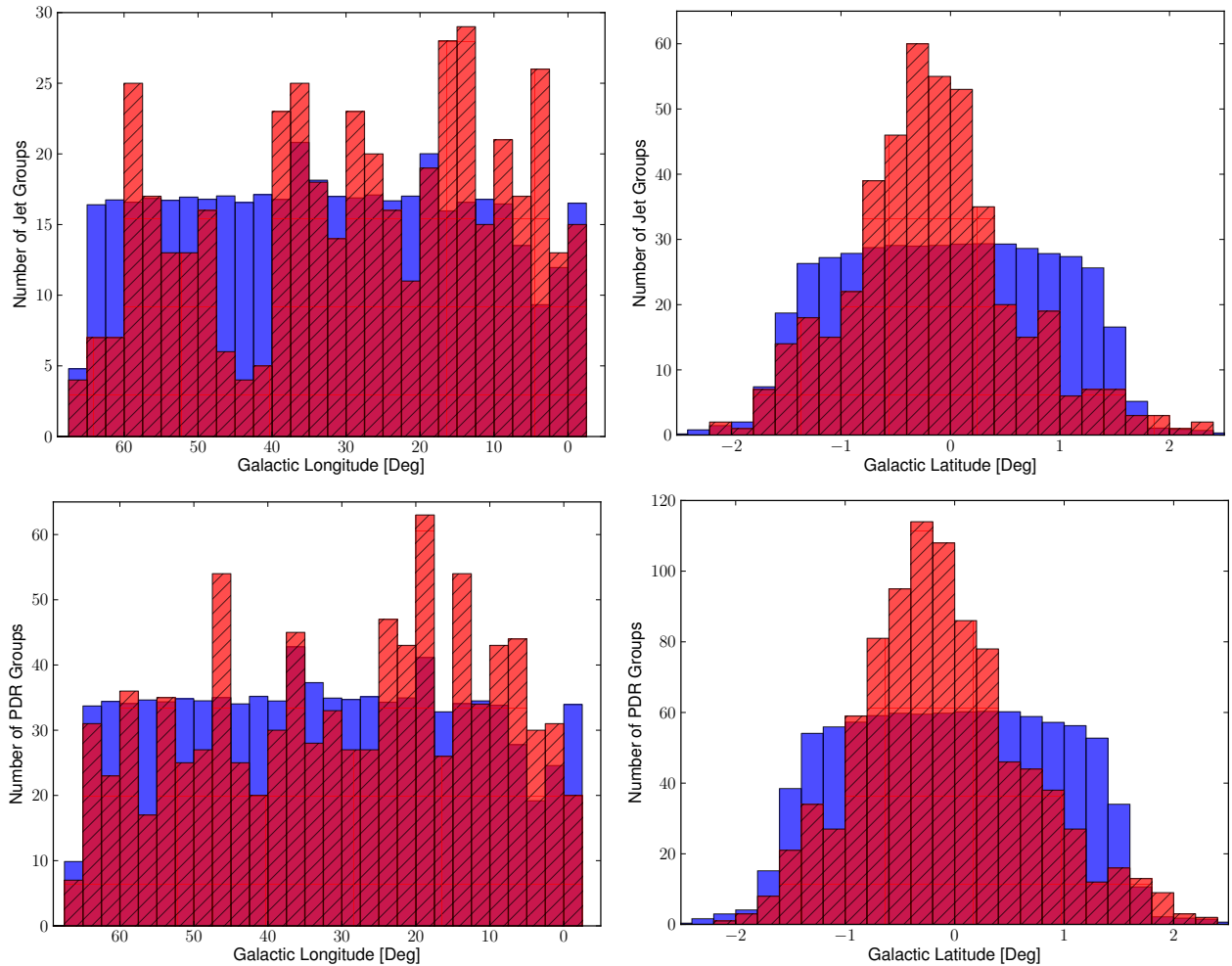
Figure 5.3: Plots of the distribution of jet (top row) and PDR (bottom row) groups along the GP found per 2.5 degrees Galactic longitude (left column) and 0.2 degrees Galactic latitude (right column). The hatched bins (red) represent the actual number of groups identified and the non-hatched bins (blue) represent the expected number of groups derived from the survey coverage.
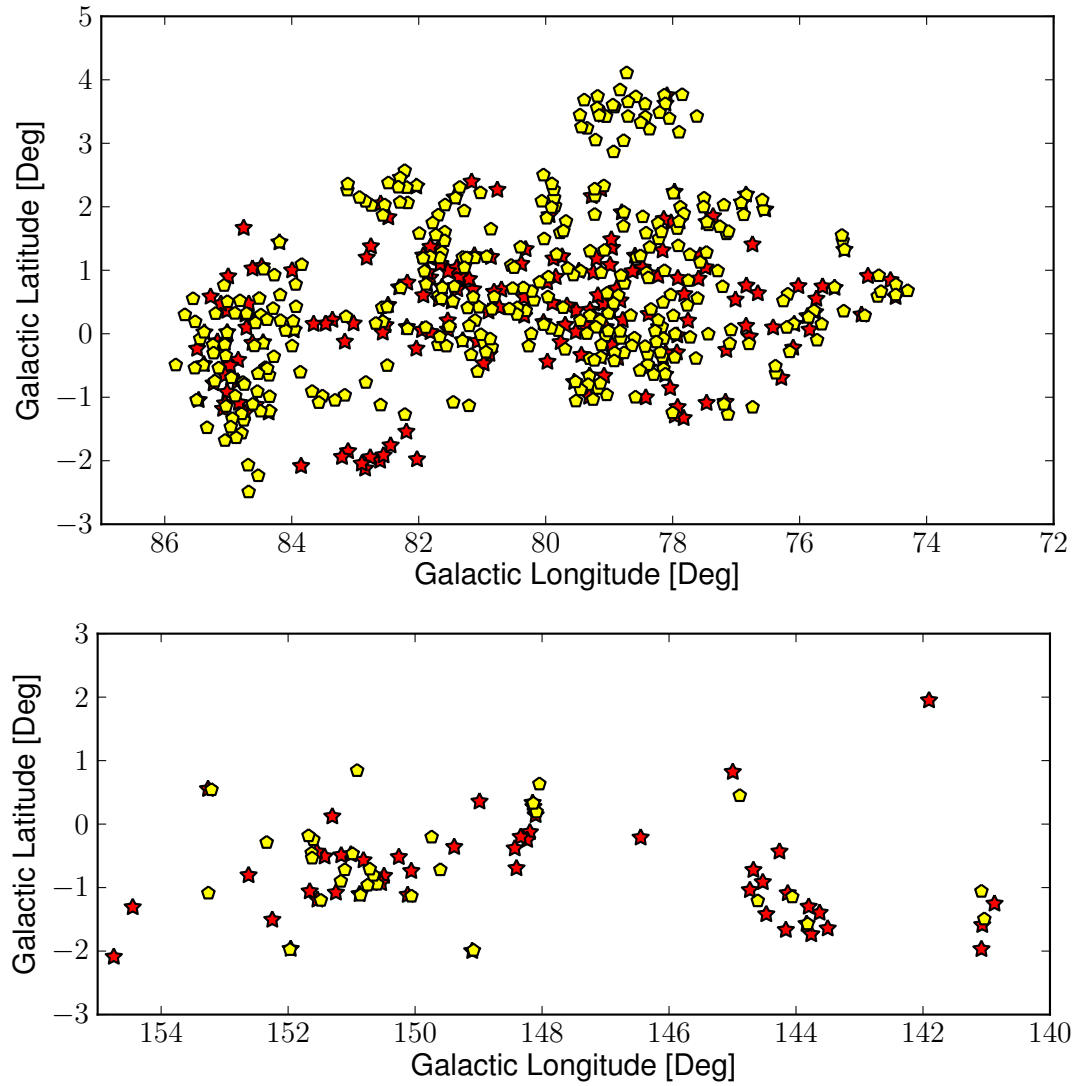
Figure 5.4: The spatial distributions of all jet (stars) and PDR (pentagons) groups within Cygnus (top) and Auriga (bottom).

Planetary Nebulae

There are 284 PNe in the UWISH2 survey after grouping, some of which were not known to exist beforehand. Of the 284 PNe analysed, 167 (about 62%) are newly discovered and have not been listed prior as either PNe or PNe candidates (Froebrich et al., 2015). There are 32 which were known to exist prior but were thought to be objects different from a PN. An example of this includes two features previously listed as MHO in (Ioannidis and Froebrich, 2012a). This leaves 85 that were already known PNe. Because we identify PNe by their morphology and the lack of association with a star forming region, anything described as 'new' is still open to speculation and are hence only candidate PNe. These candidates will be further investigated and their status will be confirmed in future work (Gledhill et al., in prep).

The spatial distributions of PNe are displayed in Figure 5.5 which shows that the number of PNe observed in low Galactic longitudes ($l < 10°$) is relatively low. Figure 5.6, which plots the distributions of PNe across the GP and the expected number from the coverage, also shows that for low Galactic longitudes there are less observed. It also shows that for $l < 20°$ there are less PNe than expected for the majority of coverage. As mentioned earlier, this is in part due to the higher extinction in this general direction from the Sagittarius arm which lowers the detection limit resulting in potential candidates being too distant or obscured for detection. To support this claim, the all-sky 100 micron extinction maps created by Schlegel et al. (1998) show that the total extinction in a given line of sight is highest at the Galactic Centre ($l,b = 0,0$) and typically decreases as l and b move away from the Galactic Centre.

Additionally, jets and PNe possess different spatial distribution characteristics. Jets are connected to dust and are therefore concentrated around star forming regions whereas PNe trace older objects and possess a much smoother distribution. The diameters of PNe are generally greater than jet widths and hence are more extended . Becuase of this, PNe are detectable at further distances than jet features. Therefore, the lack of PNe for low Galactic longitudes can likely be explained as

a combination of factors including extinction, spatial distribution and detection limits.

Approximately 92% of PNe are confined to the GP, which is roughly 1.25 per square degree. The remaining 8% are distributed in Cygnus and Auriga. Section one has approximately 1.02 PNe per square degree. Sections two, three and four have 1.38, 1.24 and 1.31 PNe per square degree respectively, suggesting PNe with H_2 emission are spread uniformly across the GP. We could speculate that if any candidates were undetected at the lower Galactic longitudes then the densities would be different. Table 5.3 separates PNe based on whether they are newly discovered candidates, reclassified or were known beforehand and then lists the numbers of each found in different regions. In the first section of the GP, 53.3% of PNe detections came from 'New' candidates with approximately 0.61 per square degree. In section two 49.3% of the PNe are 'New' candidates with a density of 0.68 per square degree. For section three, about 66.2% of the PNe are 'New' candidates, forming a density of 0.83 per square degree. Finally, 57.8% of PNe in section four are 'New', with a density of 0.80 per square degree. Contrary to this, previously known PNe are much less abundant with approximately 0.16 per square degree observed in section one, 0.52 per square degree in section two, 0.36 in section three and 0.39 per square degree in section four. A detailed list of all PNe in the survey can be found in Table C.1 within Appendix C. In Appendix E, Figures E.1 and E.2 show the spatial distributions of the candidate, reclassified and previously known PNe and are scaled to the total flux and area of the specific PN. They show that the new candidates possess typically less flux and are less extended than the known PNe. This indicates they are likely pre-PNe (protoplanetary nebulae).

Table 5.3: Table showing the split of new PNe candidates, reclassified PNe (existed in literature as a non-PN before UWISH2) and already known PNe. Rows describe the different areas of the survey (GP, Cygnus and Auriga) and the 'GP' row precedes a split into four equal wedges of Galactic longitude defined as section one ($-4° < l < 14°$), section two ($14° < l < 32°$), section three ($32° < l < 50°$) and section four ($50° < l < 68°$). For the New PNe candidates within the GP, each section lists in brackets the percentage of members where the total new PNe candidates within the GP is 100%.

Region in Survey	New	Reclassified	Old
		[number of]	
GP	152 (100%)	29	80
— Section One	27 (17.7%)	8	10
— Section Two	39 (25.7%)	10	30
— Section Three	49 (32.2%)	3	21
— Section Four	37 (24.3%)	8	19
Cygnus	11	1	4
Auriga	4	2	1
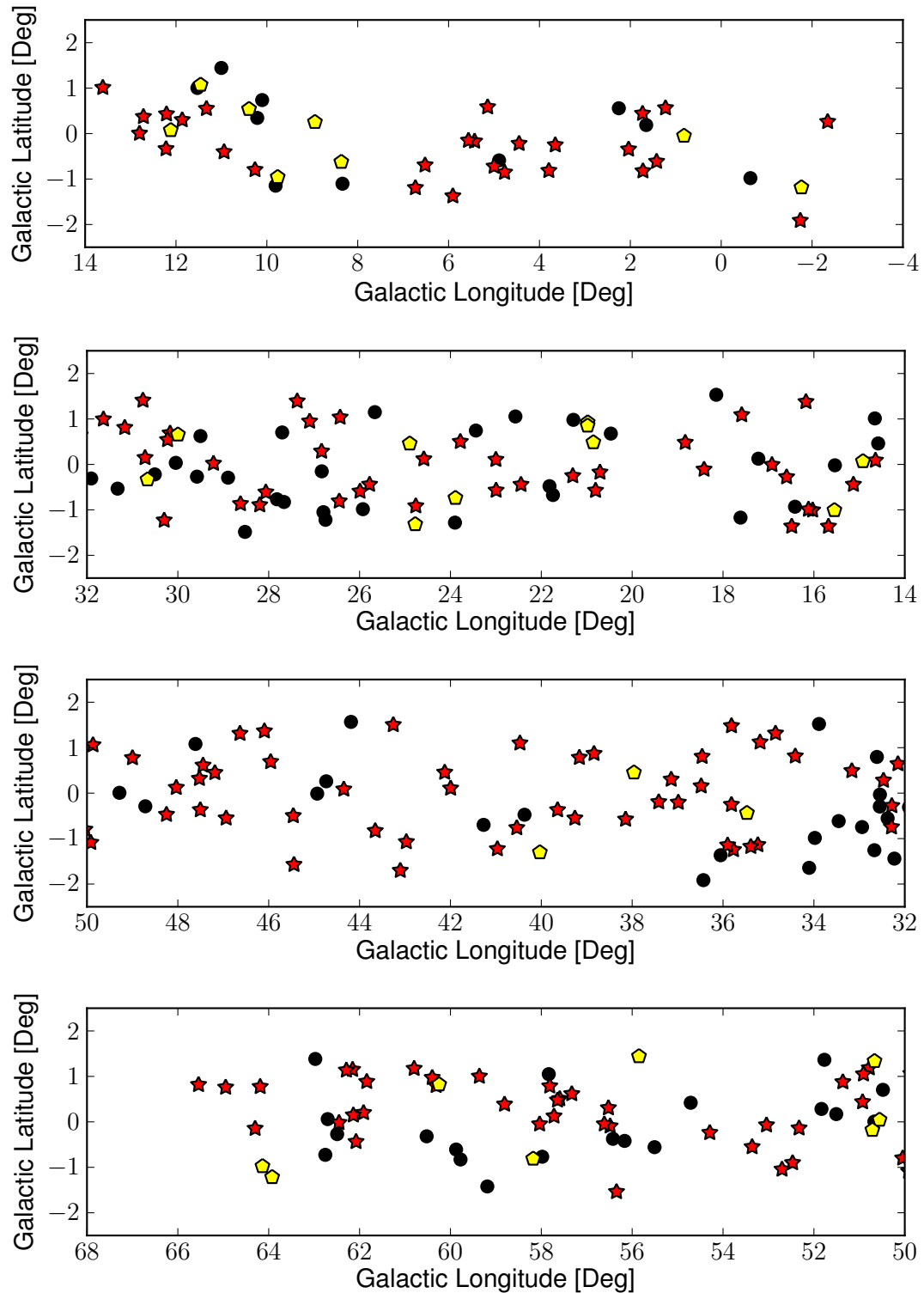
Figure 5.5: The spatial distributions of PNe within the four defined sections of the GP. The top plot represents section one with sections two, three and four following in descending order. The markers represent new PNe candidates (stars), previously identified objects but not a PN (pentagons) and previously known PNe (circles).
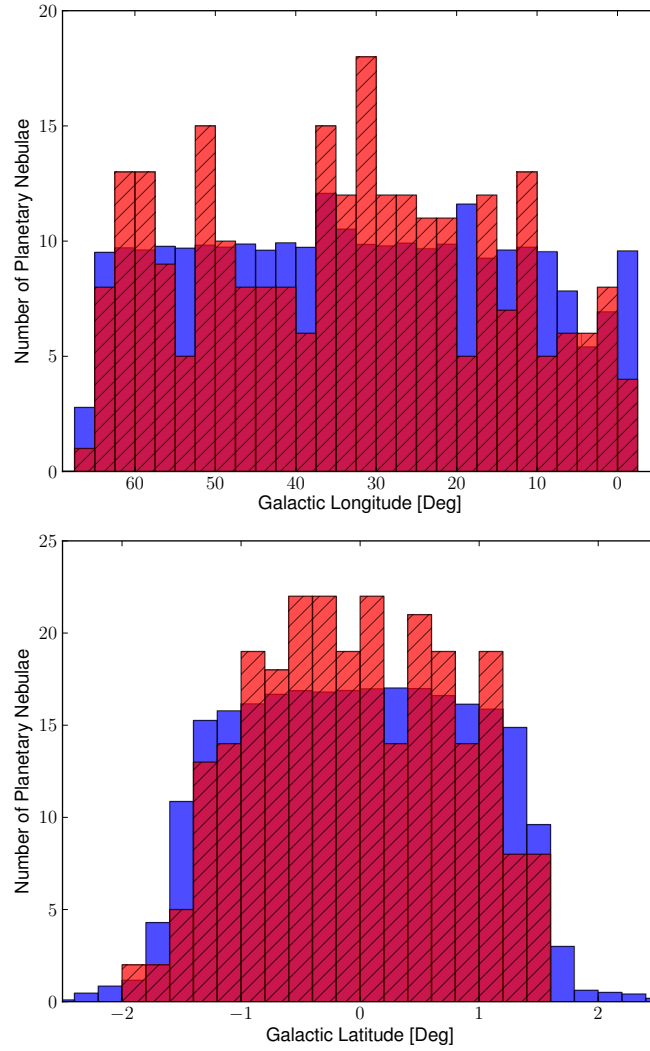
Figure 5.6: Plots of the distribution of the PNe along the GP found per 2.5 degrees Galactic longitude (top) and 0.2 degrees Galactic latitude (bottom). The hatched bins (red) represent the actual number of PNe identified and the non-hatched bins (blue) represent the expected number of PNe derived from the survey coverage.

Supernovae Remnants

As previously stated, there are 30 confirmed SNRs with extended H_2 emission in this survey. These were manually grouped as the grouping software determined that there are 78 different remnants, a factor of 2.6 more (Froebrich et al., 2015). Table 5.4 lists the details of the SNRs in the survey including their UWISH2 name, location, area and size, total and median fluxes, number of features that constitute it and, if applicable, the alternative name from previous literature. Sizes and alternative names were acquired from (Green, 2014) whilst the area and fluxes were supplied by me.

The SNRs W 28 and W 44 are responsible for the majority of the features and SNR flux with 77.8% of all features and 83.5% of the total flux (26.5% and 57.0% respectively). An example SNR, W 49B, is given in Figure 5.7 in both JKH_2 colour and $H_2 - K$ (including polygons). W 49B is a likely example of a shock-excited SNR, evidenced by the bright red radio filaments in the colour image. These are SNRs interacting with MCs, and the supernova blast wave meeting a dense environment. The SNR W 49B is very bright in H_2, and other bright SNRs (W 28, 3C391 and W 44) show similar characteristics. A much more detailed discussion of SNRs is in preparation by Lee et al. (in prep).
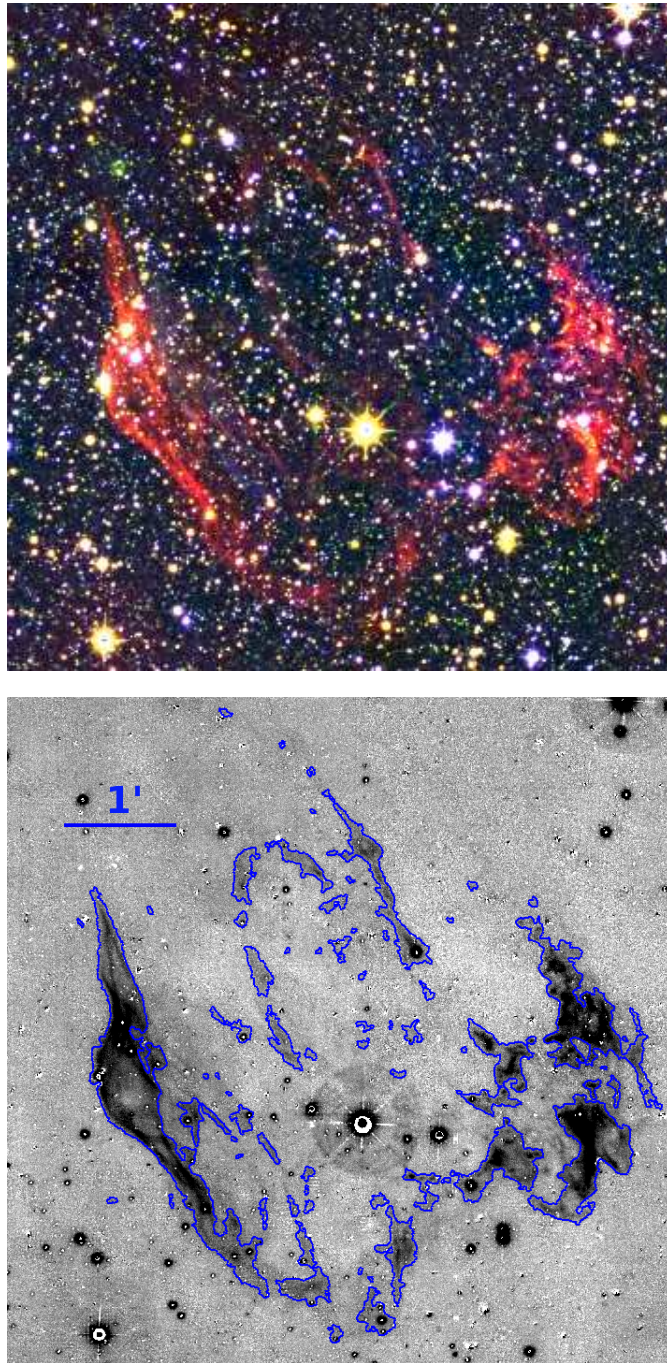
Figure 5.7: **Top:** A JKH$_2$ colour-composite image showing shocked H$_2$ filaments in the supernovae remnant known as W 49B (Froebrich et al., 2015). **Bottom:** The H$_2$ – K difference image (dark areas have higher intensity) with individual features contained in polygons. W 49B can be found (mostly) in tile *H2_l39_71___59* within image *w20100819_00434_x*.

Table 5.4: A list of SNRs, grouped from individual features in our survey, which contain extended H_2 emission line features. The majority of information is taken from (Green, 2014), which includes an objects position in both Galactic co-ordinates (listed to one-tenth of a degree) and Right Ascension and Declination. Listed is also the angular size of the remnants in arcminutes, the flux density at 1GHz in jansky (derived, not measured), the spectral index. Additionally, the type of SNR refers to either a 'shelled', 'filled-centre' or 'combination (of both)' and is given as 'S', 'F' or 'C' respectively. If a remnant has a given name in other literature, the name has been supplied. The '?' notation adjacent to any data entry implies inaccuracy and hence lack of confidence for a definitive value or category. Information listed but not taken from (Green, 2014) includes the areas, the total fluxes, F_{tot}, and median fluxes, F_{med}. Note that G6.5−0.4 also overlaps with several extended H_2 features. However, due to their visual appearance we attribute all of these to W 28.

Name	RA	DEC	Size	Area	1 GHz flux	Spectral	F_{tot}	F_{med}	Number of	Type	Other
	(J2000)		[arcmin]	[arcmin^2]	[Jy]	index	[10^{-15} W m^{-2}]		features		name
G1.0−0.1	17:48:30	−28:09	8	0.12	15	0.6?	0.24	0.22	4	S	
G1.4−0.1	17:49:39	−27:46	10	0.076	2?	?	0.69	0.18	7	S	
G5.5+0.3	17:57:04	−24:00	15x12	0.28	5.5	0.7	1.12	0.82	8	S	
G6.1+0.5	17:57:29	−23:25	18x12	0.052	4.5	0.9	0.11	0.10	3	S	
G6.4−0.1	18:00:30	−23:26	48	34.8	310	varies	122	86	1530	C	W 28
G9.9−0.8	18:10:41	−20:43	12	0.11	6.7	0.4	0.09	0.09	20	S	
G11.2−0.3	18:11:27	−19:25	4	1.70	22	0.5	5.2	3.2	77	C	
G13.5+0.2	18:14:14	−17:12	5x4	0.049	3.5?	1.0?	0.08	0.06	6	S	
G16.0−0.5	18:21:56	−15:14	15x10	0.40	2.7	0.6	1.6	0.53	47	S	
G18.1−0.1	18:24:34	−13:11	8	0.34	4.6	0.5	2.4	0.76	48	S	
G18.9−1.1	18:29:50	−12:58	33	0.80	37	0.39	1.1	0.97	102	C?	
G21.6−0.8	18:33:40	−10:25	13	0.020	1.4	0.5?	0.02	0.02	5	S	
G21.8−0.6	18:32:45	−10:08	20	1.75	65	0.56	4.3	3.7	119	S	Kes 69
G24.7+0.6	18:34:10	−07:05	30x15	0.42	20?	0.2?	0.47	0.44	70	C?	
G27.4+0.0	18:41:19	−04:56	4	0.054	6	0.68	0.09	0.09	9	S	4C−04.71
G27.8+0.6	18:39:50	−04:24	50x30	0.11	30	varies	0.15	0.14	3	F	
G28.8+1.5	18:39:00	−02:55	100?	0.046	?	0.4?	0.04	0.04	7	S?	
G31.9+0.0	18:49:25	−00:55	7x5	2.32	25	varies	15.6	7.2	102	S	3C391
G32.1−0.9	18:53:10	−01:08	40?	0.55	?	?	1.8	0.70	71	C?	
G32.8−0.1	18:51:25	−00:08	17	2.20	11?	0.2?	7.5	2.9	203	S?	Kes 78
G33.2−0.6	18:53:50	−00:02	18	0.12	3.5	varies	0.71	0.17	12	S	
G34.7−0.4	18:56:00	+01:22	35x27	62.9	250	0.37	263	157	2852	C	W 44
G38.7−1.3	19:06:40	+04:28	32x19?	0.26	?	?	0.57	0.29	43	S	
G39.2−0.3	19:04:08	+05:28	8x6	0.52	18	0.34	0.75	0.70	49	C	3C396
G43.3−0.2	19:11:08	+09:06	4x3	5.0	38	0.46	13.6	10.8	107	S	W 49B
G54.4−0.3	19:33:20	+18:56	40	0.39	28	0.5	0.51	0.39	54	S	HC 40
G65.1+0.6	19:54:40	+28:35	90x50	0.13	5.5	0.61	0.06	0.09	7	S	
G357.7+0.3	17:38:35	−30:44	24	0.032	10	0.4?	0.09	0.08	2	S	
G359.0−0.9	17:46:50	−30:16	23	0.15	23	0.5	0.27	0.28	10	S	
G359.1−0.5	17:45:30	−29:57	24	1.31	14	0.4?	10.3	3.3	53	S	
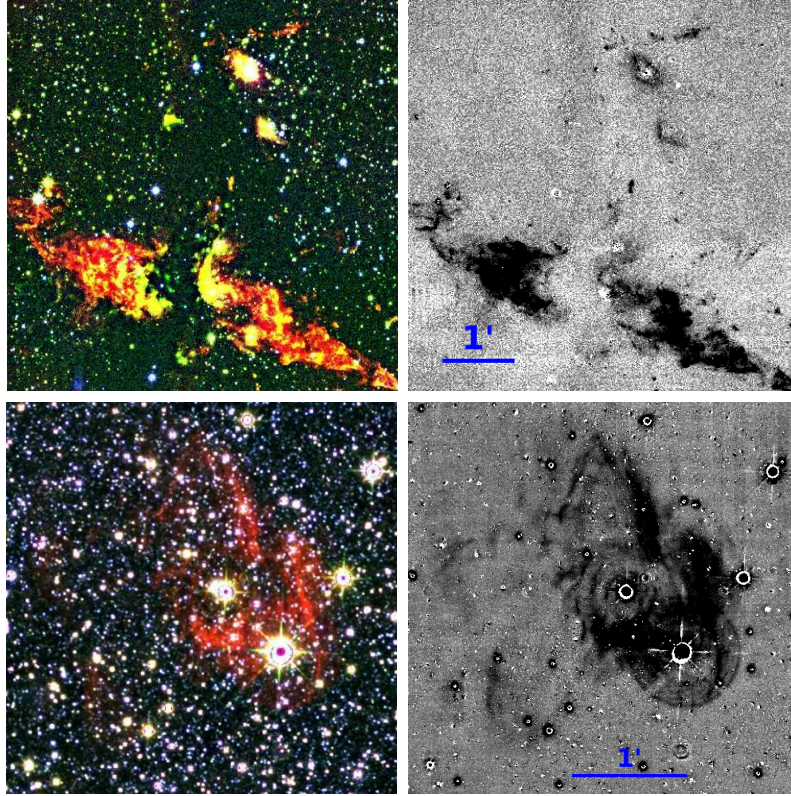
Figure 5.8: Top: A JKH$_2$ colour-composite image of the active star forming region DR 21 (left) and the H$_2$ – K false-colour difference image of the same region (right). The star cluster [BDB2003] G081.71+00.58 and HII ionised region MSX6C G081.7131+00.5792 can be seen above DR 21. This feature can be found in the tile *H2_l70_107_-131* in image *w20131119_00188_x*. **Bottom:** A JKH$_2$ colour-composite image of the bright PNe called PN G017.6-01.1 (left) and the H$_2$ – K false-colour difference image, which is highly saturated, of the same region (right). This can be found in the tile *H2_l15_50_---32* within image *w20100612_00382_y*.

Flux and Area Distributions

From Table 4.1 in Chapter 4, jets in Cygnus contain a much greater amount of flux both in total and per square degree than that of any other region. It is then unsurprising that PDR features (likely PDRs), which are also indicators of star forming regions, show a similar relationship. As for the GP, we have seen before that the majority of both individual features and groups occur at lower Galactic longitudes. With the visual aid of Figures 5.9 and 5.10 it is possible to obtain a broader overview of the flux and area distributions of the groups. The figures look at groups in the Cygnus and GP regions respectively. They represent spatial distributions where circular plot markers of varying radii are scaled to either the

84

total flux or the total area of all features within the group. The centre of the circle coincides with the group centre in Galactic co-ordinates. These figures clearly show the large portion of total flux that groups in Cygnus contribute, even with slightly less than half the number of jet groups and just over a third of the PDR groups than that of the GP. Regions like DR 21, a large star forming region, and the jet group containing several Herbig-Haro objects (HH 643 - HH 652) are responsible for over $2 \times 10^{-14} W m^{-2}$ alone, or almost a quarter of all jet flux in the survey. The five brightest jet groups in the survey are native to Cygnus.

I discussed previously the greater flux found at the low Galactic Longitudes of the GP. From the left panels of Figure 5.10, which show the flux weighted spatial distributions of jet groups, PNe and PDR groups, this conclusion is very visually apparent. Objects likely to be PDRs are relatively bright at $l < 20°$ whilst the abundance of groups and their average brightness decrease between $20° < l < 40°$. Between $40° < l < 67°$ there is no large increase in group abundance but a noticeable increase in brighter groups. Likewise, the greater abundance of jets at lower Galactic longitudes is apparent. Whilst there are more groups at the lower Galactic longitudes, there is a much smoother distribution of groups with larger than average total fluxes across the GP than compared to the PDR groups. No jet group stands out as particularly bright.

When compared to the distribution weighted by area, we can see that the groups with large total flux do not necessarily have a large total area. It is likely that the large flux groups that possess a small area are affected by saturated stars in our images. This comparative is also where the PDR groups differ. Visually, there is much more of a correlation between total flux of a group and the total area of that group, especially in larger groups. However, there are also many contradictions to these observations of flux versus area in both jet and PDR groups so we are unable to definitively draw conclusions on a relationship until factors such as saturated stars within features are properly accounted for.

Concerning PNe, there are a low fraction which contribute a large flux but there is a even distribution of low and intermediate contributors across the GP. The

object PN G017.6-01.1 is responsible for about 45% of the PNe flux of the entire survey. Upon inspection, individual features that make up this PNe enclose ten significant saturated stars which has had an effect on the total flux. Other factors can also determine the amount of H_2 emission in PNe such as the morphology and the age. With regards to the morphology, bipolar PNe are frequently observed to possess significantly more H_2 emission (Aleman and Gruenwald, 2004). A study by Gledhill and Forde (2015) found that advanced PNe showed very weak H_2 emission as it is likely the molecules have dissociated. Spatial position along the plane alone does not seem to play a huge role in determining PNe flux. Like before, some PNe with large flux also enclose a large area of emission but there are examples of smaller fluxes with larger areas. For example, in our catalogue PN G040.3-00.4, with a group centre located at $l, b = 40.3704°, -0.4752°$, has an area of 0.33 square arcminutes (relatively large) yet the total flux is low at about $9.7 \times 10^{-18} \, Wm^{-2}$. For instances concerning image artefacts (saturated and variable stars for example), the one pixel median surface brightness (multiplied by area) would be a better indicator of the flux. This shall be further discussed in Chapter 6.
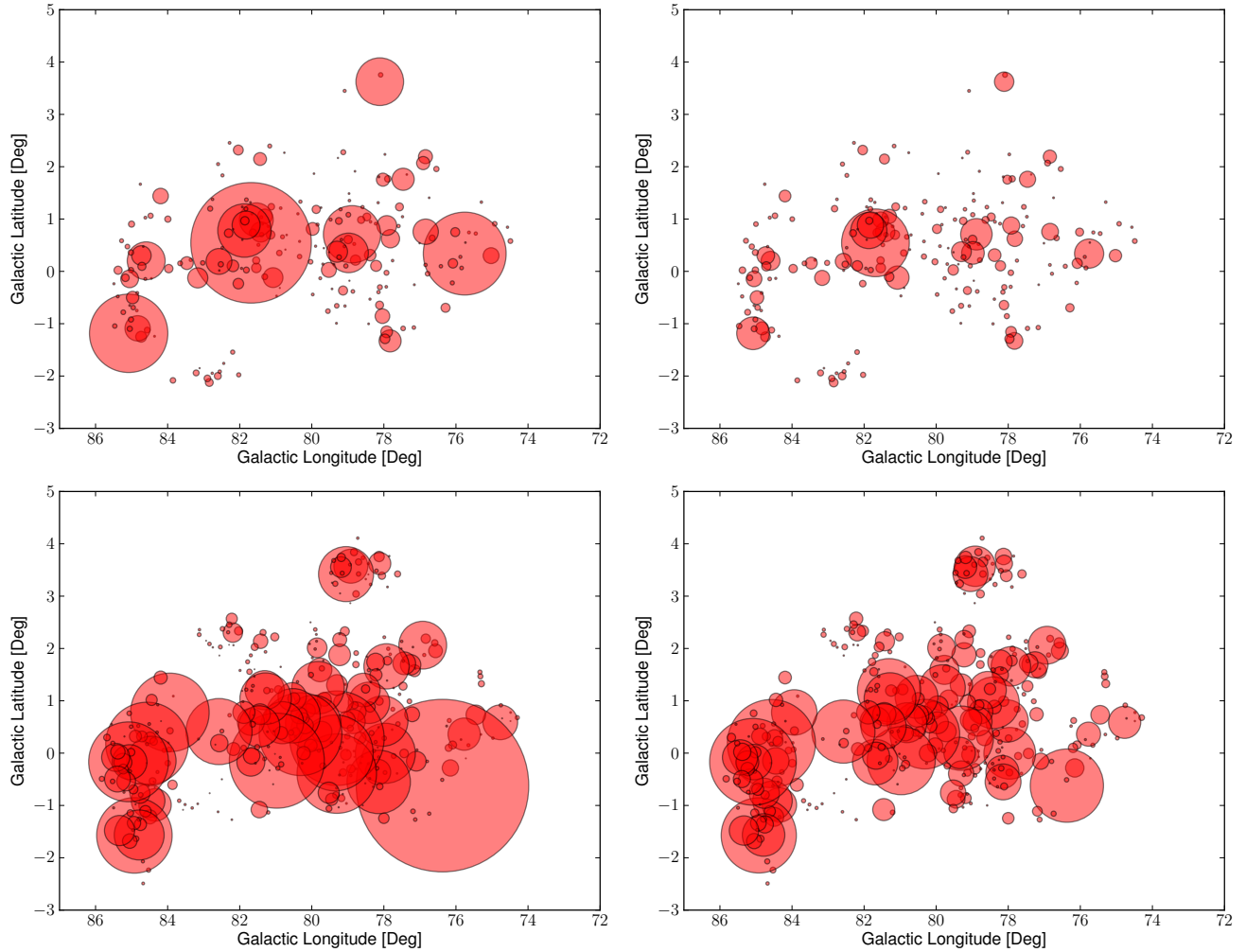
Figure 5.9: Figures showing distributions of jet groups (top) and PDR groups (mostly PDRs, bottom) in the Cygnus region. They represent the spatial distribution of each class in Galactic co-ordinates where the circle size is scaled to either the total flux of the group/object (left column) or the total area in the sky covered by the group/object (right column). The same scaling has been applied for all figures of each type (flux or area). This scaling is carried over to Figure 5.10 for comparison.
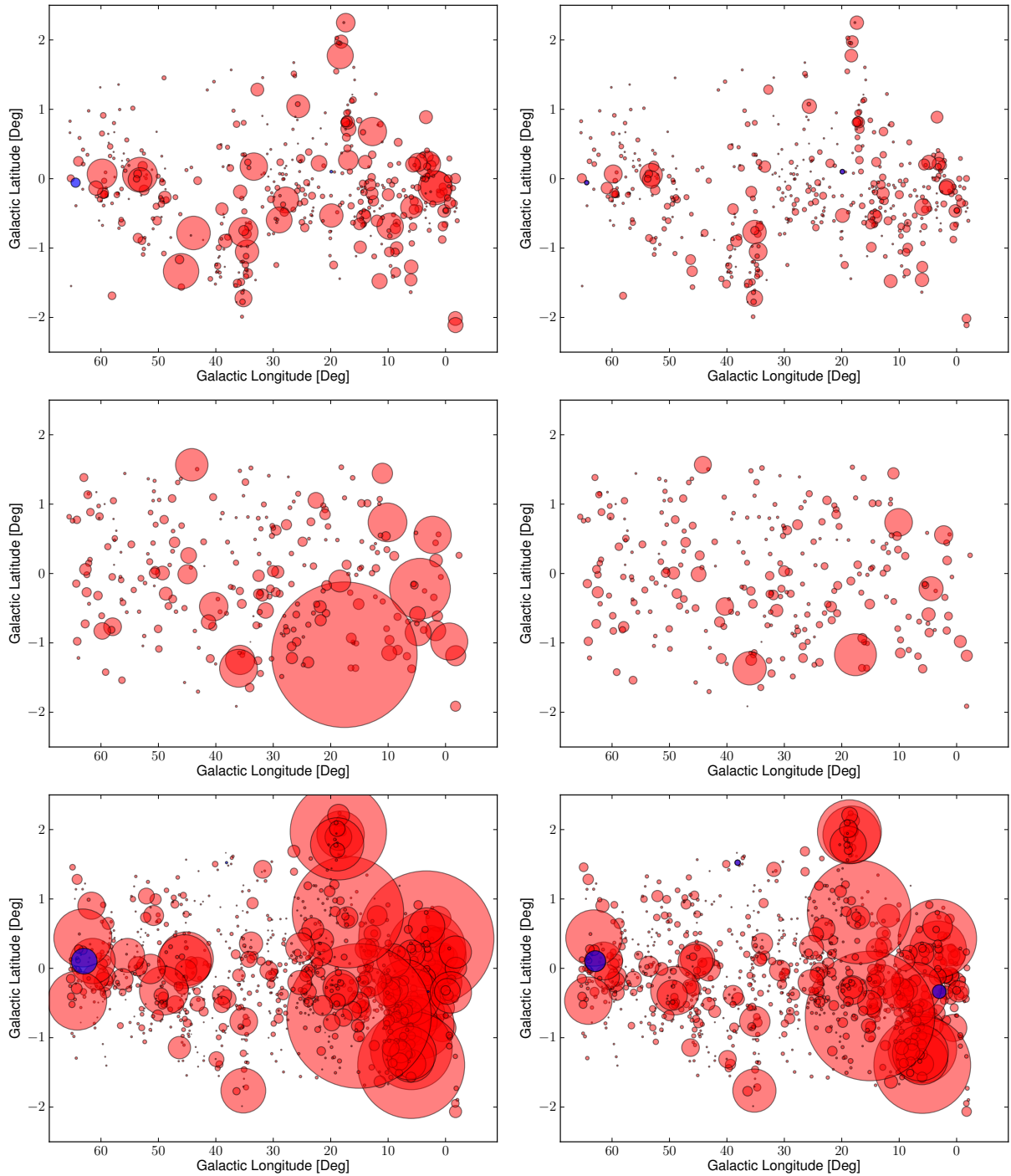
Figure 5.10: Figures showing distributions of jet groups (top), PNe (middle) and PDR groups (mostly PDRs, bottom) in the GP. They represent the spatial distribution of each class in Galactic co-ordinates where the circle size is scaled to either the total flux of the group/object (left column) or the total area in the sky covered by the group/object (right column). Some of the jet and PDR groups had negative total fluxes. They can be identified by the blue colouring of their circles. The same scaling has been applied for all figures of each type (flux or area). The scaling has been carried over from Figure 5.9 for comparison.

Chapter 6

Comparison of Photometry Methods

This chapter introduces a second flux estimate for the H_2 features and compares it to the total flux values. I advise which one of the flux estimates is better to use for each classification type. I identify some groups which show large differences in the two flux estimates.

6.1   The Median Surface Brightness

A subject that has been heavily mentioned and discussed in previous chapters is the presence of saturated stars and other artefacts in our images which can influence the total flux of features (and their subsequent objects/groups). Prior to photometry, a large amount of effort was put into reducing the number of artefacts in our images and the effects they would have to the total flux. There are still artefacts that remain.

At the end of Chapter 5 I suggested using the one-pixel median surface brightness (MSB) multiplied by the area as an alternative value for the flux of a feature. This method of photometry would in theory be able to ignore the extremely high and low pixel intensities of residual stars and produce a more reliable value than the total flux. My photometry program was responsible for producing the one-

pixel median surface brightness for a region. This is the median pixel value of the H_2 feature minus the median pixel value of the background after 3σ clipping. While using this method of photometry is preferable in cases with very bright or negative pixel intensities, there are also scenarios where the total flux would be preferred over the median surface brightness. If the automatic detection program encapsulates the H_2 emission but also includes some of the background noise then the median background intensity around the H_2 feature may become similar to the median background of the feature. This results in a median background corrected pixel intensity close to zero (or negative). If this is the case, the MSB could greatly underestimate the flux of the H_2 emission. Similarly, the MSB could underestimate the H_2 flux if the emission is highly non-uniform in nature. With both photometry methods having drawbacks, I compare the two flux estimates for each feature.

An example showing the difference in the two methods of photometry can be found in Figure 6.1. Effectively, we are comparing the one-pixel MSB to that of the one-pixel mean surface brightness, as the latter value is simply the total flux divided by the area. The figure uses a 100-pixel region, the smallest possible region for automatic detection ($2"\times2"$). If 90 pixels have an intensity (count) of one and 10 pixels have an intensity of 10, the total flux of this region is 190 counts, but the background corrected one-pixel MSB (assuming a median background intensity of zero) is one count. Multiplying this by the area leads to a flux value of 100 counts. This figure can demonstrate two possible scenarios:

The high intensity region is an artefact:
If the bright pixels represent an artefact in our image, then our desired flux is actually 90 counts (90 pixels $\times$ 1 count) and the sum of all counts (total flux) is 190, but the median count multiplied by the area is 100 (if background is zero). Therefore, using the MSB would result in a better estimate.

The low intensity region is encapsulated background noise:

Assume now that the central 10 pixels is the H_2 emission and the 90 surrounding pixels is background noise which has been included within the feature boundary and is wrongfully treated as H_2 emission. This scenario would produce a median count of one. We can assume the one-pixel median background value to be close to a value of one due to the included pixels in the feature boundary. This results in a background corrected median pixel value of near-zero which, when multiplied by the area, will be much lower than the preferred 100 counts from the real emission. An example of this occurring would be in features where the majority of flux is contained in a small fraction of the feature area (like jet knots).

Real features are more extended than this and much more complex in terms of shape and pixel intensities, which can range from hundreds to thousands of counts. This prior example is applicable for our smaller regions but the increased complexity for more extended H_2 features makes it much harder to predict which photometry method would work best. From this point on, the MSB flux refers to the flux obtained from the product of the one-pixel, background corrected, median surface brightness of a feature and the area of emission.
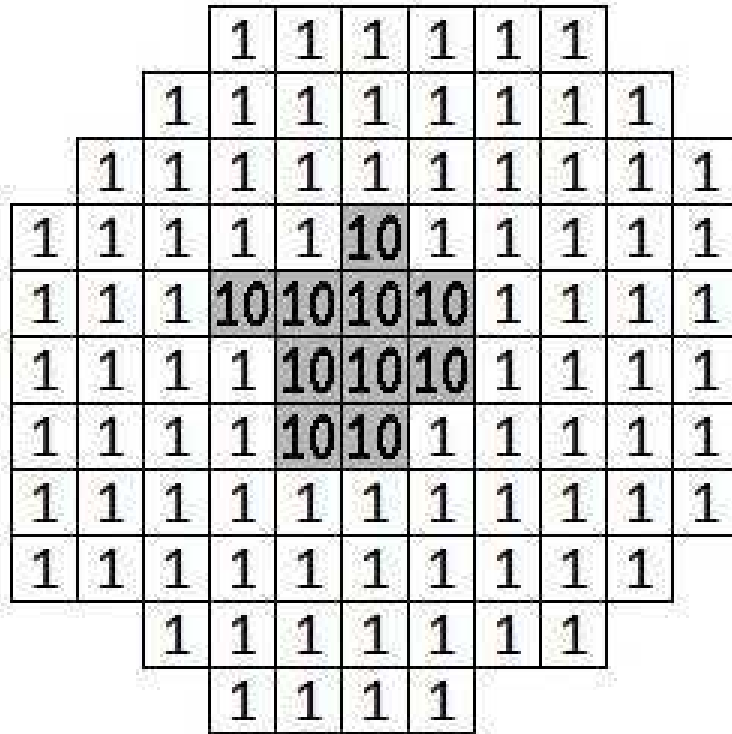
Figure 6.1: A unrealistic but simple representation of a 100-pixel (four square arcseconds) region comprised mostly of low intensity pixels. A small fraction of pixels have a higher intensity which represents a bright residual artefact.

6.2 Comparison of Flux Estimates

Figure 6.2 compares the photometry outcomes in the GP of the total flux and the MSB flux for jet groups, PNe and PDR groups (top to bottom) respectively. The left panels of the figure represent the fraction of flux at each Galactic longitude if the total flux was used. These were discussed in Chapter 4. The right panel shows the distribution of the MSB flux. Figure 6.3 is similar to Figure 6.2, but compares the photometry differences in the Cygnus region. Note these figures concern the grouped H_2 features, so individual H_2 features with with central Galactic co-ordinates in one bin may belong to a group whose centre lies in an adjacent bin. For cases such as this, the individual H_2 feature contributes its flux to the bin of the group centre.

Jet Groups

The top row of Figure 6.2 concerns jet groups and shows noticeable differences between the photometries. In areas where there was once huge fractions of total flux there is now a relatively low fraction of MSB flux, especially between $43° < l < 44°$ and $46° < l < 47°$. Regions like $17° < l < 18°$ have shown a relatively large increase in flux when the MSB flux is applied. The brightest region of the GP in total-flux photometry, $1° < l < 2°$, is no longer the brightest in MSB photometry. The brightest region in MSB photometry within the GP occurs between $35° < l < 36°$ which is the location of the molecular cloud GAL 035.2-00.74. When analysing the differences in photometry for jet H_2 features in Cygnus, represented in the top row of Figure 6.3, we observe a lesser amount of change in the flux distribution than witnessed in the GP. The most noticeable change is that regions at a Galactic longitude between $81.50° < l < 81.75°$, the location of DR 21, contribute a higher fraction of flux when using the MSB photometry. The relative flux in this range increases from about 29.6% to 34.9%. Other areas of Cygnus will therefore see a decrease in the relative flux. The most prominent example of this is between

$85.00° < l < 85.25°$ which saw a flux fraction decrease from about 12.5% to 5.6%.

Planetary Nebulae

The middle row of Figure 6.2 contrasts the relative fluxes from the two photometry methods for the PNe (candidates). The PN designated PN G017.6-01.1, whose large flux was discussed in Chapter 5, remains by far the brightest object. As discussed previously, this particular PN is relatively nearby and as such it is very extended and very bright. In total-flux photometry, it produced 45.0% of the relative PNe flux in the GP. This has seen a decrease to 25.1% in MSB photometry. Because this PN still covers a very large area it had the capacity to retain a large amount of the flux. Because of this massive decrease, most bins have seen an increase in height but the general shape of the distribution remains similar to before. The notable differences are minuscule for PNe in Cygnus, as shown in the middle row of Figure 6.3. This is likely due to the very low number of PNe identified. Aside from the large decrease in flux for PN G017.6-01.1, the photometry methods show good agreement for PNe.

PDR Groups

The bottom row of Figure 6.2 refers to the PDR groups. There is very little change in the histogram shapes within the GP with exception to $3° < l < 4°$ and $15° < l < 16°$. Using the total flux, PDR groups within these ranges were responsible for about 14.2% and 11.1% of the relative PDR GP flux respectively. When the MSB flux is used, the relative flux of the former region drops to about 9.2% and the latter increases to 16.1%. Aside from this, the rest of the histogram has minor fluctuations in bin heights which indicates an acceptable agreement between the two photometry methods. In Cygnus, the distribution also remains very similar between the two photometries. A large change includes a decrease of the relative

flux at $76.25° < l < 76.50°$. This region was and still remains the highest flux contributor for PDRs in Cygnus with a relative flux transition of 17.5% to 13.6%. Another decrease of the relative flux is observed at $79.25° < l < 79.50°$ with 12.7% decreasing to 9.8%. A small increase is seen at $84.75° < l < 85.25°$ (two adjacent bins).

Table 6.1, located at the end of this chapter, contains an arbitrary selection groups that contribute some of the greatest changes of flux when a different photometry is used. I include both fluxes and their group area, plus the group classification and the group centre Galactic longitude co-ordinate. If a group has a name given in previous literature it has been provided.
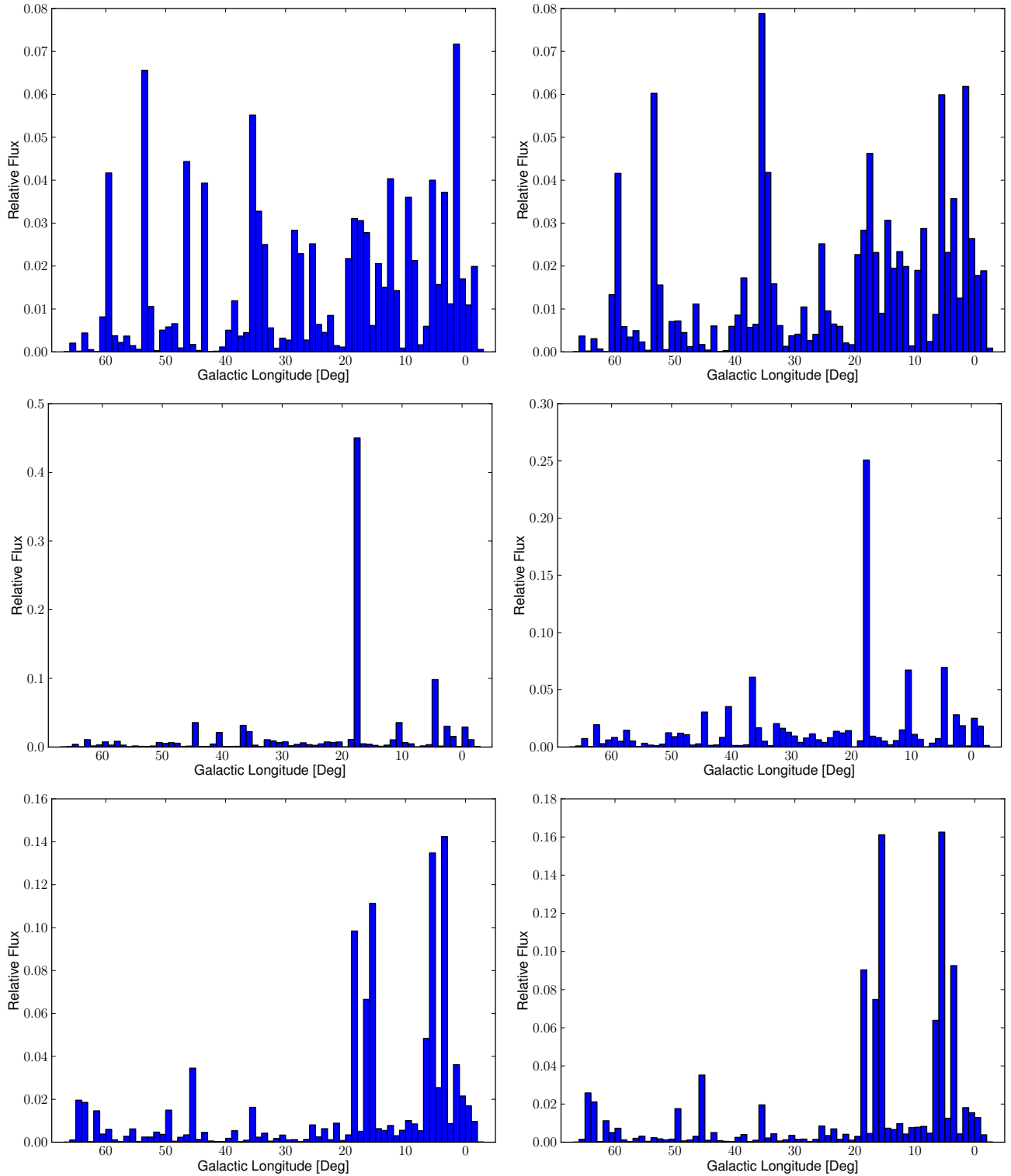
Figure 6.2: The flux distributions of jet groups (top), PNe (middle) and PDR groups (bottom) in the GP. The left panels describe the flux distribution using the total flux of groups whereas the right panels describe the flux distribution using the MSB flux.
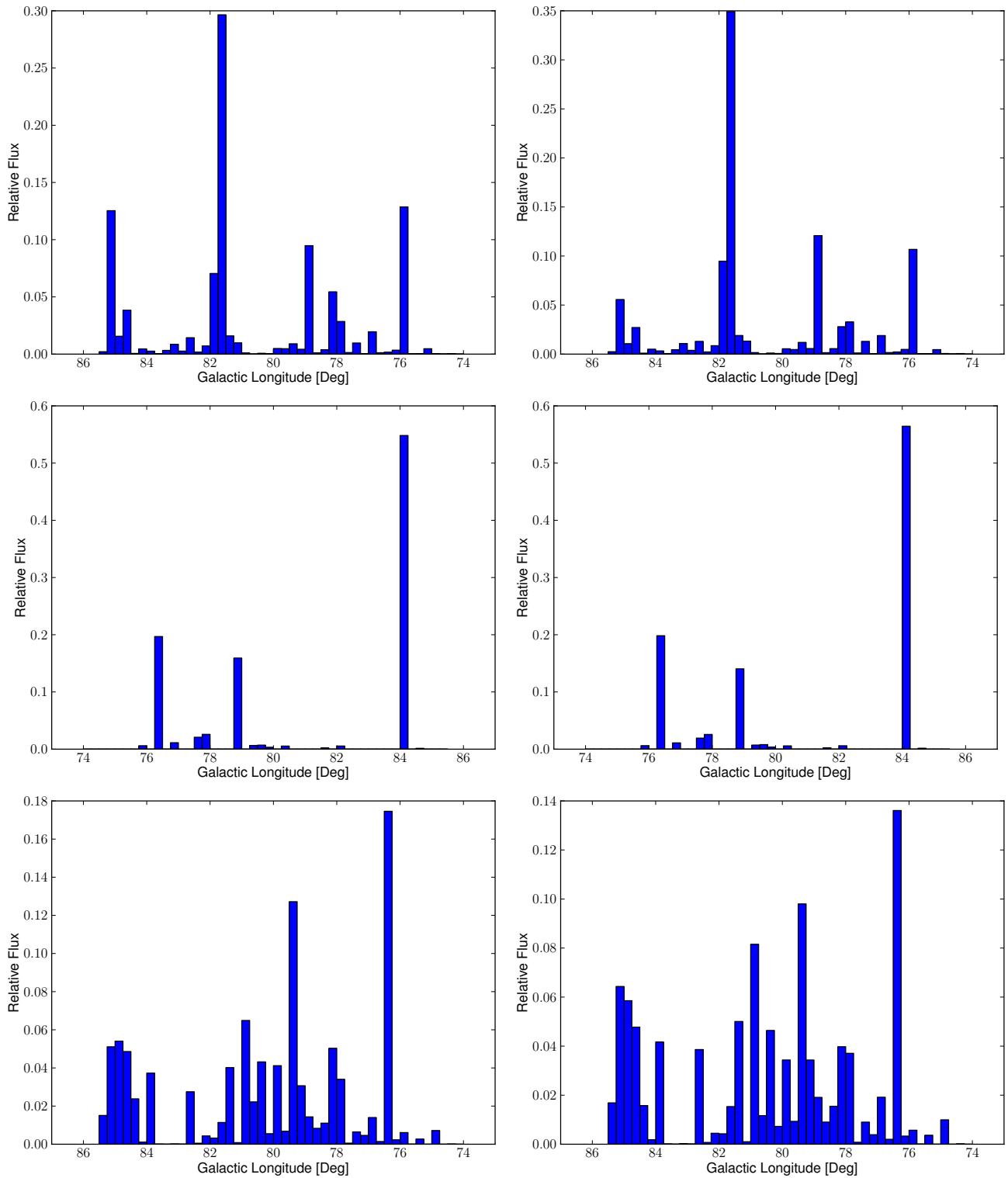
Figure 6.3: The flux distributions of jet groups (top), PNe (middle) and PDR groups (bottom) in Cygnus. The left panels describe the flux distribution using the total flux of groups whereas the right panels describe the flux distribution using the MSB flux.
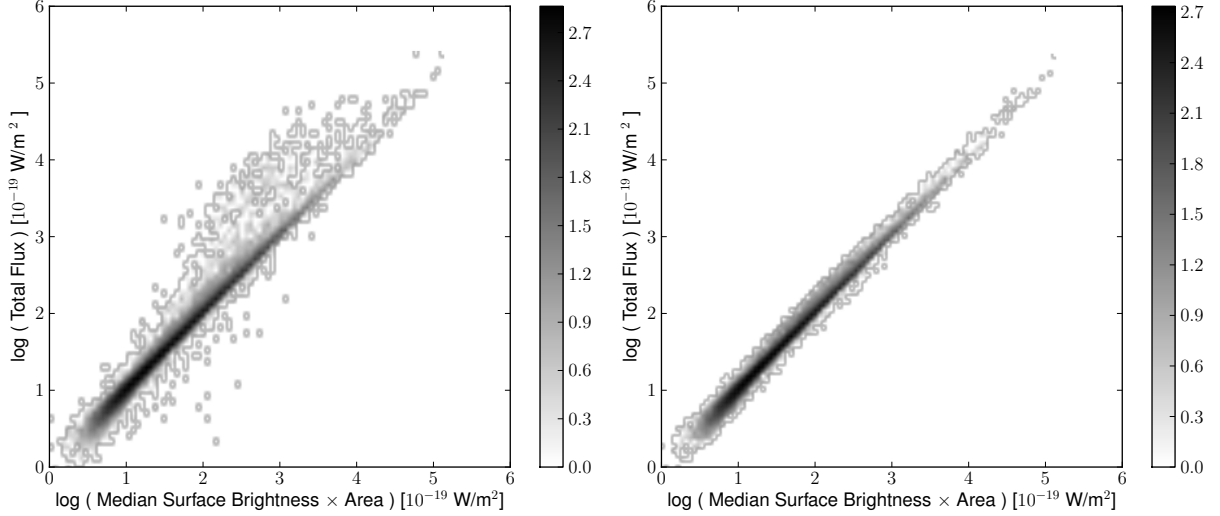
Figure 6.4: Density maps for the logarithms of the total flux versus the MSB flux with all individual regions (left) and individual regions whose ratio of the two flux values (before Log) lie between 1:2 and 2:1 (right). The grayscale indicates the Log of the density of objects in each positions (values in colourbar).

To check the agreement of the photometries, I have plotted density maps of the logarithms of the total flux versus the MSB flux for every H_2 feature of all types. This can be seen in Figure 6.4, where the left panel compares the ratios of all features and the right panel only shows the features whose ratios of the two fluxes lie within the range of 1:2 and 2:1, thus covering a 100% deviation. We choose this as we would expect a minimum accuracy of 100% to consider the agreement of the two photometry methods. Features with an agreement below 20% are deemed to be excellent due to the associated errors of the magnitude zero point and the airmass during the photometric conversion equation from Chapter 3.

Figure 6.5 describes the percentage of features for each classification type which possess photometric agreements within a given fractional deviation on the x-axis. All types of feature underwent a rapid increase between 10% and 20% before flattening out closer to 100%. We can see that $\sim 97\%$ of our features from the full catalogue are included within a 100% deviation and $\sim 82\%$ had an agreement within a 20% deviation.
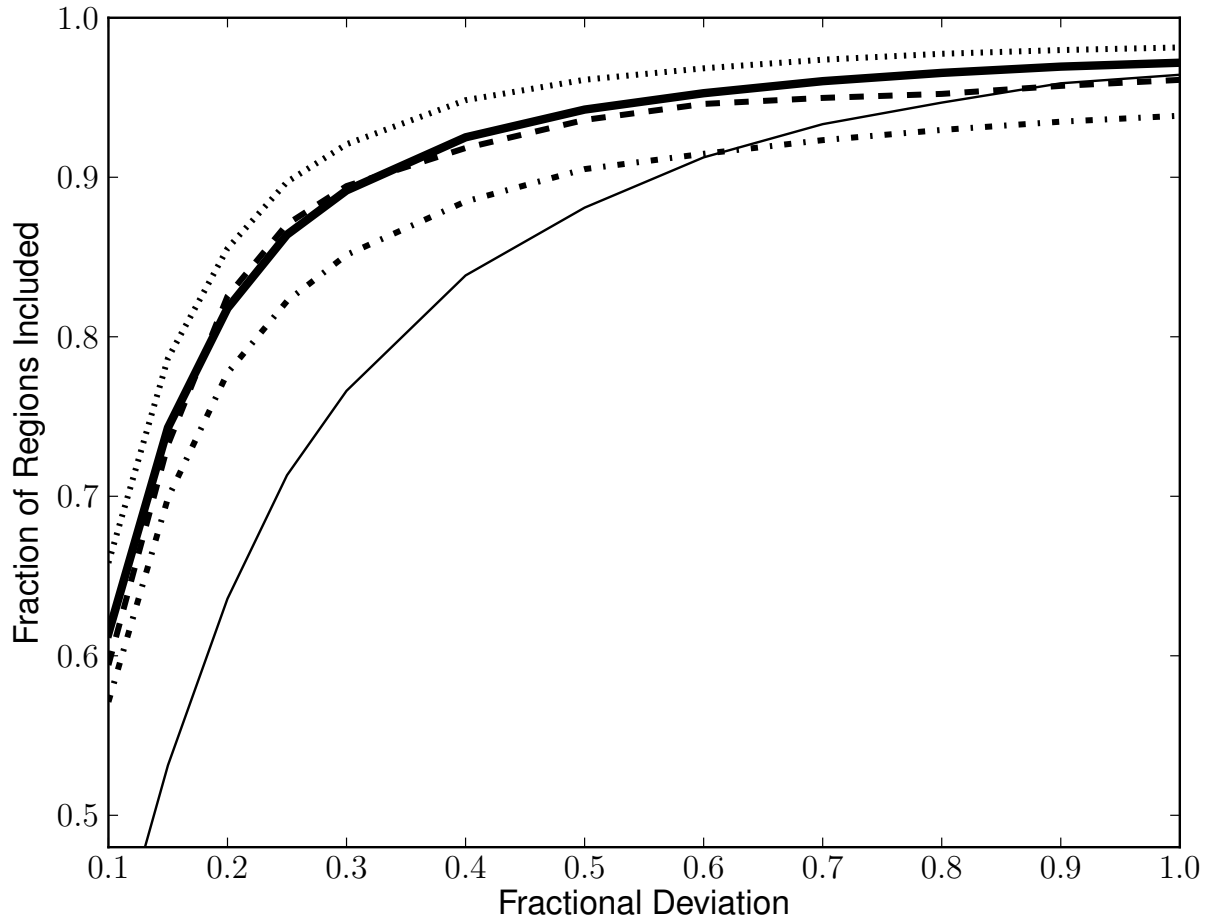
Figure 6.5: From their respective catalogues, the fraction of H_2 features whose ratio of both photometry flux estimates are smaller than a varying fractional deviation from unity. Steps increase in fractional increments up to a factor of 2. The different line styles represent the different types of features. In descending order, the lines at 100% deviation represent the PDRs (**dotted**), the full catalogue of features (**bold, solid**), the jet features (**thin, solid**), the planetary nebulae (**dashed**) and finally, the supernovae remnants (**dot-dash**).

The ratio of photometries for approximately 94% of SNR features and 96% of PNe features were within the 100% deviation of unity. Furthermore, about 78% of SNR features and about 83% of PNe features had a photometry agreement within 20%. This suggests either method of photometry is reliable.
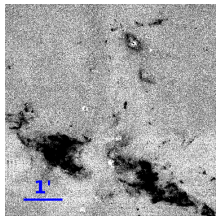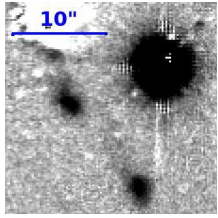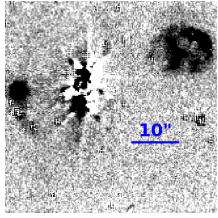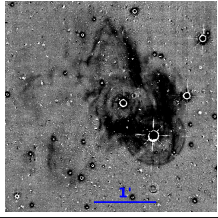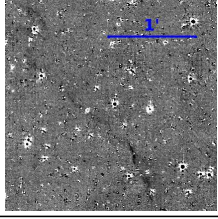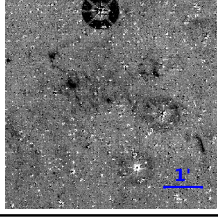
PDR features show a good photometry agreement of approximately 98% within 100% deviation and 86% within 20% deviation. Whilst 96% of jet/outflow features lie within a 100% deviation, only $\sim 64\%$ of features are within 20% deviation. These observations indicate that jet H_2 emission features show the least agreement between the two photometries (we have seen this from Figure 6.2). A likely reason for this is that large fractions of the total flux in jet features are contained within a few pixels in the jet knot. If this is the case then the MSB flux will probably be inaccurate.

I would therefore advise any reader to use the total flux for the photometry of any features classified as jets and to use the MSB flux for the photometry of SNR, PNe and PDR features because it eliminates the potential inclusion of unsubtracted or variable stars. I would also advise that if the reader requires a more accurate photometry of specific objects then it is best to re-run photometry ensuring only the desired H_2 emission features are selected (hence the thorough removal of all artefacts). Figure 6.4 demonstrates the difference in the full catalogue by removing objects with one photometry outcome substantially different from the other. In summary, we have secured confidence that the two methods of photometry achieved agreement within our minimum deviation for $\sim 97\%$ of all features whilst achieving excellent agreement within a deviation of 20% for $\sim 82\%$ of all features.
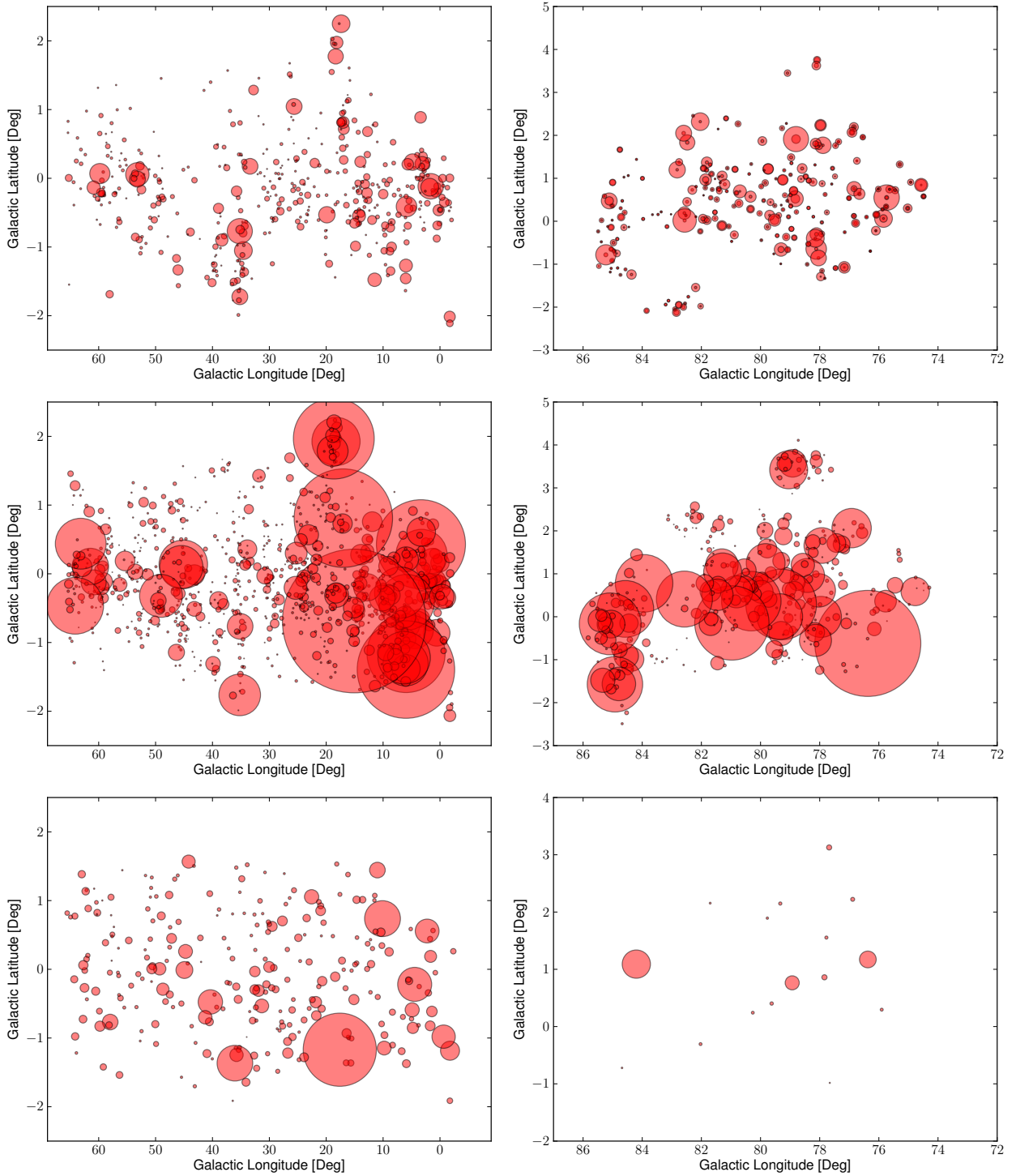
Figure 6.6: Figures showing distributions of jet groups (top), PDR groups (middle) in the GP (left) and Cygnus (right). The bottom figure shows the distributions of PNe in the GP only. They represent the spatial distribution of each type in Galactic co-ordinates where the circle size of is scaled to the median surface brightness times area (MSB flux). The same scaling has been applied for all figures and is the same scaling used in the total flux versions in Figures 5.9 and 5.10 in the previous section.

Table 6.1: Table showing some examples of grouped, false-colour H_2 emission features that underwent a large change in fluxes when a different photometry was applied. Listed is the type of group, the Galactic longitude co-ordinate of the group centre, both fluxes as well as the area that part produces the MSB flux. If the feature has an object with a name(s) listed in previous literature, then one example is presented. If a collective of objects exist then more than one may be named.

Image	Group Class	Group Centre [l]	Notable Group	Total Flux MSB [10^{-17} W m^{-2}]	Area [arcsec^2]
	Jet	81.68439°	DR 21	1556.0 1173.4	12294.04
	Jet	43.88666°	MSX6C G043.8896 -00.7835	175.6 10.4	198.45
	Jet	46.05182°	HH 32 HH 32A HH 32B HH 32C HH 32D	195.6 16.7	426.80
	PN	17.61528°	PN G017.6-01.1	3302.6 851.1	6864.53
	PDR	3.24126°	—	932.6 417.9	12576.81
	PDR	3.34822°	—	2853.8 1261.9	23986.96

Chapter 7

The Signal-to-noise Ratio

7.1 The Signal-to-noise Ratio of UWISH2 Features

This section looks at the signal-to-noise ratio, from this point abbreviated as S/N, associated with the H_2 features in UWISH2. The reciprocal of the S/N acts as a good indicator of associated uncertainty in the flux for a feature. Therefore, a higher value for S/N indicates a lower uncertainty in our fluxes. For sufficiently low values of fractional uncertainty $(\Delta F/F)$, a relationship in magnitude uncertainty (Δm) occurs:

$$\Delta m = -2.5 \, log_{10} \frac{F + \Delta F}{F} \tag{7.1}$$

$$\Delta m = -2.5 \, log_{10}(1 + \frac{\Delta F}{F})$$

Require Taylor series: $ln(1 + x) \underset{x \ll 1}{\approx} x$

$$-2.5 \, log_{10}(1 + \frac{\Delta F}{F}) = -2.5 \, \frac{ln\,(1 + \frac{\Delta F}{F})}{ln\,10} \tag{7.2}$$

(continued...)

$$-2.5 \, \frac{ln\left(1 + \frac{\Delta F}{F}\right)}{ln \, 10} = -\frac{2.5}{ln \, 10} \cdot \frac{\Delta F}{F} \tag{7.3}$$

$$-\frac{2.5}{ln \, 10} \cdot \frac{\Delta F}{F} \approx \frac{\Delta F}{F} \tag{7.4}$$

$$\frac{\Delta F}{F} \underset{\frac{\Delta F}{F} \ll 1}{\approx} \Delta m \tag{7.5}$$

My photometry software calculated both the one-pixel background corrected MSB of a feature and the one-pixel root-mean-square (RMS) background surface brightness. These two values act as the signal and noise of a feature respectively. I have analysed two variations of S/N. The first is the one square arcsecond S/N, which is the the ratio of the signal to noise multiplied by the square-root of the number of pixels required to fill one square arcsecond (25). The second is the S/N of the entire H_2 feature using the feature area. This is effectively the same as the first variation but the ratio is multiplied by the square-root of the number of pixels to fill one square arcsecond and then the feature area (in square arcseconds). For each of the features, the S/N's are calculated by:

$$S/N_{one \, arcsec} = \sqrt{25} \quad \times \quad \frac{\text{MSB}}{\text{RMS background surface brightness}} \tag{7.6}$$

$$S/N_{feature \, area} = \sqrt{25 \times \text{Area}} \quad \times \quad \frac{\text{MSB}}{\text{RMS background surface brightness}} \tag{7.7}$$

Figure 7.1 compares the median S/N (both variations) achieved at different locations along the Milky Way for the full catalogue of features. The median values are shown for every five degrees in Galactic longitude spanning from $355° < l < 360°$ and $0° < l < 155°$. The light, hatched bins represent the median S/N over one square arcsecond whilst the dark bins represent the median S/N over the area of an entire H_2 feature. From this figure we see that the median S/N value over one square arcsecond does not fluctuate a large amount as Galactic longitude increases. The median value for the entire catalogue is about 4.13 and the highest and lowest values from the figure are about 5.43 and 3.44 respectively. Comparing
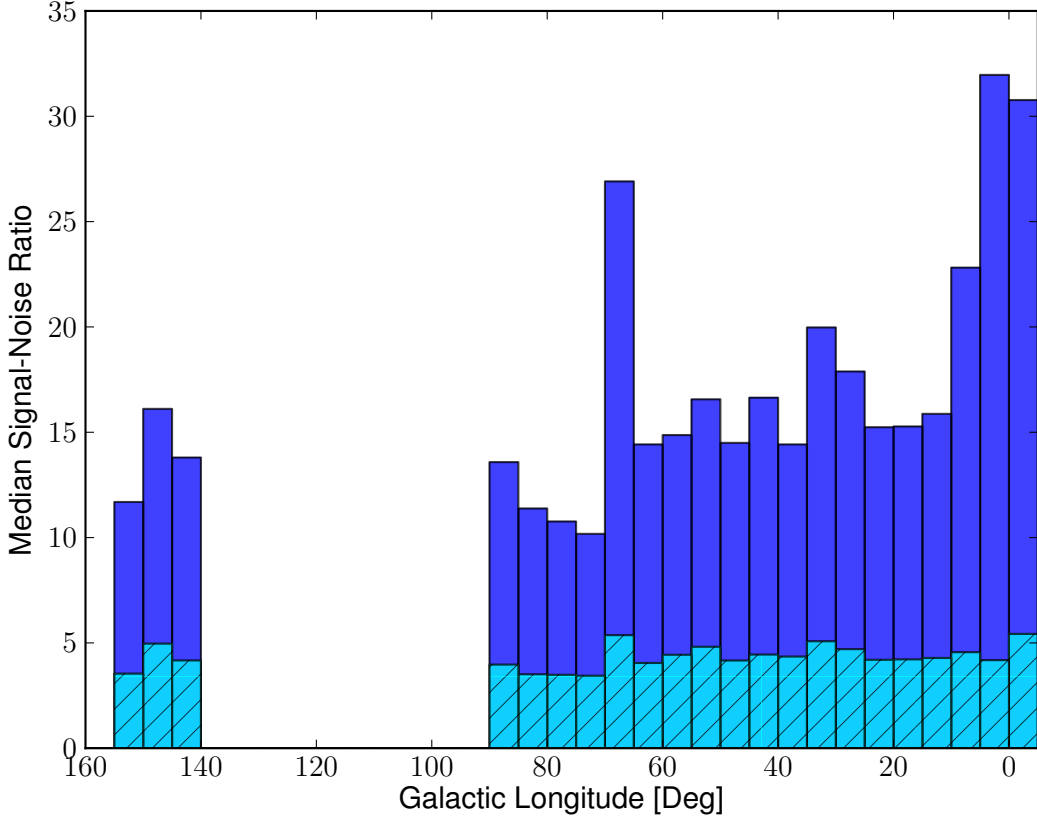
Figure 7.1: Histogram showing the median S/N for the one square arcsecond area (light, hatched) and whole H_2 feature area (dark, unhatched) of every feature in the UWISH2 catalogue. Median values are sampled for every five degrees of Galactic longitude starting from $355° < l < 360°$ and continuing to $0° < l < 155°$, covering the GP, Cygnus and Auriga. GP-Cygnus split occurs at $70°$ in this figure.

this to the median S/N when the entire area of the feature is taken into account, we see an expected increase in the median values, as all features are larger than one square arcsecond. We also see a greater change in the S/N, with much higher ratios occurring at low Galactic longitudes. This could be because a lot of the largest and brightest features occur at lower Galactic longitudes. Alternatively it could be due to there only being few features occupying the first few degrees of Galactic longitude. This idea is supported by features between $65° < l < 70°$, which produce a high median S/N whilst containing only 91 members. However, features between $355° < l < 360°$ produce a high median S/N with few members (178), and the adjacent features between $0° < l < 5°$ produce a similar median S/N from 741 members.

To further analyse, Figure 7.2 calculates the median S/N's of the individual types of H_2 feature within the same range of Galactic longitudes (except SNRs, which exist only in the GP). The panels, where top left to bottom right describe jets, PNe, PDRs and SNRs, all contain some similarities with in Figure 7.1. For medians S/N's from using the feature areas, there are some noticeable differences when compared to the one square arcesecond S/N. The one square arcsecond median S/N's remain at similar values across all Galactic longitudes, with little fluctuation. Hence the following shall look to compare how the median S/N values using feature area change with location only.

Jet Features

For the panel concerning jets, we see the majority of median values are above 20 whilst the highest ratios occurs in the same lower Galactic longitudes seen from the full catalogue in Figure 7.1 and are similar in value to one another. Therefore we observe less of a dip in median values as Galactic longitude increases. For a large fraction of jet features at $65° < l < 70°$, the noise is small relative to the rest of the jet catalogue which may contribute to the higher median ratio.

PN Features

For PNe, we see an extremely large median S/N value between $355° < l < 360°$. This is, on closer inspection, due to there being only four PNe features within this range which is far too low a number to be able to take an accurate median. Aside from this anomaly, the histogram resembles that of the full catalogue in Figure 7.1 with the exception of median ratios being slightly higher and the range $65° < l < 70°$ constituting the highest median value. This happens because there is only one PN feature in this range and it has a S/N of about 81.

PDR Features

The PDR panel shows large similarities with the full catalogue figure. This is likely due to the huge amount of PDR features in the catalogue making it plausible that all of the ranges will have a similar S/N. Only a couple of median values over the five degree ranges have changed a large amount compared to the full catalogue. An example of large change is $145° < l < 150°$ whose median S/N has dropped from about 16.11 to 7.24. However, in this range there are only 22 PDR features, a quarter of the features that exist here from the full catalogue, so the difference may stem from low numbers. It should also be noted that all PDR features in Auriga have undergone a reduction in the S/N compared to the full catalogue.

SNR Features

Features classed as SNRs also possess a similar histogram shape to the others, with high median values at low Galactic longitudes followed by a dip. The main difference is that the consistent peak in the median S/N at $65° < l < 70°$ seen in the other feature types is no longer there. The adjacent bin concerning the median S/N between $60° < l < 65°$ does contain a high value. This exchange is likely because these two ranges consist of three and four SNR features respectively, hence their values can be deemed very unreliable.
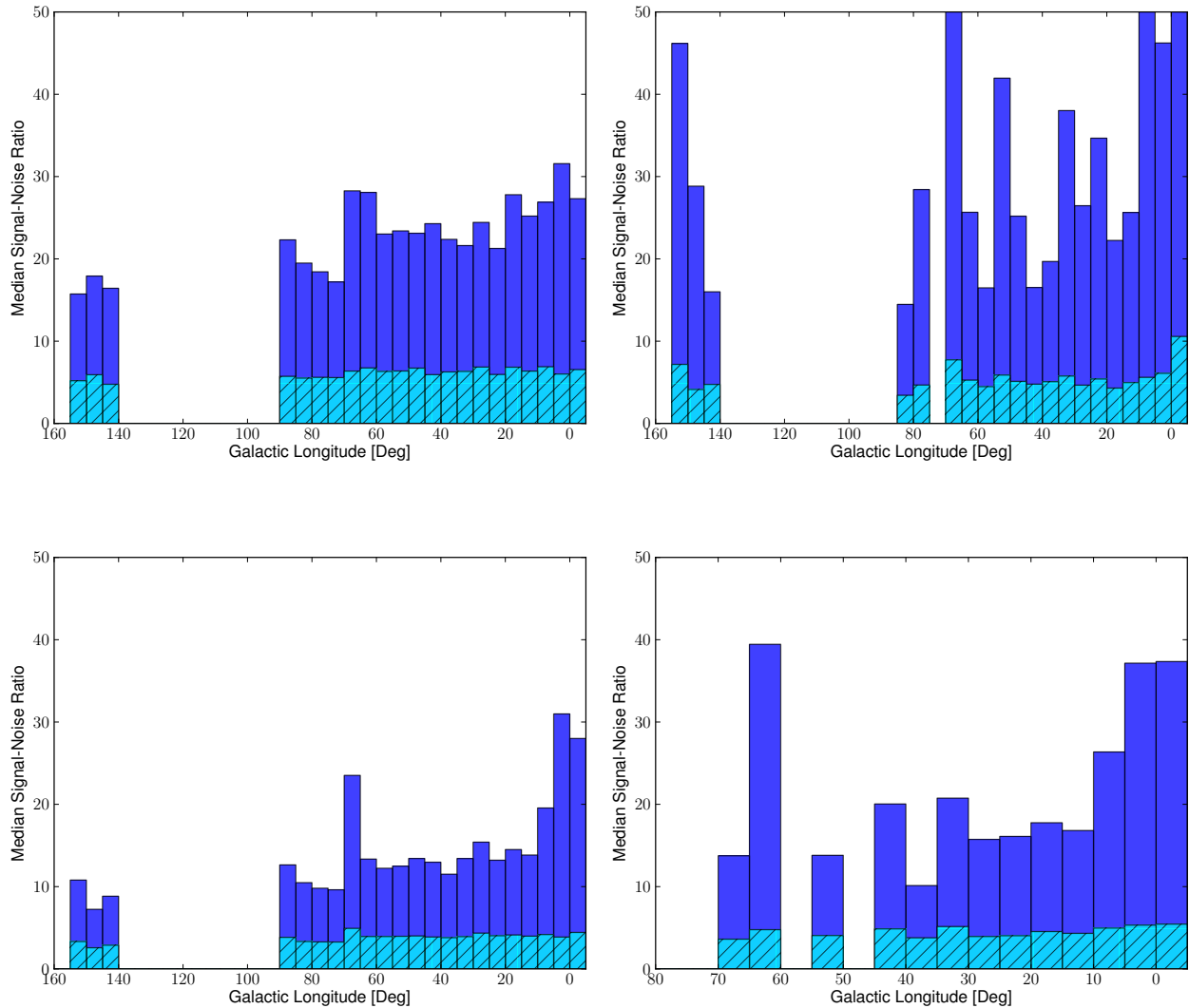
Figure 7.2: Histograms showing the median S/N for the one square arcsecond area (light, hatched) and whole H_2 feature area (dark, unhatched). The four panels from top left to bottom right display values for individual jet features, PNe features, PDR features and SNR features (not groups). Median values are sampled for every five degrees of Galactic longitude starting from $355° < l < 360°$ and continuing to $0° < l < 155°$, covering the GP, Cygnus and Auriga. GP-Cygnus split occurs at $70°$ in this figure. For the PNe figure, the bar heights that have been cut out from right to left are approximately: 177.1, 51.6 and 81.3.
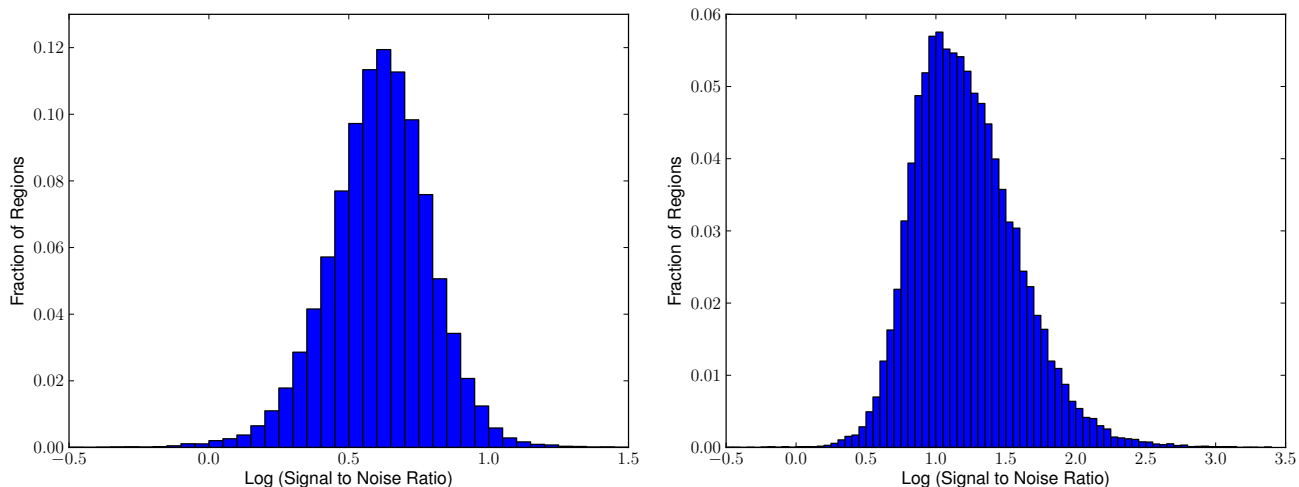
Figure 7.3: Histograms showing the relative fraction of the Log of the S/N values for H_2 features in the full catalogue. The left panel shows S/N values for one square arcsecond and the right panel shows S/N values using the feature areas. The x-axis limits have been set to include every single S/N value, which includes outliers.

7.2 Highest and Lowest Signal-to-noise Ratios

The median S/N of the entire survey is approximately 15.15 resulting in a flux uncertainty of 6.6% (for that particular feature). From the right panel of Figure 7.3, which describes the most common values of S/N, we see that the majority of S/N values over the entirety of a feature are between roughly 7 and 30, which translates to an flux uncertainty from anywhere between 14.3% to 3.3% for the majority of the features. Figure 7.4 shows the distribution of the one square arcsecond S/N values for all features. The red line indicates a S/N value of one, hence we can see that the vast majority of features have a S/N greater than unity.

For the one square arcsecond S/N, the smallest Log value is situated far from the main histogram body at -1.32 (translates to about 0.06). This is due to the PDR feature *UWISH2_016.86579+0.70140* from the image *w20100612_00321_y*, having a median surface brightness of $0.04W\ m^{-2}arcsec^{-2}$ and a background RMS of 3.33. Upon inspection, the small median surface brightness likely comes as a result of this feature residing inside another feature, which can be seen in the top panel of Figure 7.5. This would cause the median pixel values of the feature and its
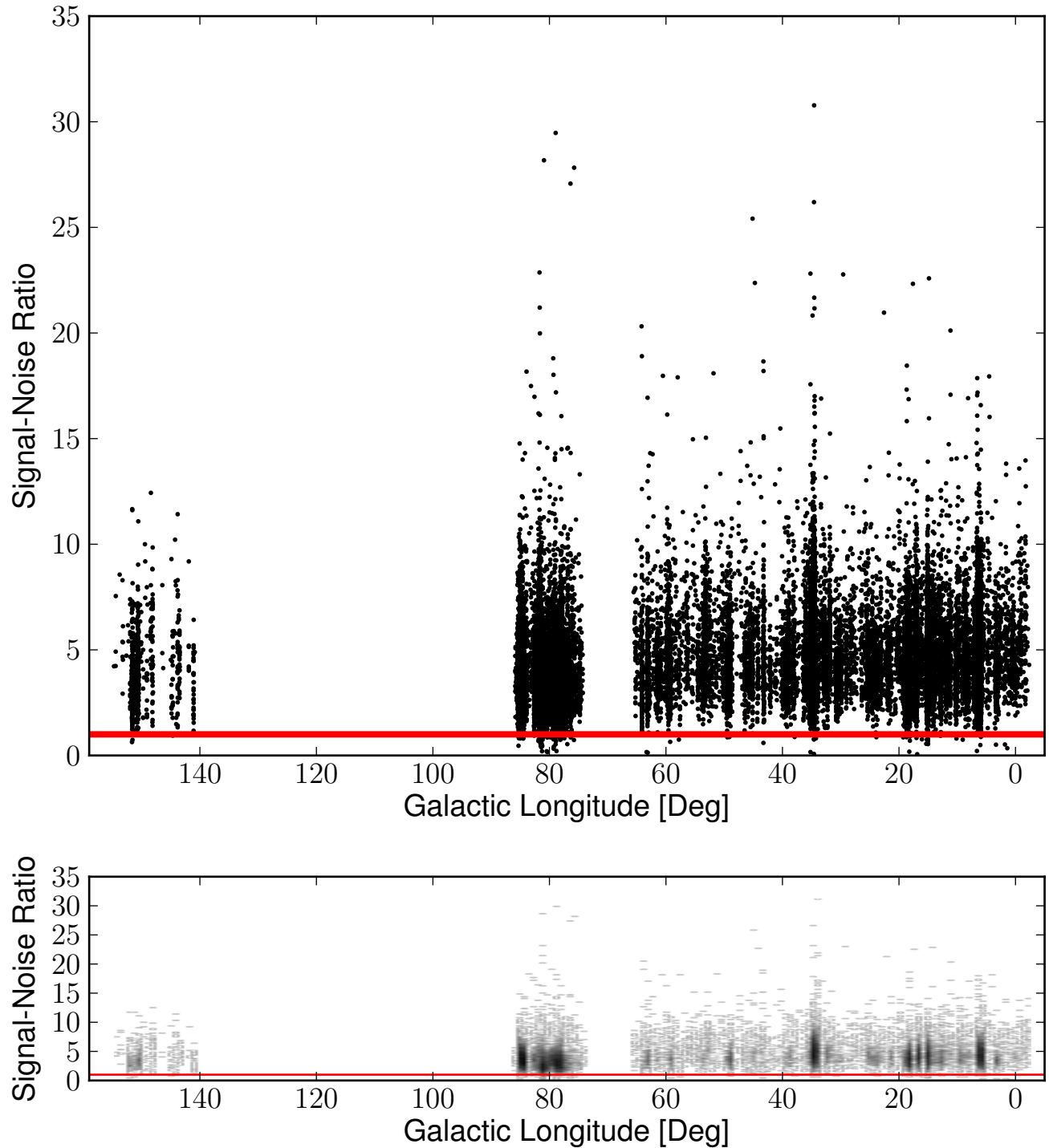
Figure 7.4: Both panels show the distribution of all S/N values across one square arcsecond for all individual features in the UWISH2 catalogue and their location in Galactic longitude. The red horizontal lines indicate S/N = 1 in both panels. The bottom panel is a density map where the gray scale indicates the Log of the density of objects in each position with the darker regions representing higher density of plots.

110

background to be very similar and results in the one-pixel background corrected median surface brightness being very low. The highest S/N Log value is about 1.49 (translates roughly to 30.77). It should be noted that I have not taken into account any features that possessed a negative median flux, which make up a very small fraction of the total number.

In contrast the Log of the smallest S/N value for a single feature, across its area, is about -0.72 (translates to 0.19). This is from the jet/outflow feature, *UWISH2_034.60081−1.02756* within image *w20110615_00666_y*. Like before, this feature has a very small median surface brightness of $0.06 W\,m^{-2}arcsec^{-2}$ and a high background RMS of 4.01. The Log of the largest S/N value for a single feature, across its area, is about 3.37 (translates to approximately 2.37×10^2). This comes from another PDR feature listed in the catalogue as *UWISH2_076.38789−0.61853* from the image *w20130604_00882_x*. This is due to a relatively large median surface brightness coupled with a very large area of almost 8×10^3 arcseconds. This feature is shown in the bottom panel of Figure 7.5.

The average seeing in our survey is 0.79" with 82.9% of the survey area having a seeing of less than 1" (Froebrich et al., 2015). Most of the areas with worse seeing are located in the additional regions of Cygnus and Auriga, which are less crowded than the lower Galactic longitudes of the GP so this is not a serious problem. Therefore, the seeing in UWISH2 is of a good standard and as the smallest of features are still very extended we do not expect poor seeing to have a detrimental effect on feature areas or fluxes and hence no effect on the S/N values.
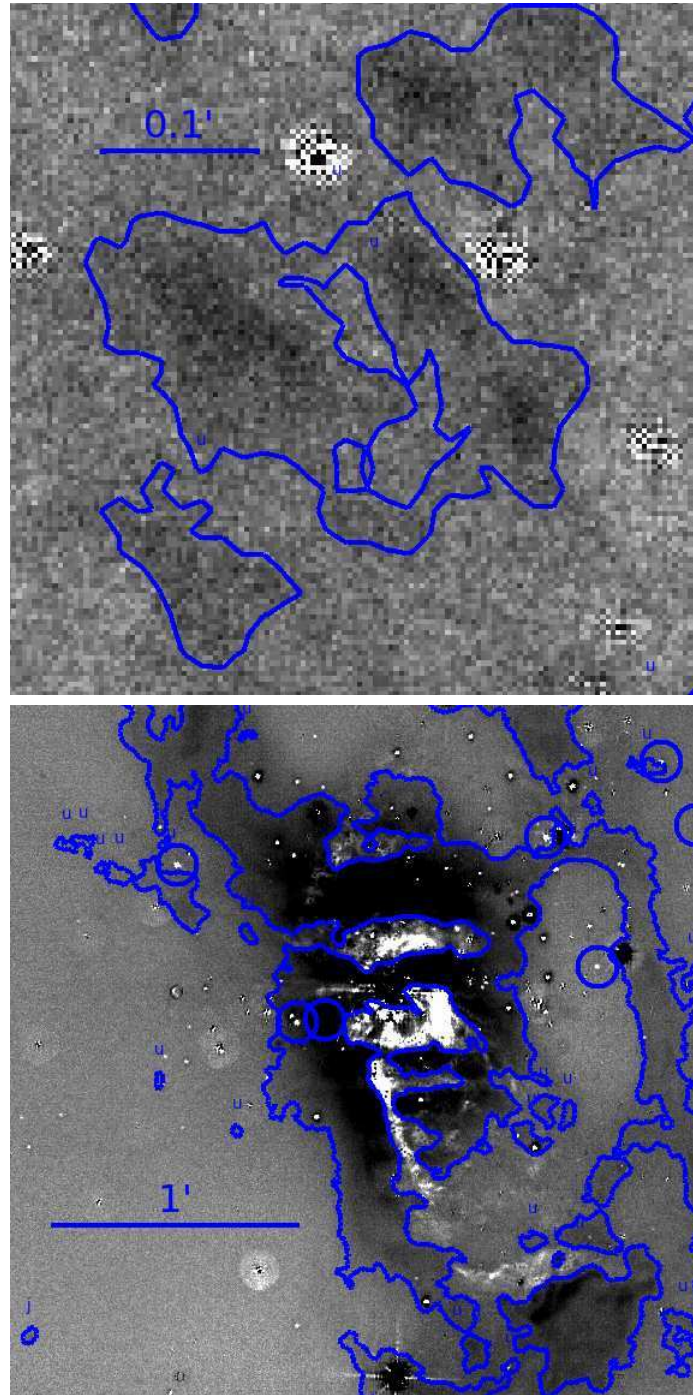
Figure 7.5: Top: The PDR feature *UWISH2_016.86579+0.70140* from the image *w20100612_00321_y* contained inside another feature. This has likely affected the median background corrected surface brightness leading to a poor S/N value. **Bottom:** The PDR feature *UWISH2_076.38789−0.61853* from the image *w20130604_00882_x*. It possesses the highest feature area S/N value in the survey due to high median surface brightness and being very extended.

Chapter 8

Future Work

There are currently ongoing efforts to identify possible candidate driving sources of the jets/outflows in the survey. This has proven difficult so far because star forming regions are crowded with a variety of jet features with different orientations and possible sources. Outflows from YSOs can be bipolar. Alternatively, only one of the outflows may be visible due to the other being obscured by dust. Emission could even appear random and non-jet-like. There are also cases of isolated jet features with no visible orientations. In cases such as this, there is difficulty encountered in verifying whether the feature is actually an outflow, before the difficulty of trying to pair the isolated emission with a driving source. Attempts to 'decrypt' the collection of H_2 jets in Cygnus are being carried out and results will soon be investigated by Makin and Froebrich (in prep). Additionally, the same efforts are currently ongoing for Auriga and result will be made available by Froebrich and Makin (in prep). There is a level of uncertainty associated with each outflow-YSO assignment. This uncertainty will be taken into account and each assignment will carry a probability that it is correctly paired. Examples of measurements to be made after the assignment of the source include the the location of the likely source, the number of outflows (bipolar, single), the lengths and orientations of each outflow, the GPS magnitudes (where entries exist) and the brightness of outflow emission, adapted from my work.

With the large number of PNe candidates that UWISH2 has discovered, there are

efforts to confirm the PNe status of the candidates and investigate their properties. The work is ongoing and the results will be prepared by Gledhill et al. (in prep). Further study of the SNRs in UWISH2 is being conducted by Lee et al. (in prep). The photometry code will be used to process the fluxes of features in the sister survey of UWISH2 called the UKIRT Widefield Infrared Survey for Fe^+ (UWIFE, Lee et al. (2014)), which uses a narrowband filter centred on the [FeII] $1.644\,\mu m$ emission line. The results of this survey will be presented by Lee at al. (in prep).

Chapter 9

Conclusions

WFCAM at UKIRT has been used to conduct a large, narrowband, unbiased survey of extended H_2 emission, using the 1–0 S(1) emission line at $2.122\,\mu m$. This has been done for regions of the GP and high column density regions in Cygnus and Auriga. The coverage of the GP was near homogeneous, covering 209 square degrees between $l \approx 357°$ to $l \approx 66°$ and $b \approx \pm 1.5°$. The coverage of Cygnus and Auriga was non-homogeneous due to the targeting of high column density regions. Approximately 42 square degrees of Cygnus were observed whilst approximately 35.5 square degrees were observed in Auriga. Various high column density regions were imaged between $l \approx 74°$ to $l \approx 86°$ and $b \approx -3°$ to $b \approx 5°$ for Cygnus and $l \approx 357°$ to $l \approx 66°$ and $b \approx -4°$ to $b \approx 2.5°$ for Auriga.

The survey consists of 367 tiles, each containing 16 images from the micro-stepping procedure, leading to 5872 different images. Out of all the images, approximately one third contained some extended H_2 emission features. In total, the UWISH2 catalogue contains 33200 real H_2 emission features, separated into their different types – jets/outflows(3558), PNe(796), SNRs(5630) and PDRs(23216). In most cases, several H_2 features were fragments of a larger object or group. Individual features were grouped to form either a single star forming region in the case of jets and PDRs or a single PN or SNR. The result of this is that we have 711 jet/outflow groups and 1309 PDR groups in the survey plus 284 PNe and 30 SNRs. Due to the grouping process, the numbers of jet/outflow and PDR groups are liable to fluctu-

ate if grouping specifications alter by small amounts. Hence I will conclude that there are approximately 700 and 1300 jet and PDR groups respectively. Grouping of the PNe and SNRs was more scrutinous and the final numbers are unlikely to change.

I have written a program that performed the photometry of these features. The output of my program was responsible for the following properties in the UWISH2 catalogue:

i) Area of the emission in square arcseconds. The number of pixels inside the feature were counted and multiplied by the 0.04 square arcseconds area per pixel.

ii) Feature radius in arcseconds. This is the radius of a circle that can encapsulate the entire feature.

iii) Median background corrected surface brightness in $10^{-19} \, W m^{-2} \, arcsec^{-2}$. It forms a reliable method of photometry when multiplied by the feature area as it will filter features with erroneous fluxes due to residual stars that can influence the flux.

iv) Peak surface brightness in $10^{-19} \, W m^{-2} \, arcsec^{-2}$: is the highest one-pixel surface brightness in the feature.

v) Total flux in $10^{-19} \, W m^{-2}$: is the sum of all pixel intensities in the feature and a form of photometry that is effective if there are no stars in the feature.

vi) 1-pixel RMS noise surface brightness in $10^{-19} \, W m^{-2} \, arcsec^{-2}$: is the one σ RMS of the pixel values in background ring after sigma clipping to remove bright or dark aberrations.

I have found that the majority of the H_2 flux is contained in PDR and SNR features, with approximately 43.6% of flux coming from PDR features and about 40.4% coming from SNR features. Jet and PNe features contain about 9.3% and 6.7% of the H_2 flux respectively. This is probably due in part to SNR features

being very extended and there being a very large number of PDR features, as total flux often scales with the area of emission.

I find that for jets and PDRs, the majority of groups occur at low Galactic longitudes ($l < 20°$) which is indicative of higher star formation activity occurring close to the Galactic Centre. I then find that the total flux and number of features declines as the Galactic longitude increases. Based on the survey coverage, there were typically more jet and PDR features, and a higher total flux than expected at low Galactic longitudes and less than expected at higher Galactic longitudes of the GP. At some higher Galactic longitudes in the GP, large amounts of jet flux have been observed, but there are almost no bright PDRs. This indicates that low mass star formation is favourable at these locations and that the bulk of higher mass stars that produce the FUV and EUV radiation responsible for PDRs and Hɪɪ regions are at the lower Galactic longitudes. There is also an abundance of jets and PDRs in Cygnus, where the highest number and flux density of jets and PDRs occur. The high density of features is likely due to the survey bias associated with Cygnus, but an unbiased survey would still likely indicate high star formation activity based on the total flux alone. Auriga received the same survey bias and remains quiescent relative to the number density of features and total fluxes of Cygnus and the GP, indicating low star formation activity.

Of the 284 PNe detected, 167 are newly discovered candidates which are likely young or embedded (or both). A further 32 have been listed in previous literature as a different type of object. About 45% of the entire PNe H_2 flux is from PN G017.6-01.1. About 92% of UWISH2 PNe are contained in the GP.

Of all the known SNRs that exist in the area covered by WFCAM, about one quarter had detectable H_2 emission. Whilst they make up about 40.4% of the total flux of the survey, two SNRs (W 28 and W 44) combined make up about 83.5% of the total SNR flux.

I compared the agreement of total-flux photometry and median MSB-photometry (or the MSB flux). I found varying amounts of change in flux when switching between the photometry methods. On a large scale, comparing the change in flux

of both photometries per degree of Galactic longitude for the GP and Cygnus, I found there were mostly small changes in between a small fraction of larger changes. Some of the extreme individual changes include jet group DR 21, which would lose 25% of its flux if the MSB flux was used, whilst the aforementioned PN G017.6-01.1 has about four times as much total flux as it does MSB flux. Overall, I found that about 97% of features in the entire survey have a total – MSB flux ratio between 2 and 0.5 (100% deviation) and 82% are within a 20% deviation. The majority of PNe, SNR and PDR features showed good agreement, with the majority of features within a 100% deviation and a large fraction within the 20% deviation desired for an excellent agreement. Because of this, I advise that the MSB flux should be used for any of the PNe, SNR or PDR features because of a high agreement with the total flux and the potential to remove unsubtracted or variable stars. For jet/outflow features, there was a good photometry agreement within a 100% deviation but only about 64% of features agreed within a 20% deviation. It is best to use the total flux for jet features, but if a specific star forming region is of interest, photometry should be re-run by the reader in order to guarantee no stars are included.

I have calculated the one square arcsecond signal-to-noise ratio as well as the signal-to-noise ratio using the feature area. I found that in the latter, features have a broad range of values. By taking the median signal-to-noise ratio occurring every five degrees of Galactic longitude, I can conclude that the ratios are typically higher toward the Galactic Centre. The vast majority of features have a signal-to-noise ratio greater than unity and the median value (using area) for the full catalogue of features is approximately 15.

Bibliography

Isabel Aleman and Ruth Gruenwald. Molecular hydrogen in the ionized region of planetary nebulae. *The Astrophysical Journal*, 607(2):865, 2004. URL `http://stacks.iop.org/0004-637X/607/i=2/a=865`.

L. D. Anderson, T. M. Bania, J. M. Jackson, D. P. Clemens, M. Heyer, R. Simon, R. Y. Shah, and J. M. Rathborne. The Molecular Properties of Galactic H II Regions. *Astrophysical Journal, Supplement*, 181:255–271, March 2009. doi: 10.1088/0067-0049/181/1/255.

P. André, S. Basu, and S. Inutsuka. *The formation and evolution of prestellar cores*, page 254. Cambridge University Press, January 2009.

I. Appenzeller and W. Tscharnuter. On the luminosity of spherical protostars. *Astronomy and Astrophysics*, 40:397–399, May 1975.

M. Beech and R. Mitalas. Formation and evolution of massive stars. *Astrophysical Journal, Supplement*, 95:517–534, December 1994. doi: 10.1086/192109.

H. Beuther and D. Shepherd. Precursors of UCHII Regions and the Evolution of Massive Outflows. In M. S. N. Kumar, M. Tafalla, and P. Caselli, editors, *Cores to Clusters: Star Formation with Next Generation Telescopes*, pages 105–119, November 2005.

I. A. Bonnell, M. R. Bate, and H. Zinnecker. On the formation of massive stars. *Monthly Notices of the RAS*, 298:93–102, July 1998. doi: 10.1046/j.1365-8711.1998.01590.x.

E. Cappellaro and M. Turatto. Supernova Types and Rates. In D. Vanbeveren, editor, *The Influence of Binaries on Stellar Population Studies*, volume 264 of *Astrophysics and Space Science Library*, page 199, 2001. doi: 10.1007/978-94-015-9723-4_16.

M. Casali, A. Adamson, C. Alves de Oliveira, O. Almaini, K. Burch, T. Chuter, J. Elliot, M. Folger, S. Foucaud, N. Hambly, M. Hastie, D. Henry, P. Hirst, M. Irwin, D. Ives, A. Lawrence, K. Laidlaw, D. Lee, J. Lewis, D. Lunney, S. McLay, D. Montgomery, A. Pickup, M. Read, N. Rees, I. Robson, K. Sekiguchi, A. Vick, S. Warren, and B. Woodward. The UKIRT wide-field camera. *Astronomy and Astrophysics*, 467:777–784, May 2007. doi: 10.1051/0004-6361:20066514.

R. Cesaroni. Outflow, Infall, and Rotation in High-Mass Star Forming Regions. *Astrophysics and Space Science*, 295:5–17, January 2005. doi: 10.1007/s10509-005-3651-8.

S. Chandrasekhar. The Maximum Mass of Ideal White Dwarfs. *Astrophysical Journal*, 74:81, July 1931. doi: 10.1086/143324.

S. Chandrasekhar. The highly collapsed configurations of a stellar mass (Second paper). *Monthly Notices of the RAS*, 95:207–225, January 1935.

M. Cohen, W. A. Wheaton, and S. T. Megeath. Spectral Irradiance Calibration in the Infrared. XIV. The Absolute Calibration of 2MASS. *Astronomical Journal*, 126:1090–1096, August 2003. doi: 10.1086/376474.

R. M. Crutcher. Magnetic Fields in Molecular Clouds: Observations Confront Theory. *Astrophysical Journal*, 520:706–713, August 1999. doi: 10.1086/307483.

R. M. Crutcher, N. Hakobian, and T. H. Troland. Testing Magnetic Star Formation Theory. *Astrophysical Journal*, 692:844–855, February 2009. doi: 10.1088/0004-637X/692/1/844.

A. Cunningham, A. Frank, and L. Hartmann. Wide-Angle Wind-driven Bipolar Outflows: High-Resolution Models with Application to Source I of the Becklin-

Neugebauer/Kleinmann-Low OMC-I Region. *Astrophysical Journal*, 631:1010–1021, October 2005. doi: 10.1086/432658.

C. J. Davis, M. S. N. Kumar, G. Sandell, D. Froebrich, M. D. Smith, and M. J. Currie. WFCAM, Spitzer/IRAC and SCUBA observations of the massive star-forming region DR21/W75 - I. The collimated molecular jets. *Monthly Notices of the RAS*, 374:29–53, January 2007. doi: 10.1111/j.1365-2966.2006.11163.x.

C. J. Davis, P. Scholz, P. Lucas, M. D. Smith, and A. Adamson. A shallow though extensive H_2 2.122-μm imaging survey of Taurus-Auriga-Perseus - I. NGC 1333, L1455, L1448 and B1. *Monthly Notices of the RAS*, 387:954–968, July 2008. doi: 10.1111/j.1365-2966.2008.13247.x.

C. J. Davis, D. Froebrich, T. Stanke, S. T. Megeath, M. S. N. Kumar, A. Adamson, J. Eislöffel, R. Gredel, T. Khanzadyan, P. Lucas, M. D. Smith, and W. P. Varricatt. A census of molecular hydrogen outflows and their sources along the Orion A molecular ridge. Characteristics and overall distribution. *Astronomy and Astrophysics*, 496:153–176, March 2009. doi: 10.1051/0004-6361:200811096.

G. Delamarter, A. Frank, and L. Hartmann. Interaction of Infall and Winds in Young Stellar Objects. *Astrophysical Journal*, 530:923–938, February 2000. doi: 10.1086/308389.

S. Dye, S. J. Warren, N. C. Hambly, N. J. G. Cross, S. T. Hodgkin, M. J. Irwin, A. Lawrence, A. J. Adamson, O. Almaini, A. C. Edge, P. Hirst, R. F. Jameson, P. W. Lucas, C. van Breukelen, J. Bryant, M. Casali, R. S. Collins, G. B. Dalton, J. I. Davies, C. J. Davis, J. P. Emerson, D. W. Evans, S. Foucaud, E. A. Gonzales-Solares, P. C. Hewett, T. R. Kendall, T. H. Kerr, S. K. Leggett, N. Lodieu, J. Loveday, J. R. Lewis, R. G. Mann, R. G. McMahon, D. J. Mortlock, Y. Nakajima, D. J. Pinfield, M. G. Rawlings, M. A. Read, M. Riello, K. Sekiguchi, A. J. Smith, E. T. W. Sutorius, W. Varricatt, N. A. Walton, and S. J. Weatherley. The UKIRT Infrared Deep Sky Survey Early

Data Release. *Monthly Notices of the RAS*, 372:1227–1252, November 2006. doi: 10.1111/j.1365-2966.2006.10928.x.

G. B. Field, W. B. Somerville, and K. Dressler. Hydrogen Molecules in Astronomy. *Annual Review of Astron and Astrophysics*, 4:207, 1966. doi: 10.1146/annurev. aa.04.090166.001231.

J. Franco, S. Kurtz, and G. García-Segura. The Interstellar Medium and Star Formation: The Impact of Massive Stars (With 12 Figures). In R. E. Schielicke, editor, *Reviews in Modern Astronomy*, volume 16 of *Reviews in Modern Astronomy*, page 85, 2003.

A. Frankowski and N. Soker. Very late thermal pulses influenced by accretion in planetary nebulae. *New Astronomy*, 14:654–658, November 2009. doi: 10.1016/ j.newast.2009.03.006.

D. J. Frew and Q. A. Parker. Planetary Nebulae: Observational Properties, Mimics and Diagnostics. *Publications of the Astronomical Society of Australia*, 27:129–148, May 2010. doi: 10.1071/AS09040.

D. Froebrich, C. J. Davis, G. Ioannidis, T. M. Gledhill, M. Takami, A. Chrysostomou, J. Drew, J. Eislöffel, A. Gosling, R. Gredel, J. Hatchell, K. W. Hodapp, M. S. N. Kumar, P. W. Lucas, H. Matthews, M. G. Rawlings, M. D. Smith, B. Stecklum, W. P. Varricatt, H. T. Lee, P. S. Teixeira, C. Aspin, T. Khanzadyan, J. Karr, H.-J. Kim, B.-C. Koo, J. J. Lee, Y.-H. Lee, T. Y. Magakian, T. A. Movsessian, E. H. Nikogossian, T. S. Pyo, and T. Stanke. UWISH2 - the UKIRT Widefield Infrared Survey for H_2. *Monthly Notices of the RAS*, 413: 480–492, May 2011. doi: 10.1111/j.1365-2966.2010.18149.x.

D. Froebrich, S. V. Makin, C. J. Davis, T. M. Gledhill, Y. Kim, B.-C. Koo, J. Rowles, J. Eislöffel, J. Nicholas, J. J. Lee, J. Williamson, and A. S. M. Buckner. Extended H_2 emission line sources from UWISH2. *Monthly Notices of the RAS*, 454:2586–2605, December 2015. doi: 10.1093/mnras/stv1729.

T. A. Gardiner, A. Frank, and L. Hartmann. Stellar Outflows Driven by Magnetized Wide-Angle Winds. *Astrophysical Journal*, 582:269–276, January 2003. doi: 10.1086/344609.

L. Georgiev, C. Morisset, and J. Zsargó. Can stellar rotation shape the planetary nebulae? In *Revista Mexicana de Astronomia y Astrofisica Conference Series*, volume 40 of *Revista Mexicana de Astronomia y Astrofisica, vol. 27*, pages 203–203, October 2011.

T. M. Gledhill and K. P. Forde. Imaging the transition between pre-planetary and planetary nebulae: integral field spectroscopy of hot post-AGB stars with NIFS. *Monthly Notices of the RAS*, 447:1080–1095, February 2015. doi: 10.1093/mnras/stu2493.

D. A. Green. A revised Galactic supernova remnant catalogue. *Bulletin of the Astronomical Society of India*, 37:45–61, March 2009.

D. A. Green. A catalogue of 294 Galactic supernova remnants. *Bulletin of the Astronomical Society of India*, 42:47–58, June 2014.

P. C. Hewett, S. J. Warren, S. K. Leggett, and S. T. Hodgkin. The UKIRT Infrared Deep Sky Survey ZY JHK photometric system: passbands and synthetic colours. *Monthly Notices of the RAS*, 367:454–468, April 2006. doi: 10.1111/j.1365-2966.2005.09969.x.

S. T. Hodgkin, M. J. Irwin, P. C. Hewett, and S. J. Warren. The UKIRT wide field camera ZYJHK photometric system: calibration from 2MASS. *Monthly Notices of the RAS*, 394:675–692, April 2009. doi: 10.1111/j.1365-2966.2008.14387.x.

D. J. Hollenbach and A. G. G. M. Tielens. Dense Photodissociation Regions (PDRs). *Annual Review of Astron and Astrophysics*, 35:179–216, 1997. doi: 10.1146/annurev.astro.35.1.179.

D. J. Hollenbach and A. G. G. M. Tielens. Photodissociation regions in the interstellar medium of galaxies. *Reviews of Modern Physics*, 71:173–230, January 1999. doi: 10.1103/RevModPhys.71.173.

D. J. Hollenbach, M. W. Werner, and E. E. Salpeter. Molecular Hydrogen in H i Regions. *Astrophysical Journal*, 163:165, January 1971. doi: 10.1086/150755.

G. Ioannidis and D. Froebrich. YSO jets in the Galactic plane from UWISH2 - I. MHO catalogue for Serpens and Aquila. *Monthly Notices of the RAS*, 421: 3257–3265, April 2012a. doi: 10.1111/j.1365-2966.2012.20550.x.

G. Ioannidis and D. Froebrich. YSO jets in the Galactic plane from UWISH2 - II. Outflow luminosity and length distributions in Serpens and Aquila. *Monthly Notices of the RAS*, 425:1380–1393, September 2012b. doi: 10.1111/j.1365-2966. 2012.21556.x.

P. A. Jaminet, W. C. Danchi, E. C. Sutton, J. H. Bieging, D. Wilner, A. P. G. Russell, and G. Sandell. CO J = 3-2 and J = 2-1 observations of NGC 7027. *Astrophysical Journal*, 380:461–475, October 1991. doi: 10.1086/170604.

J. H. Jeans. The Stability of a Spherical Nebula. *Philosophical Transactions of the Royal Society of London Series A*, 199:1–53, 1902. doi: 10.1098/rsta.1902.0012.

H.-J. Kim, B.-C. Koo, and C. J. Davis. Active Star Formation in the Long Infrared Dark Cloud G53.2. *IAU General Assembly*, 22:56867, August 2015.

R. S. Klessen. Star Formation in Molecular Clouds. In C. Charbonnel and T. Montmerle, editors, *EAS Publications Series*, volume 51 of *EAS Publications Series*, pages 133–167, November 2011. doi: 10.1051/eas/1151009.

R. S. Klessen, F. Heitsch, and M.-M. Mac Low. Gravitational Collapse in Turbulent Molecular Clouds. I. Gasdynamical Turbulence. *Astrophysical Journal*, 535:887–906, June 2000. doi: 10.1086/308891.

A. Konigl and R. E. Pudritz. Disk Winds and the Accretion-Outflow Connection. *Protostars and Planets IV*, page 759, May 2000.

M. R. Krumholz and C. F. McKee. A General Theory of Turbulence-regulated Star Formation, from Spirals to Ultraluminous Infrared Galaxies. *Astrophysical Journal*, 630:250–268, September 2005. doi: 10.1086/431734.

R. B. Larson. Turbulence and star formation in molecular clouds. *Monthly Notices of the RAS*, 194:809–826, March 1981.

R. B. Larson. Cloud fragmentation and stellar masses. *Monthly Notices of the RAS*, 214:379–398, June 1985.

R. B. Larson. The physics of star formation. *Reports on Progress in Physics*, 66: 1651–1697, October 2003. doi: 10.1088/0034-4885/66/10/R03.

A. Lawrence, S. J. Warren, O. Almaini, A. C. Edge, N. C. Hambly, R. F. Jameson, P. Lucas, M. Casali, A. Adamson, S. Dye, J. P. Emerson, S. Foucaud, P. Hewett, P. Hirst, S. T. Hodgkin, M. J. Irwin, N. Lodieu, R. G. McMahon, C. Simpson, I. Smail, D. Mortlock, and M. Folger. The UKIRT Infrared Deep Sky Survey (UKIDSS). *Monthly Notices of the RAS*, 379:1599–1617, August 2007. doi: 10.1111/j.1365-2966.2007.12040.x.

J.-J. Lee, B.-C. Koo, Y.-H. Lee, H.-G. Lee, J.-H. Shinn, H.-J. Kim, Y. Kim, T.-S. Pyo, D.-S. Moon, S.-C. Yoon, M.-Y. Chun, D. Froebrich, C. J. Davis, W. P. Varricatt, J. Kyeong, N. Hwang, B.-G. Park, M. G. Lee, H. M. Lee, and M. Ishiguro. UKIRT Widefield Infrared Survey for Fe^+. *Monthly Notices of the RAS*, 443: 2650–2660, September 2014. doi: 10.1093/mnras/stu1146.

C. Low and D. Lynden-Bell. The minimum Jeans mass or when fragmentation must stop. *Monthly Notices of the RAS*, 176:367–390, August 1976. doi: 10. 1093/mnras/176.2.367.

P. W. Lucas, M. G. Hoare, A. Longmore, A. C. Schröder, C. J. Davis, A. Adamson, R. M. Bandyopadhyay, R. de Grijs, M. Smith, A. Gosling, S. Mitchison, A. Gáspár, M. Coe, M. Tamura, Q. Parker, M. Irwin, N. Hambly, J. Bryant, R. S. Collins, N. Cross, D. W. Evans, E. Gonzalez-Solares, S. Hodgkin, J. Lewis,

M. Read, M. Riello, E. T. W. Sutorius, A. Lawrence, J. E. Drew, S. Dye, and M. A. Thompson. The UKIDSS Galactic Plane Survey. *Monthly Notices of the RAS*, 391:136–163, November 2008. doi: 10.1111/j.1365-2966.2008.13924.x.

M. N. Machida, S.-i. Inutsuka, and T. Matsumoto. Driving Mechanism of Jets and Outflows in Star Formation Process. *ArXiv e-prints*, May 2007.

A. Maeder and R. Behrend. Formation and pre-MS Evolution of Massive Stars with Growing Accretion. In P. Crowther, editor, *Hot Star Workshop III: The Earliest Phases of Massive Star Birth*, volume 267 of *Astronomical Society of the Pacific Conference Series*, page 179, October 2002.

H. Masunaga and S.-i. Inutsuka. A Radiation Hydrodynamic Model for Protostellar Collapse. II. The Second Collapse and the Birth of a Protostar. *Astrophysical Journal*, 531:350–365, March 2000. doi: 10.1086/308439.

J. S. Mathis. Interstellar dust and extinction. *Annual Review of Astron and Astrophysics*, 28:37–70, 1990. doi: 10.1146/annurev.aa.28.090190.000345.

B. Miszalski, Q. A. Parker, A. Acker, J. L. Birkby, D. J. Frew, and A. Kovacevic. MASH-II: more planetary nebulae from the AAO/UKST Hα survey. *Monthly Notices of the RAS*, 384:525–534, February 2008. doi: 10.1111/j.1365-2966.2007. 12727.x.

T. C. Mouschovias and E. V. Paleologou. The angular momentum problem and magnetic braking - an exact time-dependent solution. *Astrophysical Journal*, 230:204–222, May 1979. doi: 10.1086/157077.

P. Padoan, Å. Nordlund, A. G. Kritsuk, M. L. Norman, and P. S. Li. Two Regimes of Turbulent Fragmentation and the Stellar Initial Mass Function from Primordial to Present-Day Star Formation. *Astrophysical Journal*, 661:972–981, June 2007. doi: 10.1086/516623.

F. Palla and S. W. Stahler. The Pre-Main-Sequence Evolution of Intermediate-Mass Stars. *Astrophysical Journal*, 418:414, November 1993. doi: 10.1086/173402.

Q. A. Parker, A. Acker, D. J. Frew, M. Hartley, A. E. J. Peyaud, F. Ochsenbein, S. Phillipps, D. Russeil, S. F. Beaulieu, M. Cohen, J. Köppen, B. Miszalski, D. H. Morgan, R. A. H. Morris, M. J. Pierce, and A. E. Vaughan. The Macquarie/AAO/Strasbourg Hα Planetary Nebula Catalogue: MASH. *Monthly Notices of the RAS*, 373:79–94, November 2006. doi: 10.1111/j.1365-2966.2006.10950.x.

R. E. Pudritz, M. J. Hardcastle, and D. C. Gabuzda. Magnetic Fields in Astrophysical Jets: From Launch to Termination. *Space Science Reviews*, 169:27–72, September 2012. doi: 10.1007/s11214-012-9895-z.

B. Reipurth. Disintegrating Multiple Systems in Early Stellar Evolution. *Astronomical Journal*, 120:3177–3191, December 2000. doi: 10.1086/316865.

E. W. Rosolowsky, J. E. Pineda, J. Kauffmann, and A. A. Goodman. Structural Analysis of Molecular Clouds: Dendrograms. *Astrophysical Journal*, 679:1338–1351, June 2008. doi: 10.1086/587685.

L. Sabin, Q. A. Parker, R. L. M. Corradi, L. Guzman-Ramirez, R. A. H. Morris, A. A. Zijlstra, I. S. Bojičić, D. J. Frew, M. Guerrero, M. Stupar, M. J. Barlow, F. C. Mora, J. E. Drew, R. Greimel, P. Groot, J. M. Irwin, M. J. Irwin, A. Mampaso, B. Miszalski, L. Olguín, S. Phillipps, M. S. García, K. Viironen, and N. J. Wright. First release of the IPHAS catalogue of new extended planetary nebulae. *Monthly Notices of the RAS*, 443:3388–3401, October 2014. doi: 10.1093/mnras/stu1404.

D. J. Schlegel, D. P. Finkbeiner, and M. Davis. Maps of Dust Infrared Emission for Use in Estimation of Reddening and Cosmic Microwave Background Radiation Foregrounds. *Astrophysical Journal*, 500:525–553, June 1998. doi: 10.1086/305772.

L. I. Sedov. *Similarity and Dimensional Methods in Mechanics.* 1959.

D. Seifried, R. Banerjee, R. S. Klessen, D. Duffin, and R. E. Pudritz. Magnetically Driven Outflows During Massive Star Formation. In R. Capuzzo-Dolcetta,

M. Limongi, and A. Tornambè, editors, *Advances in Computational Astrophysics: Methods, Tools, and Outcome*, volume 453 of *Astronomical Society of the Pacific Conference Series*, page 391, July 2012.

R. A. Shaw. Shape, structure, and morphology in planetary nebulae. In *IAU Symposium*, volume 283 of *IAU Symposium*, pages 156–163, August 2012. doi: 10.1017/S1743921312010873.

F. H. Shu and H. Shang. Protostellar X-rays, Jets, and Bipolar Outflows. In B. Reipurth and C. Bertout, editors, *Herbig-Haro Flows and the Birth of Stars*, volume 182 of *IAU Symposium*, pages 225–239, 1997.

F. H. Shu, F. C. Adams, and S. Lizano. Star formation in molecular clouds - Observation and theory. *Annual Review of Astron and Astrophysics*, 25:23–81, 1987. doi: 10.1146/annurev.aa.25.090187.000323.

M. F. Skrutskie, R. M. Cutri, R. Stiening, M. D. Weinberg, S. Schneider, J. M. Carpenter, C. Beichman, R. Capps, T. Chester, J. Elias, J. Huchra, J. Liebert, C. Lonsdale, D. G. Monet, S. Price, P. Seitzer, T. Jarrett, J. D. Kirkpatrick, J. E. Gizis, E. Howard, T. Evans, J. Fowler, L. Fullmer, R. Hurt, R. Light, E. L. Kopan, K. A. Marsh, H. L. McCallon, R. Tam, S. Van Dyk, and S. Wheelock. The Two Micron All Sky Survey (2MASS). *Astronomical Journal*, 131:1163–1183, February 2006. doi: 10.1086/498708.

P. M. Solomon, A. R. Rivolo, J. Barrett, and A. Yahil. Mass, luminosity, and line width relations of Galactic molecular clouds. *Astrophysical Journal*, 319: 730–741, August 1987. doi: 10.1086/165493.

D. Stamatellos. The Formation of Low-Mass Stars and Brown Dwarfs. *Astrophysics and Space Science Proceedings*, 36:17, 2014. doi: 10.1007/978-3-319-03041-8_3.

T. Stanke, M. J. McCaughrean, and H. Zinnecker. An unbiased H_2 survey for protostellar jets in Orion A. II\@. The infrared survey data. *Astronomy and Astrophysics*, 392:239–266, September 2002. doi: 10.1051/0004-6361:20020763.

B. Strömgren. The Physical State of Interstellar Hydrogen. *Astrophysical Journal*, 89:526, May 1939. doi: 10.1086/144074.

G. Taylor. The Formation of a Blast Wave by a Very Intense Explosion. I. Theoretical Discussion. *Royal Society of London Proceedings Series A*, 201:159–174, March 1950. doi: 10.1098/rspa.1950.0049.

A. G. G. M. Tielens and D. J. Hollenbach. Photodissociation Regions and Planetary Nebulae. In R. Weinberger and A. Acker, editors, *Planetary Nebulae*, volume 155 of *IAU Symposium*, page 155, 1993.

E. I. Vorobyov. Variable Accretion in the Embedded Phase of Star Formation. *Astrophysical Journal*, 704:715–723, October 2009. doi: 10.1088/0004-637X/704/1/715.

E. I. Vorobyov and S. Basu. The effect of a finite mass reservoir on the collapse of spherical isothermal clouds and the evolution of protostellar accretion. *Monthly Notices of the RAS*, 360:675–684, June 2005. doi: 10.1111/j.1365-2966.2005.09062.x.

E. I. Vorobyov and S. Basu. The Burst Mode of Protostellar Accretion. *Astrophysical Journal*, 650:956–969, October 2006. doi: 10.1086/507320.

E. T. Whelan, T. P. Ray, F. Bacciotti, A. Natta, L. Testi, and S. Randich. A resolved outflow of matter from a brown dwarf. *Nature*, 435:652–654, June 2005. doi: 10.1038/nature03598.

M. G. Wolfire and A. Konigl. Molecular line emission models of Herbig-Haro objects. I - H2 emission. *Astrophysical Journal*, 383:205–225, December 1991. doi: 10.1086/170777.

P. R. Wood. Evolutionary and pulsation properties of AGB stars . *Memorie della Societa Astronomica Italiana*, 81:883, 2010.

H. Zinnecker and R. Mathieu, editors. *The Formation of Binary Stars*, volume 200 of *IAU Symposium*, 2001.

H. Zinnecker and H. W. Yorke. Toward Understanding Massive Star Formation. *Annual Review of Astron and Astrophysics*, 45:481–563, September 2007. doi: 10.1146/annurev.astro.44.051905.092549.

Appendix A

Photometry Code

The following is the code used for the photometry of the H_2 features in the $H_2 -$ K difference images. This will return values for all features within an image.

```python
#!/usr/bin/python

import numpy as np
from math import *
import os
import sys
from astropy.io import fits

hdulist = fits.open('FITS_FILE.fits') #FITS file
#Text file of polygon co-ordinates for all features in the FITS file.
coordlist = open("FEATURE_COORDS.txt", "r")

hdu = hdulist[0]
axis1 = hdu.header['NAXIS1'] #Dimension 1 of FITS file.
axis2 = hdu.header['NAXIS2'] #Dimension 1 of FITS file.


####################################################################################
################################ DEFINE FUNCTIONS ##################################
####################################################################################


# F1)
#This will determine whether a pixel near the feature is within the boundary or not.
#Adapated: http://stackoverflow.com/questions/16625507/ (continued next line)
#python-checking-if-point-is-inside-a-polygon?rq=1
def point_in_poly(x,y,poly):
```

```
        n = len(poly) #Number of coordinates.
        inside = False
        j = 0
        for i in range(n-1):
            #First pair is zeroth index.
            p1x, p1y = poly[j]
            #When last co-ordinate pair become p1x, p1y, use the first pair as p2x and p2y.
            if j == (n-1):
            p2x, p2y = poly[0]
            else:
                #Otherwise use the co-ordinate pair below as p2x, p2y
                p2x, p2y = poly[j+1]

            if min(p1y,p2y) < y <= max(p1y,p2y):
            if x <= max(p1x,p2x):
                if p1y != p2y:
                    xints = (y-p1y)*(p2x-p1x)/(p2y-p1y)+p1x


                    if p1y == p2y and p1x != p2x:
                    xints = None
                    if p1x == p2x or (xints is not None and x <= xints):
                    inside = not inside
            j += 1


    return inside




# F2)
#Will be used to calculate the median pixel value of the feature and its background.
#Adapted: http://stackoverflow.com/questions/24101524/finding-median-of-list-in-python
def median(lst):
            lst = sorted(lst)
            if len(lst) %2 == 1: #If list has odd number of values.
            return lst[((len(lst)+1)/2)-1]
            if len(lst) %2 == 0: #If list has even number of values.
            return float(sum(lst[(len(lst)/2)-1:(len(lst)/2)+1]))/2.0




# F3)
#Will be used to calculate the RMS of the background pixels.
def qmean(bgf,med):
    #Sqaureroot of the sum of background intensitiesminus median background intensities
    #sqaured over the number of background intensities.
    return sqrt(sum((i-med)**2 for i in bgf)/len(bgf))
```

132

```
# F4)
#Will be used to calculate the 3 sigma RMS of the background, eliminating very
#high positive or negative pixel values.
def reduce_rms():

    #Create an array of pixel intensities.
    bgflux=np.genfromtxt('backg_flux.txt',dtype='float',converters=None, (cont.)
    .... usecols=2,unpack=False)
    medbg = median(bgflux) #Initial background intensity median.
        rms = qmean(bgflux,medbg) #Initial RMS value obtained from F3).

    peakbg = max(bgflux) #Peak background intensity.
    bottombg = min(bgflux) #Lowest background intensity, including negative.

    inrange = False #Initial condition is 'RMS < 1?'. Start with False.
    #If the highest or lowest intensity is within three standard deviations of the median:
    if (medbg-(3*rms)) > bottombg or (medbg+(3*rms)) < peakbg:
        while inrange == False:
            oldrms = rms #Create a duplicate of variable 'rms'.
            #Open blank text file to write the impending, 3sigma stripped values to.
            backfluxreduce = open('backg_fluxreduce.txt', 'w')
            for line in bgflux:
             #For each pixel in background, if value is within +- 3sigma of median:
                if (medbg-(3*rms)) <= line <= (medbg+(3*rms)):
                    backfluxreduce.write(('%5.5f\n')%(line)) #Write pixel intensity.
            backfluxreduce.close()

            #The array of pixel values within +- 3sigma
            bgflux=np.loadtxt('backg_fluxreduce.txt',dtype='float',converters=None, (cont.)
            .... usecols=None,unpack=False)
            medbg = median(bgflux) #Calculate new median from these values.
            #Calculate new RMS from values. 'oldrms' is still the previous RMS.
            rms = qmean(bgflux,medbg)

            #If new RMS < 1 or RMS doesnt change, enough outliers have been stripped.
            if rms <= 1.0 or rms == oldrms:
                #Set condition to True, ends while-loop. Else, repeat 3sigma s
                #tripping using the new median and RMS
                inrange = True

    return rms, medbg


########################################################################################
```

133

```
############################################ START ############################################
###############################################################################################

final = open('MY_OUTPUT.txt', 'w')


#Column headings for what properties of each feature are written to the output file
#final.write('#Number of Co-ordinate Pairs of Polygon\n')
#final.write('#Feature Cx Co-ordinate\n')
#final.write('#Feature Cy Co-ordinate\n')
#final.write('#Number of Pixels In Feature\n')
#final.write('#Total Pixel Intensity in Feature\n')
#final.write('#Mean Pixel Intensity in Feature\n')
#final.write('#Median Pixel Intensity in Feature\n')
#final.write('#Peak Pixel Intensity in Feature\n')
#final.write('#Number of Pixels in Background\n')
#final.write('#Total Pixel Intensity in Background\n')
#final.write('#RMS of Background\n')
#final.write('#Median Pixel Intensity in Background After 3sigma\n')
#final.write('#Background Corrected Median Pixel Intensity in Feature\n')


#For a single feature in the FITS file, the following is completed
#before the next feature is analysed:


for line in coordlist:
#Text file for all of pixel intensities whose co-ordinates lie within feature.
    pixelflux = open('pixel_flux.txt', 'w')
  #File for all of pixel intensities whose co-ordinates lie within specified background.
    backflux = open('backg_flux.txt', 'w')


    #Count number of coordinate pairs.
    number=(line.count("␣")+1)/2
        #remove unnecessary text, leaves just the co-ordinate values,
        coord = map(float, line.strip().split('␣'))


    linefile = open('linefile.txt', 'w') #I write 'coord' into a rewriteable file
    linefile.write(line)
    linefile.close()


    mat=np.loadtxt('linefile.txt',dtype='float',converters=None,usecols=None,unpack=False)
    coords = open('pixel_coords.txt','w')
    y = 0
    #For every two numbers in the 'linefile', assigns the first as the
    #x co-ordinate and the seconds as the y co-ordinate.
    for line in range(number):
            a = mat[y]
            b = mat[y+1]
```

134

```
        #write these co-ordinates into a 2-column text file with 'number' amount
        #of rows such that:  x1 y1 \\ x2 y2 \\ x3 y3 \\ ... \\ xnumber ynumber
        coords.write("%s␣%s\n" %(a,b))
        y += 2
coords.close()



#This section deals with calculating the feature area (in pixels) and its
#centre coordinates: Cx & Cy.

#Number of coordinate points starts at 0.
num=0
circx=0
circy=0
number=int(number)
#Loop over all contour coordinate pairs.
for n in range(0,number):


    #similar to F1). Uses first co-ordinate pair as x2,y2
    #when program arrives at the final pair.
    x1=coord[2*n+0]
    y1=coord[2*n+1]
    if n < number-1 :
        x2=coord[2*n+2]
        y2=coord[2*n+3]
    else:
        x2=coord[0]
        y2=coord[1]


    #Area = sum of all pixels. Each pixel represents 0.04 square arcseconds.
    a=((x1)*(y2))-((x2)*(y1))
    num=num+a


    #Cx
    c=((x1)+(x2))*(((x1)*(y2))-((x2)*(y1)))
    circx=circx+c


    #Cy
    d=((y1)+(y2))*(((x1)*(y2))-((x2)*(y1)))
    circy=circy+d



#Area is 1/2 * a(for all coordinates).
A=(num)/2
```

```python
#Cx is 1/(6*Area) * circx(for all coordinates).
cx=circx/(6*A)


#Cy is 1/(6*Area) * circy(for all coordinates).
cy=circy/(6*A)


#Find minimum radius of a circle that can envelop the entire feature.
radius=0
for n in range(0,number):


    x1=coord[2*n+0]
    y1=coord[2*n+1]


    r = sqrt( (x1 - cx)**2 + (y1 - cy)**2)
    if r > radius :
        radius = r


#Turn list of coordinates into a numpy array.
#create array of 2 x number size for x y co-ordinates.
polygon = np.loadtxt('pixel_coords.txt', dtype='float', delimiter='')


#define the maximum and minimum x and y values of a box that can contain the feature
xmax = int(math.ceil(max(x[0] for x in polygon))) #rounds up
xmin = int(min(x[0] for x in polygon)) #rounds down
ymax = int(math.ceil(max(y[1] for y in polygon))) #rounds up
ymin = int(min(y[1] for y in polygon)) #rounds down


insidec = open('inside_poly.txt', 'w') #Text file: write co-ordinate pairs in feature.
outsidec = open('within_bg.txt', 'w') #Text file: write co-ordinates pairs in background.
for xx in range(xmin, xmax):
    for yy in range(ymin, ymax):
        inout = point_in_poly(xx+0.5,yy+0.5,polygon) #sends the x,y pairs
                                                      #from 'polygon' to F1)
        if inout == True: #If pixel is in contour, condition is True.
                          #Write it to 'insidedec'.
            insidec.write('%s %s\n'%(int(xx), int(yy)))
insidec.close()


#Calculated 'radius' is rounded up to integer so feature guaranteed
#to be within circle centroid co-ordinates centre.
radiusup = int(math.ceil(radius))
rad = 2*radiusup #This doubles the rounded up radius.
cxmax = int(math.ceil(cx))+rad
cymax = int(math.ceil(cy))+rad
cxmin = int(cx)-rad
cymin = int(cy)-rad #Defines a box of pixels containing the circle of radius 'rad'
```

```
for xx in range ( cxmin , cxmax ):
    for yy in range ( cymin , cymax ):
        d = sqrt (( cx-xx )**2 + ( cy-yy )**2) #Determines pixel distance from
                                              #centroid coordinates.
        #If distance is within the feature radius and twice that radius ( ring of R->2R ):
        if radius <= d <= 2*radius :
            #And if x is within image boundary , large features near edge of FITS file
            #may have backgrounds off edge of image.
            if 0 <= xx <= axis1 :
                if 0 <= yy <= axis2 : #And if y is within image boundary:
                    #Write coordinate pair to the file 'outsidedec'. It is designed to
                    #not fail if the range of the breakground exceeds image boundaries.
                    outsidec.write ( '%s %s\n'%( int ( xx ), int ( yy )))


outsidec.close ()



#####################################################################################
########################### INSIDE POLYGON - MEAN MEDIAN PEAK #######################
#####################################################################################


#Counts number lines in 'inside_poly' file. Also the number of pixels in feature.
lc = sum (1 for line in open ( 'inside_poly.txt' ))
#Turn the co-ordinate file into an array.
ip=np.loadtxt ( 'inside_poly.txt' ,dtype= 'int' ,converters=None ,usecols=None ,unpack=False )

#Using the array of x,y co-ordinates , this can enter the FITS file and
#grab the pixel intensity of x,y.
data = hdulist [0].data
m = 0
counter = 0
sum_pixint = 0
#For each pixel , write the pixel number , co-ordinates and the pixel intensity.
for line in ip :
        pixint = data [ip [m ,1] , ip [m ,0]]
        counter += 1
        sum_pixint += pixint
        pixelflux.write ( '%s %s  %s  %4.5f\n' %( counter , ip [m ,0] , ip [m ,1] , pixint ))
        m += 1
pixelflux.close ()

#MEAN
mean = sum_pixint / counter
```

```
#MEDIAN
#column 3 is the pixel intensity.
pixelvalues=np.genfromtxt('pixel_flux.txt',dtype='float',converters=None, (cont.)
.... usecols=3,unpack=False)
medianpix = median(pixelvalues)


#PEAK FLUX
peak = max(pixelvalues)


################################################################################
############################## BACKGROUND - RMS AND MEDIAN #######################
################################################################################


    #Creates an array of co-ordinates within the background ring.
    op=np.loadtxt('within_bg.txt',dtype='int',converters=None,usecols=None,unpack=False)
    #Count number of lines in the file to get the number of pixels in the background.
    count = sum(1 for line in open('within_bg.txt'))
    t = 0
    sum_pixintbg = 0
    for line in op:
        pixint = data[op[t,1]-1, op[t,0]-1]
        #This ignores any pixels that have intensity value 'NaN' if near image edges.
        if -1000000 < pixint < 1000000:
            sum_pixintbg += pixint
            backflux.write('%s  %s  %4.5f\n' %(op[t,0], op[t,1], pixint))
        t += 1
    backflux.close()
    rms2, medbg2 = reduce_rms() #Call F4) to get the 3sigma RMS and the background median.


    correct = medianpix - medbg2 #Background corrected median of feature



################################################################################
################################### WRITE TO FILE ###############################
################################################################################


    #WRITE THE OUTPUT
    final.write(('%05d %06.1f %06.1f %05d %+05.5f %+05.5f %+05.5f %+05.5f '...(cont.)
    '%05d %+05.5f %+05.5f %+05.5f %+05.5f\n")%(number,cx,cy,counter, '...(cont.)
    'sum_pixint,mean,medianpix,peak,count,sum_pixintbg,rms2,medbg2, correct))



final.close()
hdulist.close()
```

Appendix B

Example Table of Photometry Output

Table B.1: Table listing all the extended H_2 features in our survey. We list the following columns: Source ID which includes the Galactic Co-ordinates; Right Ascension and Declination in (J2000) system; Area of the H_2 feature; Radius of the H_2 feature; Median surface brightness; Maximum surface brightness; The one-pixel *rms* noise of the background; Total flux of the H_2 feature; Relative flux uncertainty due to photometric calibration; Classification (Jet, PN, SNR or unknown, most likely PDR); Tile name object is on; Image name the object is on; Name of group the object is associated with. This Table is only an excerpt of the first few objects. The full table will be made available online.

Source ID	RA	DEC	A	r	F_{sb}^{med}	F_{sb}^{max}	F_σ	F^{tot}	$\Delta F/F$	C	Tile	Image	Group
	(J2000) [deg]		[arcsec^2]	[arcsec]	[10^{-19}Wm^{-2}arcsec^{-2}]			[10^{-19}Wm^{-2}]	[%]		name	name	name
UWISH2_000.00652+0.15598	266.25682	-28.84930	121.51	18.4	4.26	103.44	6.13	520.11	7.9	u	H2_lm2_15_16	w20130827_00152_x	PDR_UWISH2_359.99949+0.16099
UWISH2_000.01128+0.16305	266.25276	-28.84155	105.35	12.3	4.17	236.49	6.21	447.16	7.9	u	H2_lm2_15_16	w20130827_00152_x	PDR_UWISH2_359.99949+0.16099
UWISH2_000.01490+0.16272	266.25525	-28.83864	22.97	5.3	2.39	18.70	6.31	55.68	7.9	u	H2_lm2_15_16	w20130827_00152_x	PDR_UWISH2_359.99949+0.16099
UWISH2_000.01868+0.16127	266.25891	-28.83617	107.44	10.3	5.54	5159.72	5.95	3916.77	7.9	u	H2_lm2_15_16	w20130827_00152_x	PDR_UWISH2_359.99949+0.16099

Source ID	RA	DEC	A	r	F_{sb}^{med}	F_{sb}^{max}	F_σ	F^{tot}	$\Delta F/F$	C	Tile	Image	Group
	(J2000) [deg]		[arcsec^2]	[arcsec]	[10^{-19}Wm^{-2}arcsec^{-2}]			[10^{-19}Wm^{-2}]	[%]		name	name	name
UWISH2_000.02914+0.16027	266.26611	−28.82777	45.03	5.5	3.32	227.03	6.14	122.05	7.9	u	H2_lm2_15_16	w20130827_00152_x	PDR_UWISH2_359.99949+0.16099
UWISH2_000.03140+0.15965	266.26807	−28.82617	7.45	3.9	2.85	52.26	5.87	20.02	7.9	u	H2_lm2_15_16	w20130827_00152_x	PDR_UWISH2_359.99949+0.16099
UWISH2_000.03229+0.15892	266.26931	−28.82579	5.45	2.1	4.54	15.35	4.81	24.07	7.9	u	H2_lm2_15_16	w20130827_00152_x	PDR_UWISH2_359.99949+0.16099
UWISH2_000.03537+0.16025	266.26985	−28.82247	34.13	5.8	2.80	43.78	5.62	109.51	7.9	u	H2_lm2_15_16	w20130827_00152_x	PDR_UWISH2_359.99949+0.16099
UWISH2_000.03733+0.16046	266.27080	−28.82068	5.16	1.6	4.20	20.33	5.92	24.94	7.9	u	H2_lm2_15_16	w20130827_00152_x	PDR_UWISH2_359.99949+0.16099
UWISH2_000.03836+0.15947	266.27239	−28.82032	6.89	2.6	3.76	17.55	4.91	31.18	7.9	u	H2_lm2_15_16	w20130827_00152_x	PDR_UWISH2_359.99949+0.16099
UWISH2_000.03981+0.16052	266.27222	−28.81854	6.28	2.3	4.92	42.96	5.34	33.02	7.9	u	H2_lm2_15_16	w20130827_00152_x	PDR_UWISH2_359.99949+0.16099
UWISH2_000.04282+0.16170	266.27288	−28.81535	97.74	10.1	4.67	83.26	5.49	460.71	7.9	u	H2_lm2_15_16	w20130827_00152_x	PDR_UWISH2_359.99949+0.16099
UWISH2_000.05025−0.20813	266.63798	−29.00157	142.26	11.1	3.31	40.87	5.40	473.13	8.6	u	H2_lm2_15_17	w20130827_00214_w	PDR_UWISH2_000.06358−0.22066
UWISH2_000.08806−0.62191	267.06548	−29.18349	9.32	3.4	3.46	49.00	5.47	134.56	3.3	j	H2_lm2_15_11	w20130728_00284_y	JET_UWISH2_000.09056−0.65984
UWISH2_000.08823−0.66263	267.10553	−29.20435	7.88	2.9	4.01	115.59	4.03	501.52	3.3	j	H2_lm2_15_11	w20130728_00284_y	JET_UWISH2_000.09056−0.65984
UWISH2_000.09108−0.66396	267.10853	−29.20259	80.40	9.0	3.45	16.82	3.82	37.24	3.3	j	H2_lm2_15_11	w20130728_00284_y	JET_UWISH2_000.09056−0.65984
UWISH2_000.11504−0.26902	266.73592	−28.97779	36.85	5.5	5.44	235.65	5.68	205.86	8.6	u	H2_lm2_15_17	w20130827_00214_w	PDR_UWISH2_000.06358−0.22066
UWISH2_000.12738−0.67989	267.14561	−29.17972	38.85	7.9	3.93	18.81	3.27	35.54	3.3	u	H2_lm2_15_11	w20130728_00284_y	PDR_UWISH2_000.12738−0.67989
UWISH2_000.16461+0.06333	266.44110	−28.76272	79.54	10.7	8.49	296.66	7.80	803.54	10.5	u	H2_lm2_15_16	w20130827_00188_x	PDR_UWISH2_000.16461+0.06333
UWISH2_000.16477−0.44615	266.93862	−29.02699	166.67	13.9	3.41	62.37	3.93	771.07	10.9	j	H2_lm2_15_17	w20130827_00238_w	JET_UWISH2_000.23142−0.46461
UWISH2_000.20896−0.46070	266.97899	−28.99669	6.28	2.4	4.83	16.10	3.50	30.03	10.9	j	H2_lm2_15_17	w20130827_00238_w	JET_UWISH2_000.23142−0.46461
UWISH2_000.20910−0.45307	266.97160	−28.99263	38.79	5.8	4.01	35.30	4.30	168.47	10.9	j	H2_lm2_15_17	w20130827_00238_w	JET_UWISH2_000.23142−0.46461
UWISH2_000.22494−0.47121	266.99872	−28.98844	6.56	2.7	3.05	11.15	3.17	21.34	10.9	j	H2_lm2_15_17	w20130827_00238_w	JET_UWISH2_000.23142−0.46461
UWISH2_000.22655−0.47021	266.99869	−28.98655	25.29	4.5	2.85	15.55	3.30	76.70	10.9	j	H2_lm2_15_17	w20130827_00238_w	JET_UWISH2_000.23142−0.46461
UWISH2_000.24117−0.47622	267.01321	−28.97713	48.86	7.7	2.32	18.53	3.01	121.54	10.9	j	H2_lm2_15_17	w20130827_00238_w	JET_UWISH2_000.23142−0.46461
UWISH2_000.25247−0.47064	267.01442	−28.96458	169.46	10.8	2.57	155.29	3.07	530.41	10.9	j	H2_lm2_15_17	w20130827_00238_w	JET_UWISH2_000.23142−0.46461
UWISH2_000.26373−0.19745	266.75411	−28.81354	253.29	14.8	5.69	2210.84	7.39	2781.84	7.8	u	H2_lm2_15_17	w20130827_00226_w	PDR_UWISH2_000.31030−0.20300
UWISH2_000.27057−0.45385	267.00868	−28.94041	14.72	3.5	3.65	25.52	2.93	73.37	10.9	j	H2_lm2_15_17	w20130827_00238_w	JET_UWISH2_000.23142−0.46461

Continued on next page

140

Source ID	RA	DEC	A	r	F_{sb}^{med}	F_{sb}^{max}	F_σ	F^{tot}	$\Delta F/F$	C	Tile	Image	Group
	(J2000) [deg]		[arcsec^2]	[arcsec]	[10^{-19}Wm^{-2}arcsec^{-2}]			[10^{-19}Wm^{-2}]	[%]		name	name	name
UWISH2_000.28306−0.47766	267.03934	−28.94201	148.32	12.6	3.80	183.74	3.05	746.67	10.9	j	H2_lm2_15_17	w20130827_00238_w	JET_UWISH2_000.23142−0.46461
UWISH2_000.30634−0.17075	266.75326	−28.76326	53.68	7.8	3.00	115.90	3.75	335.33	7.8	j	H2_lm2_15_17	w20130827_00226_w	JET_UWISH2_000.31666−0.18594
UWISH2_000.30904−0.21135	266.79447	−28.78200	21.05	3.5	7.24	41.57	4.98	187.12	7.8	u	H2_lm2_15_17	w20130827_00226_w	PDR_UWISH2_000.31030−0.20300
UWISH2_000.31508−0.20018	266.78715	−28.77105	967.36	49.7	6.91	3377.88	4.89	16183.15	7.8	u	H2_lm2_15_17	w20130827_00226_w	PDR_UWISH2_000.31030−0.20300
UWISH2_000.31792−0.19281	266.78163	−28.76480	18.46	3.7	4.84	30.59	3.34	233.24	7.8	u	H2_lm2_15_17	w20130827_00226_w	PDR_UWISH2_000.31030−0.20300
UWISH2_000.32140−0.22713	266.81717	−28.77960	90.22	10.3	3.70	355.74	4.18	315.07	7.8	u	H2_lm2_15_17	w20130827_00226_w	PDR_UWISH2_000.31030−0.20300
UWISH2_000.32288−0.20320	266.79470	−28.76594	22.45	5.0	3.08	23.90	3.86	99.16	7.8	j	H2_lm2_15_17	w20130827_00226_w	JET_UWISH2_000.31666−0.18594
UWISH2_000.32301−0.20783	266.79929	−28.76823	70.54	8.6	3.01	16.65	3.97	200.99	7.8	u	H2_lm2_15_17	w20130827_00226_w	PDR_UWISH2_000.31030−0.20300
UWISH2_000.32489−0.21032	266.80283	−28.76791	19.50	4.0	4.87	41.71	3.69	133.61	7.8	u	H2_lm2_15_17	w20130827_00226_w	PDR_UWISH2_000.31030−0.20300
UWISH2_000.32524−0.20528	266.79812	−28.76500	102.03	9.7	2.51	18.15	3.93	51.46	7.8	u	H2_lm2_15_17	w20130827_00226_w	PDR_UWISH2_000.31030−0.20300
UWISH2_000.32696−0.19658	266.79066	−28.75902	40.23	6.4	1.66	16.62	3.45	35.40	7.8	j	H2_lm2_15_17	w20130827_00226_w	JET_UWISH2_000.31666−0.18594
UWISH2_000.32730−0.20233	266.79646	−28.76171	31.46	7.5	5.76	212.38	5.04	450.39	7.8	u	H2_lm2_15_17	w20130827_00226_w	PDR_UWISH2_000.31030−0.20300
UWISH2_000.32775−0.21154	266.80572	−28.76610	148.28	9.8	2.91	40.24	3.48	428.10	7.8	u	H2_lm2_15_17	w20130827_00226_w	PDR_UWISH2_000.31030−0.20300
UWISH2_000.32998−0.20366	266.79935	−28.76011	11.38	4.1	3.27	10.70	3.60	40.00	7.8	u	H2_lm2_15_17	w20130827_00226_w	PDR_UWISH2_000.31030−0.20300
UWISH2_000.38851−0.62473	267.24546	−28.92752	5.23	1.8	5.41	34.87	4.31	47.96	8.6	j	H2_lm2_15_17	w20130827_00214_x	JET_UWISH2_000.48489−0.68601
UWISH2_000.39571+0.20634	266.43912	−28.49095	17.04	3.6	6.75	26.22	5.29	121.43	6.4	u	H2_lm2_15_16	w20130827_00176_y	PDR_UWISH2_000.40129+0.21193
UWISH2_000.39726+0.20853	266.43792	−28.48849	64.85	8.4	6.59	5525.55	5.30	6375.84	6.4	u	H2_lm2_15_16	w20130827_00176_y	PDR_UWISH2_000.40129+0.21193
UWISH2_000.40382+0.21417	266.43633	−28.47996	140.67	14.7	5.19	891.35	5.11	695.27	6.4	u	H2_lm2_15_16	w20130827_00176_y	PDR_UWISH2_000.40129+0.21193
UWISH2_000.41135−0.56867	267.20401	−28.87906	10.77	3.0	2.74	27.84	3.98	108.63	8.6	u	H2_lm2_15_17	w20130827_00214_x	PDR_UWISH2_000.41634−0.56827
UWISH2_000.41656−0.56825	267.20666	−28.87438	241.30	29.3	6.10	47.51	4.03	222.50	8.6	u	H2_lm2_15_17	w20130827_00214_x	PDR_UWISH2_000.41634−0.56827
UWISH2_000.45198−0.69240	267.34905	−28.90793	12.11	3.0	4.64	31.18	3.95	65.46	8.6	j	H2_lm2_15_17	w20130827_00214_x	JET_UWISH2_000.48489−0.68601
UWISH2_000.46375−0.69183	267.35542	−28.89754	33.83	5.4	6.02	33.35	3.58	44.08	8.6	j	H2_lm2_15_17	w20130827_00214_x	JET_UWISH2_000.48489−0.68601
UWISH2_000.47577−0.10395	266.78827	−28.58375	315.34	15.2	6.57	11084.29	6.76	9244.19	8.6	u	H2_lm2_15_17	w20130827_00214_z	PDR_UWISH2_000.50861−0.09983
UWISH2_000.47915−0.70944	267.38171	−28.89339	28.64	6.1	5.36	95.27	4.06	149.50	8.6	j	H2_lm2_15_17	w20130827_00214_x	JET_UWISH2_000.48489−0.68601

141

Source ID	RA	DEC	A	r	F_{sb}^{med}	F_{sb}^{max}	F_{σ}	F^{tot}	$\Delta F/F$	C	Tile	Image	Group
	(J2000) [deg]		[arcsec^2]	[arcsec]	[10^{-19}Wm^{-2}arcsec^{-2}]			[10^{-19}Wm^{-2}]	[%]		name	name	name
UWISH2_000.48097−0.70716	267.38054	−28.89065	6.87	2.5	2.98	19.91	4.53	94.59	8.6	j	H2_lm2_15_17	w20130827_00214_x	JET_UWISH2_000.48489−0.68601
UWISH2_000.48113−0.69815	267.37181	−28.88588	65.91	7.0	4.66	130.65	5.22	327.87	8.6	j	H2_lm2_15_17	w20130827_00214_x	JET_UWISH2_000.48489−0.68601
UWISH2_000.48123−0.71211	267.38555	−28.89297	19.81	4.3	4.45	18.26	4.32	32.65	8.6	j	H2_lm2_15_17	w20130827_00214_x	JET_UWISH2_000.48489−0.68601
UWISH2_000.48162−0.70885	267.38257	−28.89096	7.34	2.7	3.55	5338.14	4.55	7995.51	8.6	j	H2_lm2_15_17	w20130827_00214_x	JET_UWISH2_000.48489−0.68601
UWISH2_000.48347−0.11515	266.80372	−28.58297	53.79	7.1	8.88	277.54	6.61	529.51	8.6	j	H2_lm2_15_17	w20130827_00214_z	JET_UWISH2_000.48596−0.11519
UWISH2_000.48780−0.11562	266.80673	−28.57951	16.90	4.1	4.86	26.27	6.68	86.61	8.6	j	H2_lm2_15_17	w20130827_00214_z	JET_UWISH2_000.48596−0.11519
UWISH2_000.48984−0.11501	266.80734	−28.57745	26.50	5.4	4.48	193.47	5.83	836.79	8.6	j	H2_lm2_15_17	w20130827_00214_z	JET_UWISH2_000.48596−0.11519
UWISH2_000.49102−0.64245	267.32307	−28.84876	8.14	3.0	5.31	32.65	4.58	49.05	8.6	j	H2_lm2_15_17	w20130827_00214_x	JET_UWISH2_000.48489−0.68601
UWISH2_000.50459−0.78770	267.47334	−28.91176	25.07	5.6	3.80	52.54	4.61	222.02	10.9	u	H2_lm2_15_17	w20130827_00238_x	PDR_UWISH2_000.57908−0.85893
UWISH2_000.51701−0.65611	267.35170	−28.83350	33.30	6.2	4.54	25.22	4.60	49.90	8.6	j	H2_lm2_15_17	w20130827_00214_x	JET_UWISH2_000.48489−0.68601
UWISH2_000.51855−0.65899	267.35542	−28.83366	6.37	2.0	5.22	24.74	3.78	33.24	8.6	j	H2_lm2_15_17	w20130827_00214_x	JET_UWISH2_000.48489−0.68601
UWISH2_000.52020−0.65446	267.35196	−28.82992	23.24	4.6	8.08	36.06	4.44	181.44	8.6	j	H2_lm2_15_17	w20130827_00214_x	JET_UWISH2_000.48489−0.68601
UWISH2_000.54160−0.85338	267.55943	−28.91369	22.38	4.4	4.54	1202.53	4.00	248.36	10.9	j	H2_lm2_15_17	w20130827_00238_x	JET_UWISH2_000.57163−0.87718
UWISH2_000.54163−0.84176	267.54805	−28.90771	44.34	9.2	4.72	14.54	4.32	61.68	10.9	u	H2_lm2_15_17	w20130827_00238_x	PDR_UWISH2_000.57908−0.85893
UWISH2_000.54344−0.85947	267.56648	−28.91524	98.22	10.7	3.87	336.75	5.00	380.25	10.9	u	H2_lm2_15_17	w20130827_00238_x	PDR_UWISH2_000.57908−0.85893
UWISH2_000.54348−0.84696	267.55423	−28.90879	14.06	4.9	4.50	50.22	4.04	94.24	10.9	u	H2_lm2_15_17	w20130827_00238_x	PDR_UWISH2_000.57908−0.85893
UWISH2_000.54377−0.85233	267.55967	−28.91129	17.77	4.0	3.83	16.16	4.39	17.37	10.9	j	H2_lm2_15_17	w20130827_00238_x	JET_UWISH2_000.57163−0.87718
....													

Appendix C

Table of Planetary Nebulae

Table C.1: Table listing all the PNe detected in our survey. We list the UWISH2 PN source ID, which includes the Galactic co-ordinates, the RA and DEC (J2000) positions of the geometric centre of the H_2 emission features that compose the PN, the radius around this central position enclosing all the H_2 emission, the area covered by H_2 emission, the total and MSB fluxes of the PN, and any other known name/identifier or coinciding object (not necessarily a PN). 'New' in the last column indicates objects that have so far not been recognised as PNe or PNe candidates in the literature.

Source ID	RA	DEC	Radius	Area	F_{tot}	F_{med}	Other ID
	[deg]	[deg]	[arcsec]	[arcsec^2]	$[10^{-19}Wm^{-2}]$		
PN_UWISH2_000.81878−0.04944	266.93718	−28.26207	6.3	52.97	388.50	345.89	SSTGC 841071
PN_UWISH2_001.22588+0.56414	266.58223	−27.59584	5.7	44.18	386.74	331.79	New
PN_UWISH2_001.42213−0.61357	267.83773	−28.03457	16.9	243.11	1706.78	1796.58	New
PN_UWISH2_001.65056+0.18803	267.19290	−27.42713	14.8	298.48	2544.15	2286.36	PN G001.6+00.1
PN_UWISH2_001.72196−0.82262	268.21435	−27.88315	17.3	211.92	6355.37	1543.66	New
PN_UWISH2_001.73118+0.44232	266.99457	−27.22684	12.2	137.19	498.93	439.01	New
PN_UWISH2_002.03824−0.34363	267.93092	−27.36701	23.4	149.54	680.57	655.32	New
PN_UWISH2_002.25319+0.55724	267.18642	−26.72043	47.7	1312.63	1712.21	9032.45	PN G002.2+00.5
PN_UWISH2_003.65197−0.25068	268.75783	−25.92948	4.9	48.46	323.03	309.66	New
PN_UWISH2_003.79367−0.81428	269.37918	−26.09041	5.7	35.84	746.92	224.72	New
PN_UWISH2_004.44847−0.21905	269.17220	−25.22542	88.9	2267.66	7638.52	18397.78	New
PN_UWISH2_004.76799−0.85257	269.95542	−25.26527	17.1	289.48	0582.35	2023.47	New
PN_UWISH2_004.88887−0.58981	269.77016	−25.02963	38.6	690.14	3875.28	3181.93	PN G004.8−00.5
PN_UWISH2_004.99841−0.72107	269.95596	−24.99999	6.5	60.86	338.48	306.73	New
PN_UWISH2_005.14078+0.58616	268.79000	−24.22186	6.5	40.10	205.82	202.82	New
PN_UWISH2_005.42811−0.16852	269.66434	−24.35213	26.1	178.42	906.42	848.62	New
PN_UWISH2_005.56222−0.15023	269.72037	−24.22679	10.5	112.38	478.75	485.48	New
PN_UWISH2_005.90685−1.37325	271.07450	−24.53226	17.8	279.37	992.38	1008.53	New
PN_UWISH2_006.51856−0.69279	270.75465	−23.66517	8.5	96.85	425.90	405.80	New
PN_UWISH2_006.73073−1.19177	271.34313	−23.72525	11.0	169.83	829.38	765.93	New
PN_UWISH2_008.33574−1.10291	272.10781	−22.28043	19.1	109.88	1414.41	551.62	PN G008.3−01.1
PN_UWISH2_008.36142−0.62384	271.66930	−22.02504	8.9	112.93	794.42	606.43	IRAS 18036−2201
PN_UWISH2_008.94169+0.25318	271.15183	−21.09003	15.7	205.01	1280.44	1158.31	MGE G008.9409+00.2532
PN_UWISH2_009.76150−0.95756	272.71231	−20.96230	10.7	143.92	1308.31	761.34	SSTGLMC G009.7612−00.9575
PN_UWISH2_009.80708−1.14613	272.91283	−21.01314	20.9	376.92	3534.44	3056.88	PN G009.8−01.1
PN_UWISH2_010.10373+0.73752	271.30883	−19.83976	110.7	2993.26	23449.28	20473.46	PN G010.1+00.7
PN_UWISH2_010.21147+0.34469	271.72932	−19.93758	30.7	190.12	571.03	555.52	PN G010.2+00.3

144

Table C.1 – continued from previous page

Source ID	RA	DEC	Radius	Area	F_{tot}	F_{med}	Other ID
	[deg]	[deg]	[arcsec]	[arcsec^2]	$[10^{-19}\mathrm{Wm}^{-2}]$		
PN_UWISH2_010.26120−0.79452	272.81690	−20.44591	8.0	132.78	537.11	512.53	New
PN_UWISH2_010.39239+0.53966	271.64211	−19.68458	20.1	301.02	1239.45	1159.96	SSTGLMC G010.393+00.538
PN_UWISH2_010.94194−0.40277	272.80040	−19.66068	13.2	133.56	435.56	422.76	New
PN_UWISH2_011.00185+1.44395	271.12230	−18.71089	18.7	503.97	6480.38	3915.85	PN G011.0+01.4
PN_UWISH2_011.32982+0.54981	272.11575	−18.86062	7.4	98.14	360.27	424.95	New
PN_UWISH2_011.45829+1.07349	271.69860	−18.49376	4.0	49.55	455.05	345.22	IRAS 18038−1830
PN_UWISH2_011.52915+1.00385	271.79911	−18.46579	8.2	72.03	181.51	188.48	PN G011.5+01.0
PN_UWISH2_011.86338+0.30190	272.61733	−18.51366	6.0	67.67	292.62	280.15	New
PN_UWISH2_012.11515+0.07516	272.95467	−18.40229	12.3	179.10	899.29	872.22	GPSR5 12.116+0.076
PN_UWISH2_012.20907+0.43081	272.67407	−18.14868	5.2	36.29	93.15	87.46	New
PN_UWISH2_012.21971−0.33477	273.38671	−18.50730	10.8	67.23	241.45	198.28	New
PN_UWISH2_012.71728+0.37202	272.98548	−17.73160	7.6	105.71	403.04	372.10	New
PN_UWISH2_012.80348+0.00510	273.36698	−17.83207	16.9	144.48	463.28	427.44	New
PN_UWISH2_013.61090+1.01274	272.84745	−16.64001	9.2	145.48	820.75	699.76	New
PN_UWISH2_014.58523+0.46161	273.83795	−16.04881	7.4	56.81	247.96	213.56	PN G014.5+00.4
PN_UWISH2_014.64501+0.08920	274.20847	−16.17352	10.4	85.77	317.09	321.64	New
PN_UWISH2_014.65833+1.01220	273.37138	−15.72154	18.8	186.94	887.33	882.35	PN G014.6+01.0
PN_UWISH2_014.92112+0.06989	274.36260	−15.93970	17.5	101.11	384.56	385.95	IRAS 18145−1557
PN_UWISH2_015.13012−0.44046	274.93310	−15.99718	30.5	368.79	1810.59	1662.43	New
PN_UWISH2_015.53753−0.01923	274.74746	−15.43907	29.9	43.62	189.24	178.44	PN G015.5−00.0
PN_UWISH2_015.54859−1.00657	275.65740	−15.89444	8.5	73.78	414.18	379.23	IRAS 18197−1555
PN_UWISH2_015.67993−1.36320	276.04901	−15.94546	11.4	150.86	693.24	629.09	New
PN_UWISH2_016.02790−1.00525	275.88952	−15.47051	4.7	41.72	152.10	146.44	New
PN_UWISH2_016.11984−0.98789	275.91826	−15.38115	16.6	110.13	255.34	259.28	New
PN_UWISH2_016.17480+1.37914	273.78738	−14.21429	12.5	114.53	345.46	350.14	New
PN_UWISH2_016.41571−0.93047	276.00920	−15.09285	32.3	326.45	1539.81	1349.89	PN G016.4−00.9
PN_UWISH2_016.48834−1.36082	276.43858	−15.22966	33.8	188.83	570.06	557.68	New
PN_UWISH2_016.60078−0.27565	275.50065	−14.62230	8.5	101.08	461.29	411.40	New
PN_UWISH2_016.92321−0.00616	275.41159	−14.21103	6.7	64.19	185.62	179.73	New
PN_UWISH2_017.22288+0.12645	275.43624	−13.88420	37.3	232.61	1324.38	790.29	PN G017.2+00.1
PN_UWISH2_017.58861+1.09048	274.73927	−13.10716	7.8	72.61	282.56	256.31	New
PN_UWISH2_017.61528−1.17013	276.80657	−14.14383	152.8	6864.53	330258.97	85111.55	PN G017.6−01.1
PN_UWISH2_018.14941+1.53214	274.61205	−12.40431	9.9	73.37	356.23	285.41	PN G018.1+01.5
PN_UWISH2_018.41760−0.10793	276.22489	−12.93880	14.8	250.57	7524.71	1420.73	New
PN_UWISH2_018.83207+0.48278	275.88871	−12.29607	3.6	29.65	193.62	182.94	New

Table C.1 – continued from previous page

Source ID	RA	DEC	Radius	Area	F_{tot}	F_{med}	Other ID
	[deg]	[deg]	[arcsec]	[arcsec^2]	[10^{-19}Wm^{-2}]		
PN_UWISH2_020.46958+0.67836	276.49348	−10.75715	31.0	144.90	497.17	474.42	PN G020.4+00.6
PN_UWISH2_020.70907−0.17267	277.37398	−10.94099	12.9	261.67	1516.99	1431.33	New
PN_UWISH2_020.80590−0.57267	277.78078	−11.04048	16.4	202.93	898.55	855.13	New
PN_UWISH2_020.85450+0.48588	276.84922	−10.50625	2.4	10.67	108.07	67.97	SSTGLMC G020.8543+00.4857
PN_UWISH2_020.97795+0.92363	276.51391	−10.19310	28.1	137.21	684.15	592.45	GPSR 020.979+0.925
PN_UWISH2_020.98141+0.85244	276.57954	−10.22323	25.7	293.44	1726.19	1527.14	MHO 3200
PN_UWISH2_021.29383+0.98091	276.61194	−9.88697	9.6	109.65	417.59	382.68	PN G021.2+00.9
PN_UWISH2_021.30767−0.25089	277.72679	−10.44677	22.0	103.42	303.70	295.95	New
PN_UWISH2_021.74338−0.67287	278.31186	−10.25536	14.0	211.85	1983.87	1480.83	PN G021.7−00.6
PN_UWISH2_021.81951−0.47837	278.17225	−10.09807	26.3	429.56	2257.37	2074.66	PN G021.8−00.4
PN_UWISH2_022.44734−0.44228	278.43371	−9.52442	25.3	165.39	608.36	580.98	New
PN_UWISH2_022.57000+1.05505	277.14674	−8.72291	13.1	289.63	3901.84	3278.61	PN G022.5+01.0
PN_UWISH2_022.99501−0.56968	278.80394	−9.09703	7.8	83.05	255.30	243.34	New
PN_UWISH2_022.99982+0.10714	278.19818	−8.78078	22.7	183.99	666.78	624.85	New
PN_UWISH2_023.44011+0.74528	277.83172	−8.09545	10.4	160.99	996.94	898.32	PN G023.4+00.7
PN_UWISH2_023.78286+0.50238	278.20917	−7.90372	3.5	23.67	126.19	106.99	New
PN_UWISH2_023.89021−0.73778	279.37125	−8.37930	12.8	158.79	426.44	567.42	GPSR 023.890−0.737
PN_UWISH2_023.90016−1.28024	279.86330	−8.61917	13.6	238.74	1905.40	1258.16	PN G023.9−01.2
PN_UWISH2_024.58540+0.11989	278.92479	−7.36772	7.8	43.53	162.26	138.43	New
PN_UWISH2_024.76272−0.91396	279.93336	−7.68478	2.8	16.29	110.21	97.41	New
PN_UWISH2_024.77483−1.31616	280.29988	−7.85808	41.4	93.54	261.05	256.44	MHO 2456
PN_UWISH2_024.89596+0.45853	278.76581	−6.93617	9.2	118.28	341.25	891.83	G024.8959+00.4586
PN_UWISH2_025.66408+1.15020	278.50388	−5.93589	28.4	151.60	402.43	414.26	PN G025.6+01.1
PN_UWISH2_025.77993−0.44005	279.97837	−6.56355	4.1	37.20	284.64	231.01	New
PN_UWISH2_025.92671−0.98449	280.53333	−6.68220	10.0	106.93	1165.94	857.58	PN G025.9−00.9
PN_UWISH2_025.99096−0.59183	280.21143	−6.44546	5.5	116.81	730.31	685.15	New
PN_UWISH2_026.42837+1.03759	278.95767	−5.30927	5.2	35.20	144.32	124.96	New
PN_UWISH2_026.44767−0.80840	280.61536	−6.13843	7.6	74.54	374.88	348.10	New
PN_UWISH2_026.74999−1.21865	281.12124	−6.05692	12.8	308.77	1998.37	1713.67	PN G026.7−01.2
PN_UWISH2_026.79572−1.05024	280.99156	−5.93937	13.2	201.09	1233.94	1023.55	PN G026.8−01.0
PN_UWISH2_026.83269−0.15180	280.20553	−5.49569	6.9	66.40	490.11	436.91	PN G026.8−00.1
PN_UWISH2_026.83640+0.28828	279.81431	−5.29077	4.9	42.57	316.53	310.34	New
PN_UWISH2_027.09954+0.94886	279.34624	−4.75395	6.8	75.15	233.94	226.95	New
PN_UWISH2_027.37280+1.39262	279.07660	−4.30750	4.1	21.17	60.48	62.66	New
PN_UWISH2_027.66357−0.82670	281.18977	−5.06529	11.7	137.45	664.66	598.03	PN G027.6−00.8

146

Table C.1 – continued from previous page

Source ID	RA	DEC	Radius	Area	F_{tot}	F_{med}	Other ID
	[deg]	[deg]	[arcsec]	[arcsec^2]	[10^{-19}Wm^{-2}]		
PN_UWISH2_027.70327+0.70354	279.84264	−4.33003	37.4	386.40	1632.32	1556.50	PN G027.7+00.7
PN_UWISH2_027.81843−0.76628	281.20679	−4.89994	7.1	56.83	318.47	289.26	PN G027.8−00.7
PN_UWISH2_028.06295−0.61048	281.17972	−4.61128	4.9	34.62	137.77	132.94	New
PN_UWISH2_028.19767−0.89109	281.49190	−4.61951	11.7	61.46	164.11	161.12	New
PN_UWISH2_028.52225−1.48422	282.16994	−4.60108	30.4	99.29	274.33	277.01	PN G028.5−01.4
PN_UWISH2_028.62122−0.86537	281.66273	−4.23091	7.7	29.57	63.90	65.83	New
PN_UWISH2_028.89451−0.29151	281.27590	−3.72585	32.6	202.61	780.88	762.12	PN G028.8−00.2
PN_UWISH2_029.21554+0.02262	281.14282	−3.29679	22.0	215.51	2369.65	711.76	New
PN_UWISH2_029.50204+0.62395	280.73827	−2.76719	15.6	316.05	1600.87	1607.46	PN G029.5+00.6
PN_UWISH2_029.57883−0.26901	281.56882	−3.10673	6.1	49.36	258.66	660.93	PN G029.5−00.2
PN_UWISH2_029.99765+0.65621	280.93623	−2.31163	5.6	55.76	351.46	325.64	G30.421−0.226
PN_UWISH2_030.04497+0.03465	281.51132	−2.55337	31.1	452.87	1929.37	1880.83	PN G030.0+00.0
PN_UWISH2_030.17049+0.68782	280.98710	−2.14346	5.9	54.68	356.97	300.21	New
PN_UWISH2_030.22594+0.54285	281.14150	−2.16034	14.0	108.68	414.40	398.18	New
PN_UWISH2_030.30097−1.22812	282.75329	−2.90143	9.0	78.48	351.91	292.73	New
PN_UWISH2_030.50743−0.21913	281.94856	−2.25769	17.0	199.62	943.44	847.33	PN G030.5−00.2
PN_UWISH2_030.66759−0.33136	282.12162	−2.16634	11.7	76.83	399.40	322.69	G030.6671−00.3316
PN_UWISH2_030.72160+0.14788	281.71954	−1.89964	14.9	100.07	270.46	280.51	New
PN_UWISH2_030.76828+1.40983	280.61768	−1.28196	3.7	24.77	126.92	114.19	New
PN_UWISH2_031.16908+0.81029	281.33422	−1.19919	3.3	22.97	95.06	90.50	New
PN_UWISH2_031.32618−0.53286	282.60153	−1.67212	44.9	592.19	3797.09	3019.22	PN G031.3−00.5
PN_UWISH2_031.63781+0.99595	281.38290	−0.69744	6.6	62.40	389.78	344.45	New
PN_UWISH2_031.90685−0.30936	282.66738	−1.05343	27.7	368.30	2400.90	2183.65	PN G031.9−00.3
PN_UWISH2_032.14993+0.64445	281.92933	−0.40212	7.6	62.99	300.67	251.96	New
PN_UWISH2_032.22860−1.44045	283.82102	−1.28266	30.1	211.09	597.61	614.37	PN G032.2−01.4
PN_UWISH2_032.28479−0.27816	282.81195	−0.70284	7.2	91.60	477.47	438.76	New
PN_UWISH2_032.29224−0.74568	283.23149	−0.90936	4.1	29.38	231.96	173.05	New
PN_UWISH2_032.37721−0.55490	283.10042	−0.74677	7.6	79.64	444.97	406.96	PN G032.3−00.5
PN_UWISH2_032.46866+0.28147	282.39772	−0.28401	6.6	53.49	199.32	171.17	New
PN_UWISH2_032.54650−0.03210	282.71230	−0.35773	17.9	281.26	2062.73	1760.69	PN G032.5−00.0
PN_UWISH2_032.54998−0.29529	282.94812	−0.47464	12.5	219.21	1571.41	1552.01	PN G032.5−00.3
PN_UWISH2_032.61348+0.79678	282.00515	+0.07986	3.8	31.65	241.38	160.47	PN PM 1−258
PN_UWISH2_032.66916−1.25559	283.85720	−0.80638	10.2	124.80	973.71	817.44	PN G032.6−01.2
PN_UWISH2_032.94004−0.74662	283.52766	−0.33328	7.9	102.73	759.84	697.54	PN G032.9−00.7
PN_UWISH2_033.16509+0.49150	282.52836	+0.43156	3.8	25.56	106.84	108.63	New

Table C.1 – continued from previous page

Source ID	RA	DEC	Radius	Area	F_{tot}	F_{med}	Other ID
	[deg]	[deg]	[arcsec]	[arcsec^2]	$[10^{-19}\mathrm{Wm}^{-2}]$		
PN_UWISH2_033.45470−0.61500	283.64519	+0.18474	4.8	24.37	27.24	76.77	PN G033.4−00.6
PN_UWISH2_033.88796+1.52134	281.94106	+1.54427	33.8	86.69	255.42	247.80	PN G033.8+01.5
PN_UWISH2_033.97946−0.98557	284.21432	+0.48266	2.2	4.42	8.03	8.88	PN G033.9−00.9
PN_UWISH2_034.10462−1.64333	284.85672	+0.29388	12.0	148.05	1176.28	1034.87	PN G034.1−01.6
PN_UWISH2_034.41021+0.81477	282.80828	+1.68706	4.5	36.56	115.32	110.41	New
PN_UWISH2_034.84509+1.31721	282.55901	+2.30305	9.1	125.35	698.43	611.71	New
PN_UWISH2_035.18522+1.12134	282.88860	+2.51653	11.5	43.14	107.63	103.53	New
PN_UWISH2_035.23366−1.13623	284.92089	+1.52961	30.0	120.64	251.39	255.44	New
PN_UWISH2_035.38919−1.17506	285.02650	+1.65019	12.0	122.81	375.93	372.11	New
PN_UWISH2_035.47394−0.43716	284.40844	+2.06260	20.9	292.90	1251.38	1039.51	IRAS 18551+0159
PN_UWISH2_035.76967−1.24531	285.26293	+1.95644	16.6	461.29	3353.90	2827.71	New
PN_UWISH2_035.81426+1.48019	282.85558	+3.23983	11.8	75.27	181.05	183.03	New
PN_UWISH2_035.81489−0.25181	284.39919	+2.45055	15.6	279.99	850.69	834.37	New
PN_UWISH2_035.89918−1.14425	285.23222	+2.11780	4.9	44.77	196.69	182.66	New
PN_UWISH2_036.05309−1.36593	285.49991	+2.15329	149.5	4344.13	22362.90	20233.61	PN G035.9−01.1
PN_UWISH2_036.43225−1.91396	286.16112	+2.23949	1.7	4.02	58.24	30.95	PN G036.4−01.9
PN_UWISH2_036.46081+0.80581	283.75199	+3.50792	10.5	47.01	71.59	73.22	New
PN_UWISH2_036.48189+0.15610	284.34075	+3.23021	8.9	98.54	440.57	369.52	New
PN_UWISH2_036.98479−0.20330	284.89114	+3.51340	7.2	106.23	311.99	290.01	New
PN_UWISH2_037.14125+0.30341	284.51110	+3.88408	6.8	55.62	138.70	135.16	New
PN_UWISH2_037.41544−0.19254	285.07885	+3.90133	5.0	55.13	365.57	311.48	New
PN_UWISH2_037.96134+0.45337	284.75297	+4.68210	7.2	50.18	257.08	243.87	MSX6C G037.9595+00.4535
PN_UWISH2_038.14463−0.57489	285.75429	+4.37465	6.5	66.25	255.38	257.05	New
PN_UWISH2_038.83959+0.87057	284.78315	+5.65389	5.5	51.95	200.06	197.93	New
PN_UWISH2_039.16222+0.78375	285.00892	+5.90117	7.1	24.74	54.26	45.90	New
PN_UWISH2_039.26101−0.55123	286.24689	+5.37758	13.8	100.73	252.46	253.89	New
PN_UWISH2_039.64158−0.36822	286.25902	+5.79968	4.3	37.29	208.89	170.42	New
PN_UWISH2_040.03148−1.30313	287.27361	+5.71599	29.0	42.09	86.46	82.29	GPSR 040.033−1.302
PN_UWISH2_040.36950−0.47517	286.69085	+6.39710	32.2	1195.79	2682.48	9475.86	PN G040.3−00.4
PN_UWISH2_040.47073+1.10067	285.32726	+7.20967	7.6	76.14	797.05	546.69	New
PN_UWISH2_040.53948−0.76310	287.02679	+6.41554	8.0	144.08	050.63	1022.97	New
PN_UWISH2_040.96700−1.22601	287.63857	+6.58146	61.5	382.13	1021.97	1026.43	New
PN_UWISH2_041.27043−0.69797	287.30768	+7.09423	16.3	405.50	3270.84	2883.10	PN G041.2−00.6
PN_UWISH2_041.99634+0.10743	286.92389	+8.10956	19.9	16.17	24.70	26.29	New
PN_UWISH2_042.12631+0.45706	286.67062	+8.38580	9.0	126.16	547.41	509.69	New

Table C.1 – continued from previous page

Source ID	RA	DEC	Radius	Area	F_{tot}	F_{med}	Other ID
	[deg]	[deg]	[arcsec]	[arcsec^2]	[10^{-19}Wm^{-2}]	
PN_UWISH2_042.97101−1.07103	288.43505	+8.42942	4.9	38.11	152.55	146.72	New
PN_UWISH2_043.10420−1.70207	289.06236	+8.25419	9.8	68.68	172.42	174.90	New
PN_UWISH2_043.25830+1.50423	286.25472	+9.87206	5.5	40.78	191.80	134.57	New
PN_UWISH2_043.65562−0.82777	288.53841	+9.14866	4.0	39.85	194.97	196.86	New
PN_UWISH2_044.18877+1.56732	286.63144	+10.72749	100.4	1127.24	16445.03	2750.69	PN G044.1+01.5
PN_UWISH2_044.34714+0.08637	288.04202	+10.18518	6.1	73.84	187.67	177.95	New
PN_UWISH2_044.73433+0.26046	288.06742	+10.60898	16.1	325.33	3884.71	3071.11	PN G044.7+00.2
PN_UWISH2_044.93245−0.01060	288.40523	+10.65887	27.7	859.52	5722.84	4532.10	PN G044.9+00.0
PN_UWISH2_045.44425−1.57085	290.05177	+10.38386	11.0	50.65	83.50	84.33	New
PN_UWISH2_045.45878−0.49801	289.09365	+10.89817	31.3	186.85	443.03	433.85	New
PN_UWISH2_045.95707+0.69049	288.25641	+11.89176	21.8	192.00	504.54	445.28	New
PN_UWISH2_046.09523+1.36603	287.70922	+12.32673	5.8	53.80	157.90	140.96	New
PN_UWISH2_046.63335+1.31220	288.01280	+12.77895	6.8	90.48	323.00	294.06	New
PN_UWISH2_046.93735−0.54973	289.84548	+12.18115	5.4	43.42	204.57	180.63	New
PN_UWISH2_047.18522+0.44999	289.05872	+12.86745	14.3	367.10	1724.42	1558.36	New
PN_UWISH2_047.44521+0.61199	289.03591	+13.17296	5.8	70.25	212.27	191.78	New
PN_UWISH2_047.50612−0.36750	289.95370	+12.76896	15.1	188.00	982.46	827.20	New
PN_UWISH2_047.52536+0.32144	289.33823	+13.10836	7.5	68.59	245.39	244.87	New
PN_UWISH2_047.61228+1.08168	288.68845	+13.53933	11.4	212.69	926.61	903.93	PN G047.6+01.0
PN_UWISH2_048.03497+0.12296	289.76335	+13.46599	7.1	73.77	205.19	185.16	New
PN_UWISH2_048.24968−0.46947	290.40474	+13.37742	12.3	152.83	747.66	539.49	New
PN_UWISH2_048.71570−0.28960	290.46721	+13.87323	25.4	364.39	2620.46	2407.63	PN G048.7−00.2
PN_UWISH2_048.99884+0.77703	289.63259	+14.62389	16.9	240.14	1116.38	1035.00	New
PN_UWISH2_049.28561+0.00740	290.47382	+14.51586	46.3	569.06	2981.11	2487.01	PN G049.2+00.0
PN_UWISH2_049.86763+1.06075	289.79393	+15.52434	18.8	88.86	197.54	208.44	New
PN_UWISH2_049.91632−1.08675	291.77791	+14.55322	7.5	93.90	684.22	413.16	New
PN_UWISH2_050.04556−0.79804	291.57894	+14.80423	11.8	168.42	916.59	828.63	New
PN_UWISH2_050.48027+0.70434	290.41955	+15.89793	10.0	53.94	406.30	265.92	PN G050.4+00.7
PN_UWISH2_050.55559+0.04506	291.06046	+15.65315	13.4	151.83	1031.51	822.92	MSX6C G050.5557+00.0448
PN_UWISH2_050.66579+1.33631	289.92941	+16.35846	4.6	25.36	158.23	146.07	NVSS J191942+162128
PN_UWISH2_050.66912+0.00673	291.15137	+15.73500	14.9	296.54	1740.80	1598.35	PN G050.6+00.00
PN_UWISH2_050.71285−0.17840	291.34224	+15.68573	4.1	22.96	57.61	54.64	SSTGLMC G050.7128−00.1780
PN_UWISH2_050.78036+1.18512	290.12457	+16.38873	13.0	76.08	163.43	159.22	New
PN_UWISH2_050.90936+1.05076	290.31138	+16.43949	4.2	28.91	113.63	79.79	New
PN_UWISH2_050.92866+0.43874	290.88325	+16.16805	8.8	97.01	326.21	328.86	New

Table C.1 – continued from previous page

Source ID	RA	DEC	Radius	Area	F$_{tot}$	F$_{med}$	Other ID
	[deg]	[deg]	[arcsec]	[arcsec^2]	[10^{-19}Wm^{-2}]	
PN_UWISH2_051.36290+0.87878	290.69251	+16.75857	4.8	53.32	350.03	319.39	New
PN_UWISH2_051.50791+0.17037	291.41553	+16.55106	11.4	126.26	578.84	398.98	PN G051.5+00.2
PN_UWISH2_051.76939+1.36491	290.44421	+17.34605	7.9	47.35	88.78	91.94	PN G051.7+01.3
PN_UWISH2_051.83306+0.28374	291.47259	+16.89104	2.6	8.95	116.17	80.64	PN G051.8+00.2
PN_UWISH2_052.32654−0.13737	292.10564	+17.12427	7.3	71.74	208.44	211.63	New
PN_UWISH2_052.46943−0.90047	292.87751	+16.88365	6.1	50.84	188.75	175.91	New
PN_UWISH2_052.70187−1.04355	293.12567	+17.01832	15.2	39.27	57.60	55.43	New
PN_UWISH2_053.04316−0.06957	292.40274	+17.78595	8.7	96.71	561.10	420.69	New
PN_UWISH2_053.36023−0.54988	293.00521	+17.83310	7.5	57.09	185.39	169.56	New
PN_UWISH2_054.29190−0.23778	293.19088	+18.79969	13.7	140.74	452.81	408.15	New
PN_UWISH2_054.71154+0.41990	292.79511	+19.48442	13.3	188.23	750.03	725.44	PN G054.7+00.4
PN_UWISH2_055.50747−0.55729	294.11183	+19.70728	11.7	63.20	136.06	139.41	PN G055.5−00.5
PN_UWISH2_055.85017+1.44210	292.42181	+20.97381	3.5	14.40	91.78	33.55	IRAS 19275+2052
PN_UWISH2_056.16673−0.41918	294.32630	+20.34998	25.6	152.88	544.46	501.19	PN G056.1−00.4
PN_UWISH2_056.34479−1.53764	295.45680	+19.95462	22.9	244.36	688.72	737.19	New
PN_UWISH2_056.42331−0.37341	294.41770	+20.59614	15.7	36.70	140.07	135.03	PN G056.4−00.3
PN_UWISH2_056.48535−0.09364	294.18926	+20.78706	7.4	56.97	490.79	251.81	New
PN_UWISH2_056.52321+0.30702	293.83452	+21.01540	7.6	25.68	60.67	59.06	New
PN_UWISH2_056.61303−0.04761	294.21301	+20.92095	10.8	75.07	143.00	144.35	New
PN_UWISH2_057.32913+0.61698	293.96505	+21.87025	3.5	12.70	35.54	35.18	New
PN_UWISH2_057.59474+0.50715	294.20811	+22.04854	71.8	168.49	474.72	380.17	New
PN_UWISH2_057.64365+0.47814	294.26120	+22.07705	15.7	49.74	106.16	108.30	New
PN_UWISH2_057.72078+0.12541	294.63369	+21.97154	3.2	10.74	21.34	23.41	New
PN_UWISH2_057.81415+0.78641	294.06045	+22.37632	11.2	16.38	34.10	33.73	New
PN_UWISH2_057.83552+1.04920	293.82333	+22.52291	15.7	161.92	612.56	595.87	PN G057.8+01.0
PN_UWISH2_057.98004−0.76740	295.60822	+21.75634	16.7	434.52	4950.65	3888.95	PN G057.9−00.7
PN_UWISH2_058.03770−0.04866	294.96541	+22.16189	12.4	118.13	711.13	409.12	New
PN_UWISH2_058.17873−0.81177	295.75604	+21.90672	17.2	160.93	769.03	707.50	IPHASX J194301.3+215424
PN_UWISH2_058.80916+0.38692	294.96654	+23.04782	19.2	225.19	613.84	632.41	New
PN_UWISH2_059.18828−1.42144	296.87169	+22.47539	16.1	183.33	669.01	647.15	PN G059.1−01.4
PN_UWISH2_059.36328+1.00137	294.68039	+23.83244	3.0	7.63	22.54	23.88	New
PN_UWISH2_059.77812−0.82788	296.63714	+23.28371	9.7	177.59	4307.78	1662.24	PN G059.7−00.8
PN_UWISH2_059.87554−0.60874	296.48399	+23.47800	25.3	172.51	557.42	557.70	PN G059.8−00.6
PN_UWISH2_060.24810+0.82261	295.32874	+24.51420	32.1	185.63	879.93	762.55	Kronberger GN J1941.3+2430
PN_UWISH2_060.31487+0.79769	295.38886	+24.55989	2.6	11.74	49.98	47.90	New

Table C.1 – continued from previous page

Source ID	RA	DEC	Radius	Area	F_{tot}	F_{med}	Other ID
	[deg]	[deg]	[arcsec]	[arcsec^2]	$[10^{-19}\text{Wm}^{-2}]$		
PN_UWISH2_060.40130+0.97372	295.26758	+24.72207	9.5	91.77	219.05	219.33	New
PN_UWISH2_060.52372−0.31828	296.56513	+24.18437	7.3	103.74	1170.77	1066.45	PN G060.5−00.3
PN_UWISH2_060.79926+1.17327	295.29316	+25.16660	4.2	13.28	25.83	26.96	New
PN_UWISH2_061.84215+0.88506	296.14467	+25.92826	10.2	191.11	887.07	705.20	New
PN_UWISH2_061.91270+0.20109	296.84101	+25.64602	7.5	108.16	330.31	305.01	New
PN_UWISH2_062.07780−0.43633	297.54294	+25.46559	17.1	81.06	149.06	150.19	New
PN_UWISH2_062.13719+0.14857	297.01712	+25.81331	7.0	119.67	606.13	503.81	New
PN_UWISH2_062.15368+1.15140	296.06083	+26.33111	7.1	66.06	136.15	138.73	New
PN_UWISH2_062.29042+1.13629	296.15164	+26.44203	9.4	156.43	989.99	905.73	New
PN_UWISH2_062.45283−0.01779	297.35430	+26.00125	13.0	171.08	555.39	535.48	New
PN_UWISH2_062.49346−0.27008	297.61889	+25.90799	45.4	489.22	1341.03	1237.50	PN G062.4−00.2
PN_UWISH2_062.70165+0.06019	297.42017	+26.25520	12.6	248.72	2127.60	1395.32	PN G062.7+00.0
PN_UWISH2_062.75413−0.72565	298.20231	+25.89915	41.1	309.48	1031.28	963.32	PN G062.7−00.7
PN_UWISH2_062.97476+1.38380	296.29463	+27.15831	9.1	147.33	1006.81	864.83	PN G062.9+01.3
PN_UWISH2_063.92454−1.21740	299.34644	+26.64663	20.3	71.19	123.18	107.66	TEUTSCH PN J1957.3+2639
PN_UWISH2_064.13697−0.97667	299.24006	+26.95330	15.2	279.17	938.35	874.99	IPHASX J195657.6+265713
PN_UWISH2_064.18792+0.77438	297.57807	+27.89812	6.9	93.23	886.65	602.27	New
PN_UWISH2_064.29941−0.14559	298.53508	+27.52268	21.9	282.35	840.34	812.91	New
PN_UWISH2_064.94759+0.76048	298.03161	+28.54425	8.1	79.97	334.74	259.10	New
PN_UWISH2_065.54459+0.81855	298.32416	+29.08648	9.8	110.56	333.96	331.68	New
PN_UWISH2_075.90338+0.29517	305.56985	+37.51621	6.2	37.98	147.45	138.63	IRAS 20204+3721
PN_UWISH2_076.37264+1.17216	304.99291	+38.40071	28.0	937.52	4816.41	4462.80	PN G076.3+01.1
PN_UWISH2_076.88532+2.22199	304.24755	+39.41480	5.5	49.81	276.23	248.05	New
PN_UWISH2_077.65952−0.98321	308.18149	+38.19935	10.9	17.40	20.89	20.49	New
PN_UWISH2_077.68068+3.12797	303.84237	+40.57914	18.1	89.89	489.55	414.05	PN G077.7+03.1
PN_UWISH2_077.77375+1.55436	305.61335	+39.77046	4.6	39.10	184.09	152.10	New
PN_UWISH2_077.84010+0.86042	306.39998	+39.42610	17.1	177.79	449.55	427.28	New
PN_UWISH2_078.92993+0.76378	307.32851	+40.25589	9.1	195.70	3896.91	3160.55	PN G078.9+00.7
PN_UWISH2_079.33319+2.14863	306.14806	+41.38834	6.9	57.66	158.81	161.45	New
PN_UWISH2_079.62439+0.40225	308.25045	+40.60291	15.5	78.42	172.78	179.45	New
PN_UWISH2_079.77014+1.89347	306.76299	+41.59724	4.6	42.87	82.23	83.60	New
PN_UWISH2_080.26214+0.24219	308.92358	+41.01858	7.3	52.52	132.40	129.20	New
PN_UWISH2_081.70275+2.15524	308.01013	+43.31551	6.9	28.75	56.09	54.25	New
PN_UWISH2_082.02890−0.30589	310.94401	+42.08439	6.4	70.10	134.10	134.23	New
PN_UWISH2_084.20031+1.09069	311.29225	+44.65363	41.3	1754.40	13412.66	12703.83	PN G084.2+01.0

Table C.1 – continued from previous page

Source ID	RA	DEC	Radius	Area	F_{tot}	F_{med}	Other ID
	[deg]	[deg]	[arcsec]	[arcsec^2]	$[10^{-19}Wm^{-2}]$		
PN_UWISH2_084.68426−0.72166	313.67853	+43.87961	8.3	22.25	35.79	37.44	New
PN_UWISH2_143.50140−2.81706	49.59757	+54.07942	61.1	399.82	1135.87	1091.73	New
PN_UWISH2_144.15931−0.50100	52.77255	+55.64775	16.6	657.79	2599.43	2473.29	BFS 30
PN_UWISH2_146.29327+0.54871	56.89683	+55.22098	5.7	48.63	97.88	95.31	IRAS 03437+5503
PN_UWISH2_149.16730−0.22038	59.84500	+52.80158	2.2	5.48	4.97	6.74	New
PN_UWISH2_149.43257−2.19327	58.12051	+51.11816	10.5	258.08	1097.52	1094.26	New
PN_UWISH2_151.30910−0.74888	61.88161	+50.98841	4.9	67.14	376.14	206.52	New
PN_UWISH2_153.77044−1.40652	63.97733	+48.82783	4.7	49.03	224.19	201.51	PN G153.7−01.4
PN_UWISH2_357.65660+0.26265	264.72283	−30.78903	10.0	82.48	568.19	478.38	New
PN_UWISH2_358.23394−1.18468	266.51148	−31.06071	19.4	489.97	6329.42	5781.65	SSTGLMC G358.2595−01.9129
PN_UWISH2_358.25962−1.91267	267.25577	−31.41518	7.9	73.67	1606.15	506.11	New
PN_UWISH2_359.35683−0.98000	266.98384	−29.99451	28.1	567.26	21509.73	8645.04	PN G359.3−00.9

# Appendix D

Relative UWISH2 Coverages of Cygnus and Auriga
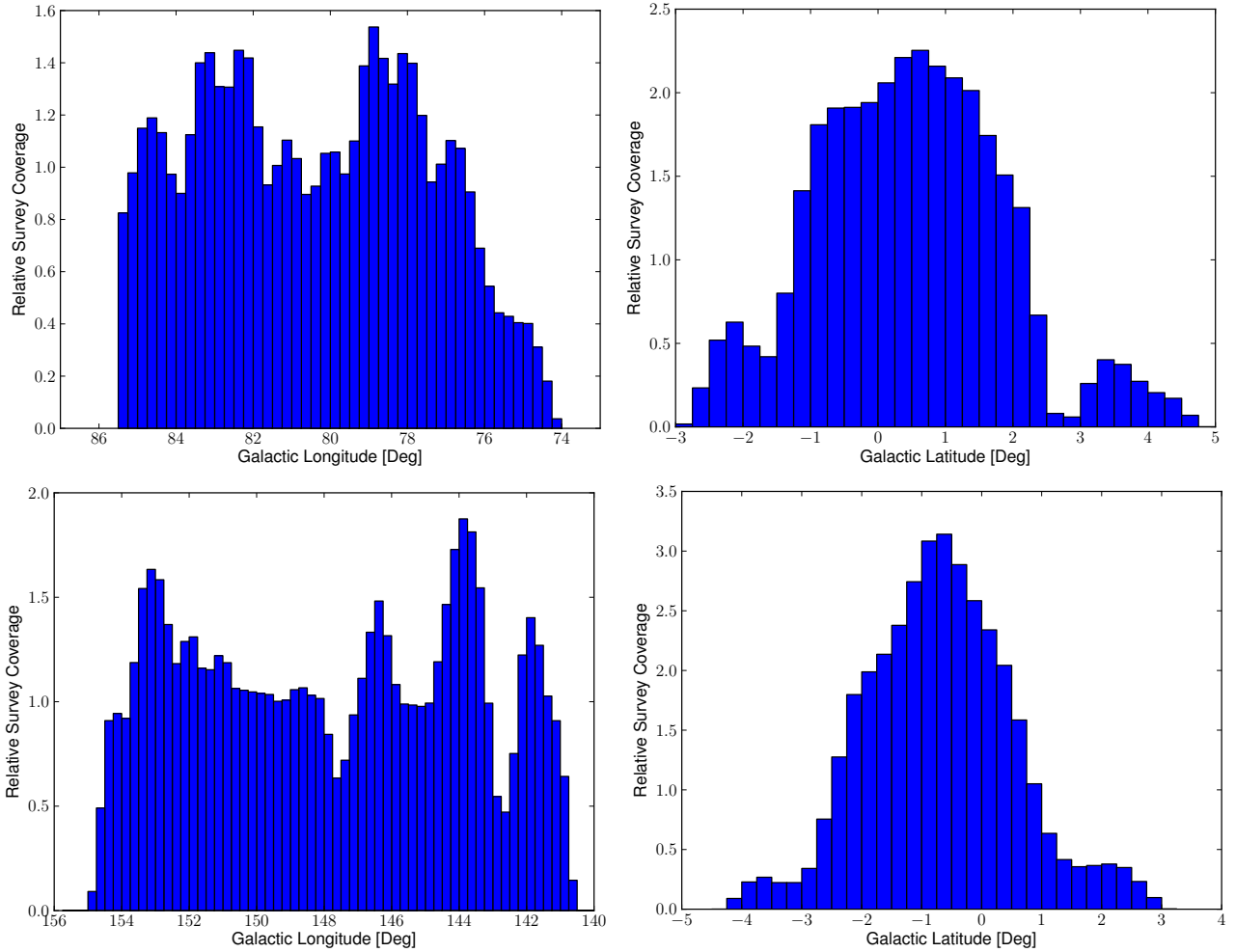
Figure D.1: Left: Galactic longitude. **Right:** Galactic Latitude. Histograms showing the relative coverages at certain Galactic longitudes and latitudes of Cygnus (top) and Auriga (bottom). We can see that compared to the GP in Figure 2.3, the coverage is not nearly as homogeneous. This is due to specifically targeting regions of high column density.
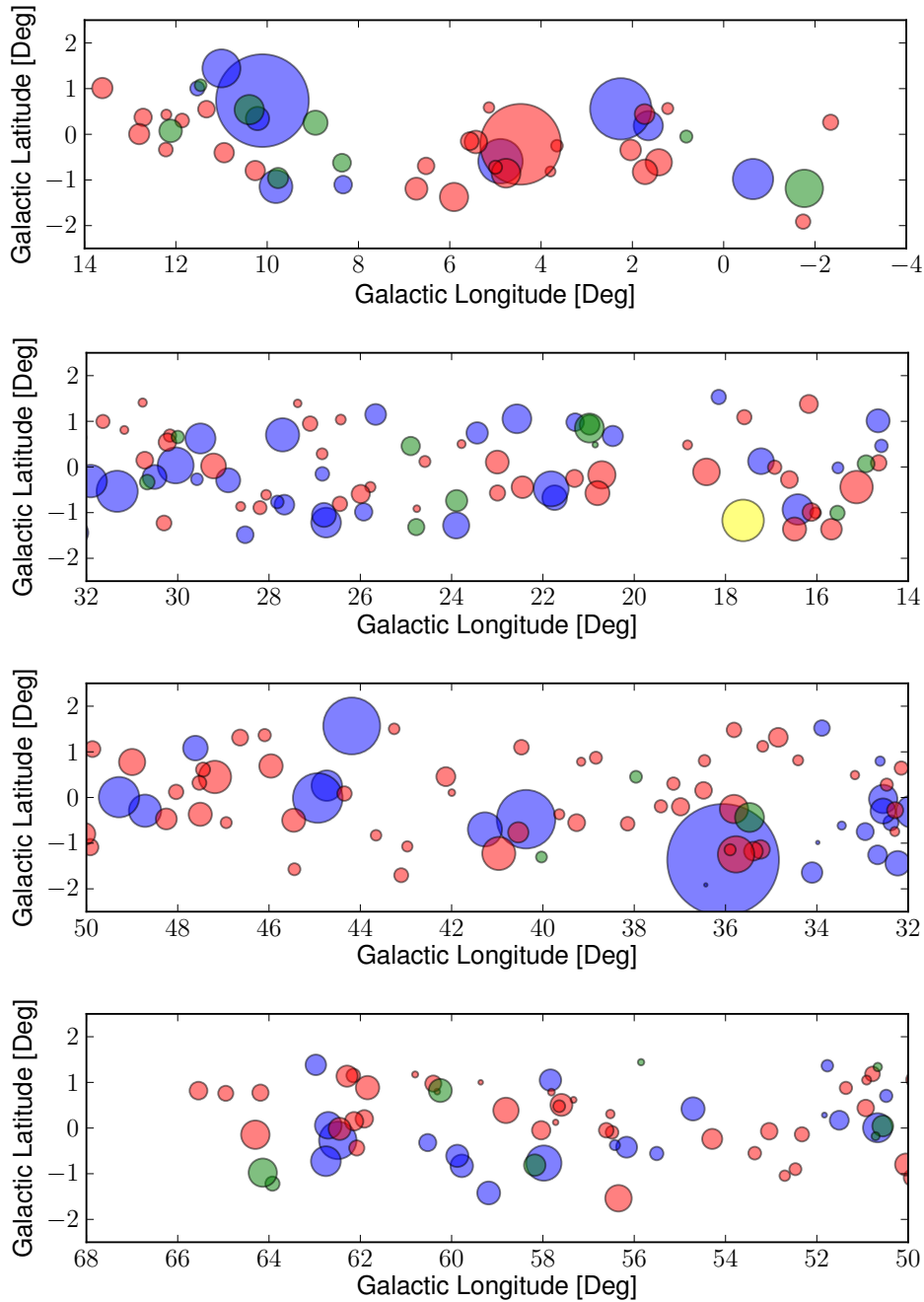
Appendix E

# Distribution of Planetary Nebulae in the GP
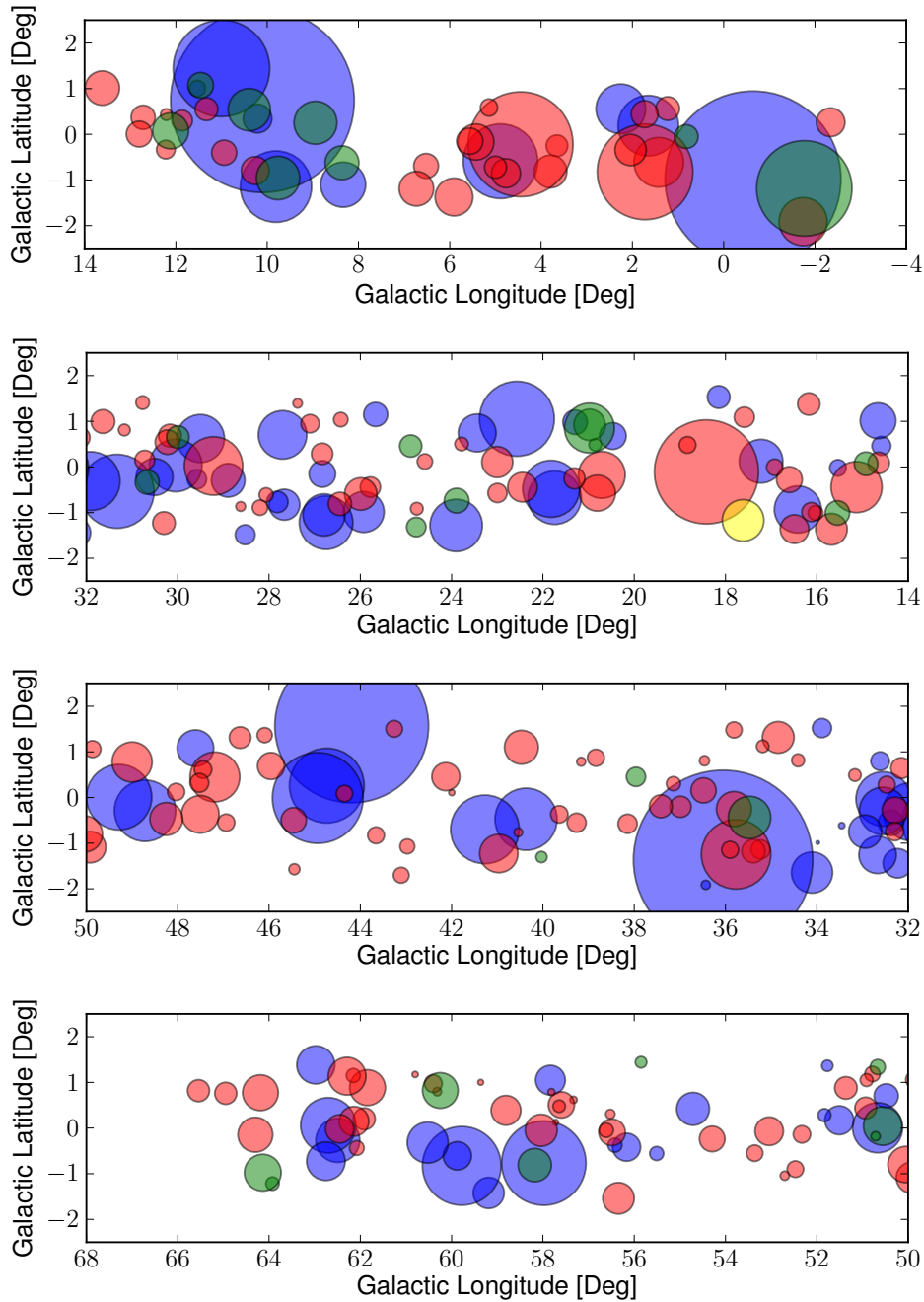
Figure E.1: The location in Galactic co-ordinates of the PNe within the four defined sections of the GP. The top plot represents section one, with sections two, three and four following in descending order. The 'New' candidate PNe are represented by red circles, the reclassified PNe are represented by green circles and the previously known PNe are represented by blue circles. The circle radius has been scaled to the total flux of the PNe. The yellow circle in the second panel (section two) represents the known PN G017.6-01.1, which would be several times bigger than the panel under the same scaling as the other PNe. Previously known PNe typically possess higher flux than the candidate PNe, indicating that the emission from 'New' PNe is likely from young PNe embedded in dust.

156

Figure E.2: The location in Galactic co-ordinates of the PNe within the four defined sections of the GP. The top plot represents section one, with sections two, three and four following in descending order. The 'New' candidate PNe are represented by red circles, the reclassified PNe are represented by green circles and the previously known PNe are represented by blue circles. The circle radius has been scaled to the area of the PNe emission. The yellow circle in the second panel (section two) represents the known PN G017.6-01.1, which would be several times bigger than the panel under the same scaling as the other PNe. Previously known PNe typically possess higher area than the candidate PNe, indicating that the emission from 'New' PNe is likely from young PNe embedded in dust.
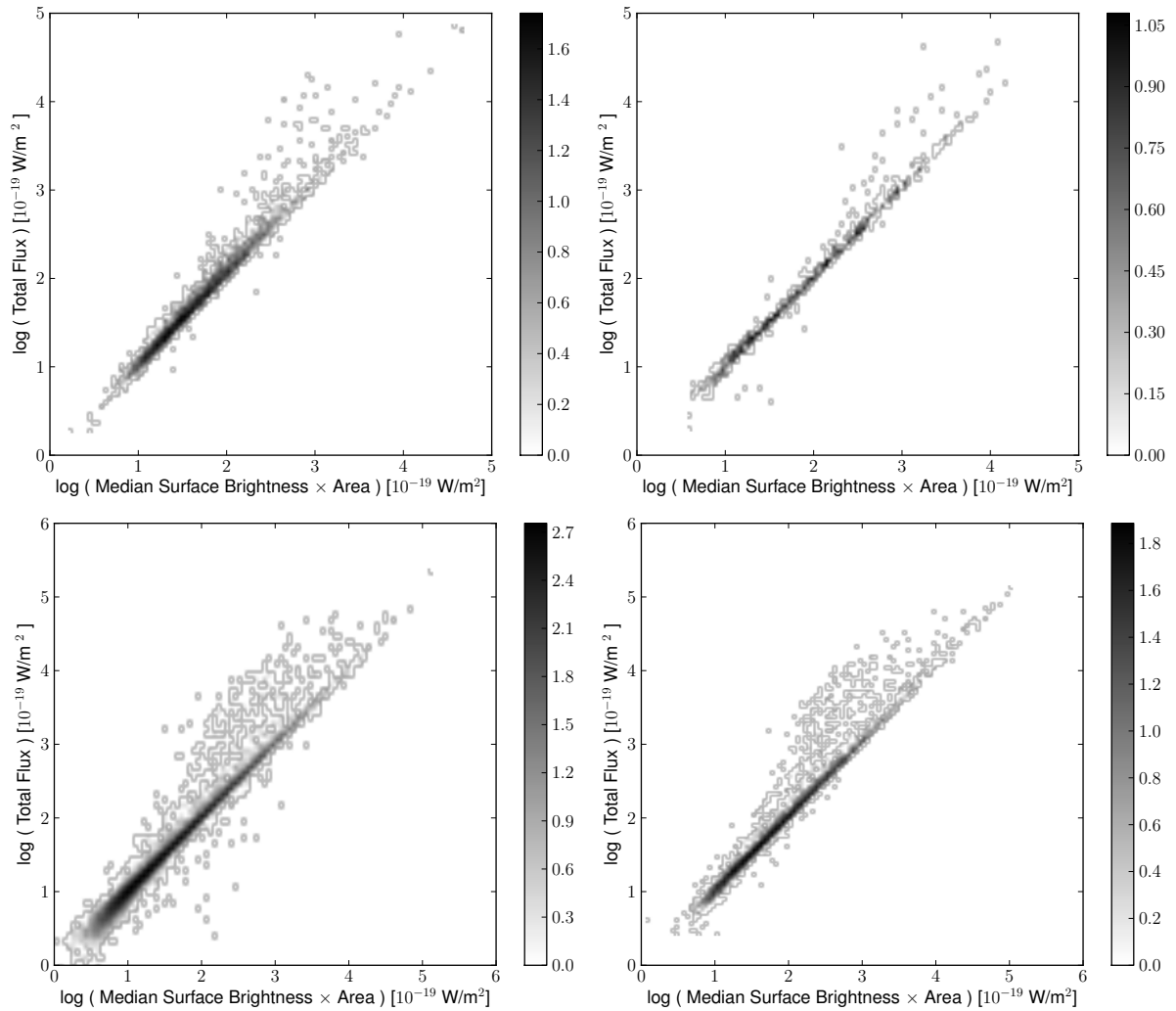
157

Appendix F

GP Coverages for Non-Jet Features
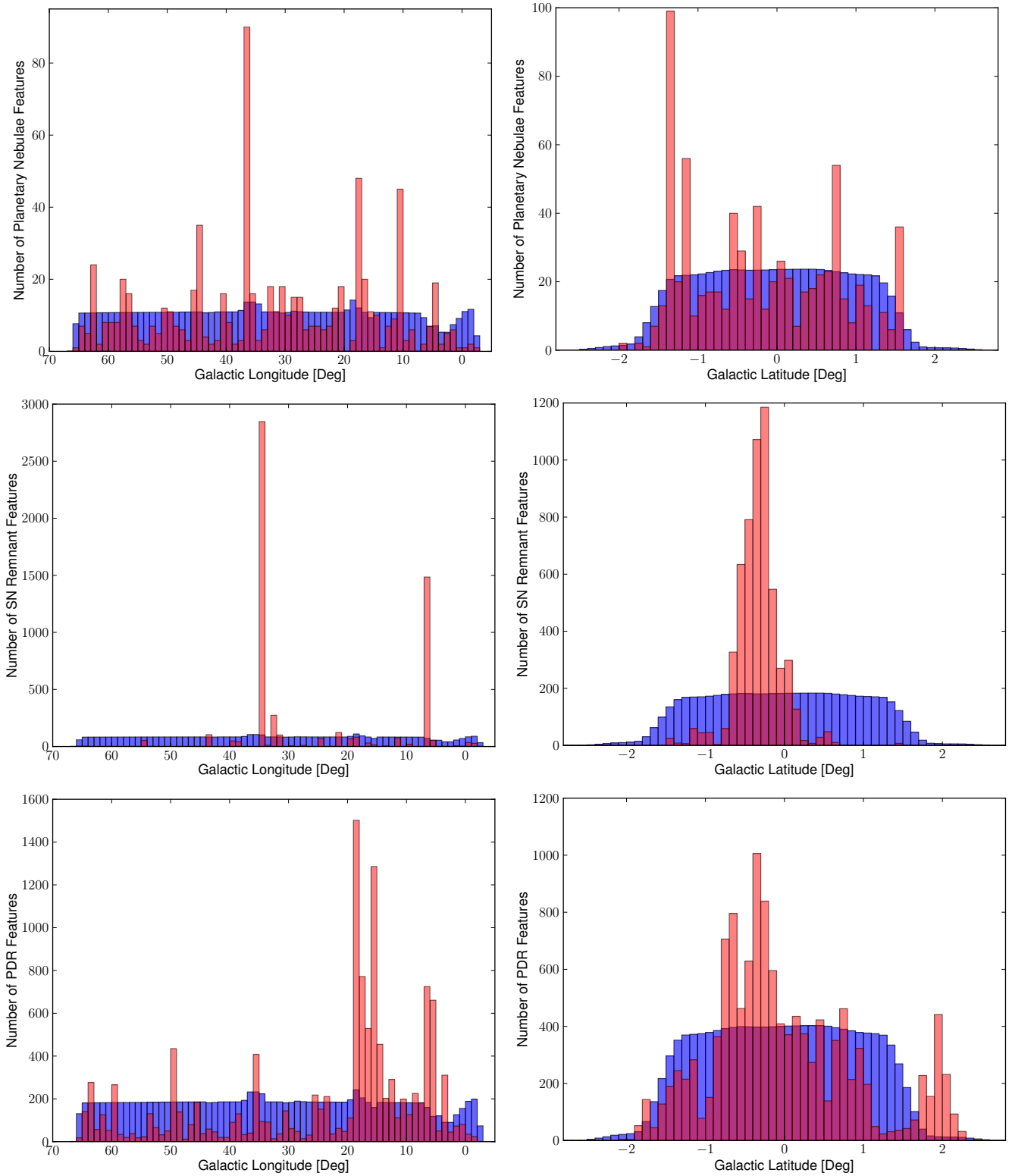
Figure F.1: The distribution of PNe (top), SNR (middle) and PDR (bottom) features in the GP found per one degree Galactic longitude (top) and 0.1 degrees Galactic latitude (bottom) versus the projected distribution using the relative survey coverage at each region (blue).

159

Appendix G

Total Flux Versus MSB Flux Density Maps

Figure G.1: Density mapping for the total flux versus the MSB flux values of a single H_2 emission feature whose ratio of the two values (before Log) lies between 1:2 and 2:1. From top left to bottom right: jet/outflow features, PNe features, PDR features and SNR features . The grayscale indicates the Log of the density of objects in each position. A minute fraction of H_2 features are not in the figures due to a negative total flux or negative Log value of either flux.